Computational Modeling of Electroactive Hydrogels for Cartilage–Tissue Repair Using Electrical Stimulation

Dissertation
zur
Erlangung des akademischen Grades
Doktor-Ingenieur (Dr.-Ing.)
der Fakultät für Informatik und Elektrotechnik
der Universität Rostock

vorgelegt von

Abdul Razzaq Farooqi, geboren am 02.04.1988 in Bahawalpur, Pakistan

Tag der Einreichung: 17.06.2020
Tag der Verteidigung: 16.11.2020

Gutachter:
Prof. Dr. Ursula van Rienen, Universität Rostock
Prof. Dr. Rainer Bader, Universitätsmedizin Rostock
Prof. Dr. Ludger Klinkenbusch, Christian-Albrechts-Universität zu Kiel

https://doi.org/10.18453/rosdok_id00002869

Dieses Werk ist lizenziert unter einer
Creative Commons Namensnennung 4.0 International Lizenz.

Abstract

The self-repair capability of articular cartilage is limited due to the lack of vascularization and low turnover of its extracellular matrix. Regenerating hyaline cartilage remains a significant clinical challenge as most of the non-surgical and surgical treatments provide only mid-term relief. Eventually, further pain and mobility loss occur for many patients in the long run due to further joint deterioration. In quest of therapeutic options, electrical stimulation has been proposed for improving tissue-engineering approaches for the repair of articular cartilage. The use of electrical stimulation for the repair of cartilage tissue requires detailed preliminary analysis, which is done in the present work. Computational models are used as they have the power to simulate various surgical conditions without damaging the specimen. Moreover, they serve for cross-validation with experimental models, elucidating important limitations of *in vitro* set-ups. In this thesis, computational models have been studied that can be used for optimizing the experimental protocols for cartilage–tissue repair using electrical stimulation.

The findings of this thesis can be summarized into four main achievements. First, a general mathematical framework based on continuum mechanics has been formulated for *in silico* modeling of cartilage tissue properties due to various biophysical stimuli. Moreover, based upon this framework, *in silico* investigations reported to date involving induced electrical properties of cartilage tissue discussing the effects of various biophysical stimuli have been summarized. Second, a numerical study involving electromechanical transduction in a bovine cartilage–tissue sample has been carried out using the open-source finite-element computational software FEniCS with Python interface. The simulation results have been compared to the experimental results from the literature. Third, a simulation model of electroactive hydrogels to be used for cartilage–tissue repair employing finite-element software FEniCS is presented. The proposed mathematical formulation was first validated with an example from the literature. Then, the effect of electric stimulation on a circular hydrogel sample was computed that served as a model for a cartilage-repair implant. Finally, the multiphysics transport model is used to study the electromechanical effect of electrical and osmotic stimulation on the cell-seeded hydrogel scaffolds using the finite element method. The proposed mathematical formulation is validated with data from literature and its application as the cartilage-repair implant is discussed. This thesis is a step forward in providing augmented computational models for cartilage–tissue repair using electrical stimulation.

Zusammenfassung

Die Fähigkeit des Gelenkknorpels, sich selbst zu regenerieren, ist aufgrund der fehlenden Vaskularisierung und des niedrigen Umsatzes seiner extrazellulären Matrix begrenzt. Die Regeneration von lädiertem hyalinem Knorpel stellt nach wie vor eine bedeutende klinische Herausforderung dar, da die meisten konventionellen Behandlungsmethoden nur eine mittelfristige Linderung bringen. Aufgrund eines weiteren Verschleißes im Gelenk treten bei vielen Patienten langfristig Schmerzen und Mobilitätseinbußen auf. Ein alternativer Therapieansatz zu klassischen operativen Eingriffen ist die elektrische Stimulation des Knorpelgewebes im Gelenk. Diese neuartige Methode bedarf ausführlicher Voranalyse, die in der vorliegenden Arbeit gemacht wird. Rechnergestützte Modelle bieten die Möglichkeit, experimentelle Arbeiten vorzubereiten und die Ergebnisse aus Experimenten tiefgehendzu analysen. So können verschiedene experimentelle Bedingungen simuliert werden, ohne die Knorpelprobe zu beschädigen. Des Weiteren dienen Modelle der Kreuzvalidierung mit experimentellen Modellen, wodurch wichtige Einschränkungen *in vitro* aufgeklärt werden. In dieser Arbeit wurden Computermodelle untersucht, die zur Optimierung der experimentellen Protokolle für die Knorpelgewebereparatur mittels elektrischer Stimulation verwendet werden können.

Die Ergebnisse dieser Arbeit lassen sich in vier Errungenschaften zusammenfassen. Erstens wurde ein allgemeiner mathematischer Rahmen auf der Grundlage der Kontinuumsmechanik für die *in silico*-Modellierung von Knorpelgewebeeigenschaften aufgrund verschiedener biophysikalischer Stimuli formuliert. Darüber hinaus wurden auf der Grundlage dieses Rahmens bisher berichtete *in silico*-Untersuchungen mit induzierten elektrischen Eigenschaften des Knorpelgewebes zusammengefasst, in denen die Auswirkungen verschiedener biophysikalischer Stimuli diskutiert wurden. Zweitens wurde eine numerische Studie zur elektromechanischen Transduktion in einer Knorpelgewebeprobe vom Rind durchgeführt, bei der die Open-Source-Finite-Elemente-Berechnungssoftware FEniCS mit Python-Schnittstelle verwendet wurde. Die Simulationsergebnisse wurden mit den experimentellen Ergebnissen aus der Literatur verglichen. Drittens wird ein Simulationsmodell von elektroaktiven Hydrogelen vorgestellt, das für die Knorpelgewebereparatur mit der Finite-Elemente-Software FEniCS verwendet wird. Die vorgeschlagene mathematische Formulierung wurde zunächst an einem Beispiel aus der Literatur validiert. Dann wurde die Wirkung der elektrischen Stimulation auf eine kreisförmige Hydrogelprobe berechnet, die als Modell für ein Knorpelreparatur-Implantat diente. Schließlich wird ein multiphysikalisches Transportmodell verwendet, um die elektromechanische Wirkung der elektrischen und osmotischen Stimulation auf zellbesiedelte Hydrogel-Scaffolds mit

Hilfe der Finite-Elemente-Methode zu untersuchen. Die vorgeschlagene mathematische Formulierung wird mit Daten aus der Literatur validiert. Weiterhin wird ihre Anwendung in Bezug auf das Knorpelreparaturimplantat diskutiert. Diese Arbeit stellt einen Fortschritt für die Bereitstellung detaillierter Rechenmodelle für die Knorpelgewebereparatur mittels elektrischer Stimulation dar.

Acknowledgement

It has been almost four years since I moved to Germany to pursue my PhD degree in Computational Science and Engineering. It was my first time studying abroad and it was a pleasant learning experience through exciting and sometimes challenging events.

First and foremost, my sincere thanks go to my supervisor Prof. Dr. Ursula van Rienen for helping me in every step of my PhD thesis and answering all my questions patiently. She was always there for suggestions, guidance, and support during this research. I am also highly indebted to Prof. Dr. Rainer Bader for his advice and help in understanding the medical aspects related to my thesis.

I would also like to thank all my current and former colleagues at the Institute of General Electrical Engineering, especially Julius, Konstantin, Yogesh, Duy, and Gowrishankar for their help and coordination extended to me during my PhD thesis. I always found my colleagues helpful not only in the academic activities but in daily life as well. A pleasant academic atmosphere was maintained because of my colleagues and my stay remained very calm and memorable.

I am thankful to the Higher Education Commission (HEC), Pakistan, for providing me with a PhD scholarship in collaboration with the German Academic Exchange Service (DAAD). I am thankful to the Islamia University of Bahawalpur, Pakistan, for granting me the study leave to pursue my PhD degree.

It was a nice experience to work as an associated member in the Collaborative Research Centre (CRC) 1270 Electrically Active Implants (ELAINE) funded by the Deutsche Forschungsgemeinschaft (DFG, German Research Foundation) – SFB-1270/1 – 299150580. This opportunity enabled me to broaden my knowledge and meet many good people to learn from them.

My sincere thanks to my friends and colleagues at the Islamia University of Bahawalpur, Pakistan, for motivating me to pursue PhD degree and were always there to support me. My thanks go to all my friends in Rostock, who made my stay happy

and comfortable. I am also thankful to my friends back in Pakistan who have always stood for me in difficult times.

I am grateful to my parents, who have always encouraged me in every step of life. My sincere thanks to my brother and sisters for their motivation and support.

Finally, I am grateful to my wife and children for their love and patience during the journey of the PhD degree. Without their understanding and support, this work would never have come into existence.

Contents

List of Figures xiii

List of Tables xvii

List of Symbols xix

1 Introductory Remarks 1

1.1 Motivation . . . 1
1.2 Thesis Outline . . . 2

2 Background and Basic Concepts 5

2.1 Articular Cartilage Structure . . . 5
2.2 Cartilage Pathologies . . . 7
2.3 Repair Techniques/Therapeutic Alternatives . . . 9
2.4 Tissue–Engineering Approaches for Cartilage Repair . . . 11
2.5 Hydrogels for Cartilage–Tissue Repair . . . 12
2.6 Electrical Stimulation for Tissue Engineering . . . 13
2.7 Computational Electromagnetics . . . 15
  2.7.1 Maxwell's Equations . . . 16
  2.7.2 The Finite Element Method . . . 17
2.8 Finite Element Computational Software Employed . . . 20

3 Electrical-Stimulation Studies of Articular Cartilage 23

3.1 Direct Coupling . . . 23
  3.1.1 *In Vivo* Studies . . . 23
  3.1.2 *In Vitro* Studies . . . 23
3.2 Indirect Coupling . . . 24
  3.2.1 *In Vivo* Studies . . . 24
  3.2.2 *In Vitro* Studies . . . 25
3.3 Concluding Remarks . . . 26

4 Continuum Mechanics: Framework for Modeling Cartilage Properties 29
4.1 Overview 29
4.2 Continuum Mechanics 29
  4.2.1 Triphasic Theory with Diffusion Potential 35
  4.2.2 Modified Triphasic Theory 36
4.3 Electrical Properties of Cartilage for *In Silico* Studies 38
  4.3.1 Electrical Stimulation 39
  4.3.2 Mechanical Stimulation 41
  4.3.3 Other Stimuli 42

5 One-dimensional Electrokinetic Transduction Model Based on Continuum Theory 47
5.1 Overview 47
5.2 Model Formulation 47
5.3 Galerkin Form of the Finite Element Formulation 50
5.4 Results and Discussion 50
5.5 Convergence Study 53

6 Electroactive Scaffolds for Cartilage–Tissue Repair 55
6.1 Overview 55
6.2 Introduction 55
6.3 Mathematical Model 57
  6.3.1 Poisson Equation 60
  6.3.2 Nernst–Planck Equation 60
6.4 Results and Discussion 63
  6.4.1 Chemical Stimulation 63
  6.4.2 Electrical Stimulation 64
  6.4.3 Convergence Study 67
  6.4.4 Limitations 70

7 Electromechanics of Electroactive Scaffolds for Cartilage–Tissue Repair 73
7.1 Overview 73
7.2 Introduction 73
7.3 Mathematical Model 75
  7.3.1 Poisson Equation 77
  7.3.2 Nernst-Planck Equation 77
  7.3.3 Osmotic Pressure and Momentum Equations 78

7.4 Results 80
7.4.1 Chemical Stimulation 81
7.4.2 Electrical Stimulation 82
7.4.3 Osmotic Stimulation and Displacement 83
7.5 Discussion 85
7.5.1 Convergence Analysis 87
7.5.2 Limitations 88

8 Conclusions and Perspectives **91**

Bibliography **95**

List of Figures

2.1 Detailed composition and structure of the articular cartilage. **(a)** Location of diarthrodial joints in the body (top to bottom): neck, shoulder, elbow, hip, wrist, knee, and ankle, **(b)** location of cartilage in the knee joint covering the femur and tibia, **(c)** zonal structure of the articular cartilage with varying shape and orientation of chondrocytes and collagen fibres, **(d)** extracellular matrix of the chondrocytes, **(e)** molecular structure of cartilage. The figure is taken with permission from [1]. 6

2.2 Types of defect for the knee articular cartilage. **(a)** Grade 0 (normal cartilage), **(b)** Grade I (Softening or swelling), **(c)** Grade II (partial-thickness defect), **(d)** Grade III (full-thickness defect), **(e)** Grade IV (osteochondral defect). The figure is taken with permission from [2]. . 8

2.3 Currently used treatment methods of articular cartilage. **(a)** Microfracture, **(b)** osteochondral autograft transfer, **(c)** osteochondral allograft transplantation, **(d)** matrix-induced autologous chondrocyte implantation, **(e)** implantation of the processed allograft cartilage e.g. DeNovo NT, ProChondrix and Cartiform. The figure is taken with permission from [3]. 10

2.4 Schematic representation of various approaches for delivering electrical stimulation. **(a)** Direct stimulation, **(b)** capacitive stimulation, **(c)** inductive stimulation, **(d)** combined stimulation, **(e)** agar salt bridge configuration. The figure is taken with permission from [4–6]. 14

4.1 Schematic illustration of composition and structure of articular cartilage lining the bone adapted from Servin-Vences *et al.* [1] (not drawn to scale). 30

4.2 Schematic representation showing various approaches to observe the electrical properties in cartilage tissue. **(a)** Electrical stimulation, **(b)** confined compression, **(c)** unconfined compression, **(d)** indentation, **(e)** permeation configuration, **(f)** electro-osmosis/diffusion (without V_i). ΔP is the change in pressure, $\Delta\delta$ is the change in thickness of the cartilage sample, ΔV_i and ΔV_o are the change in input and output voltages, respectively. 40

5.1 Schematic representation and discretization for electrokinetic transduction model. **(a)** Electrical-to-mechanical transduction, **(b)** mechanical-to-electrical transduction, **(c)** discretization to find current-generated stress, **(d)** discretization to find the streaming potential due to applied stress. ΔP is the change in pressure, $\Delta\delta$ is the change in thickness of the cartilage sample, V_i and V_o are the input and output voltages, respectively. 48
5.2 Mechanical-to-electrical transduction–amplitude of the dynamic stiffness versus frequency. 51
5.3 Mechanical-to-electrical transduction–amplitude of streaming potential versus frequency. 52
5.4 Electrical-to-mechanical transduction–amplitude of current-generated stress versus frequency. 52
5.5 Relative error in amplitude of streaming potential as a function of mesh elements taken at a representative value of $f = 0.3\,\mathrm{Hz}$ using the Equation (5.13). 54
5.6 Relative error in amplitude of current-generated stress as a function of mesh elements taken at a representative value of $f = 0.7\,\mathrm{Hz}$ using the Equation (5.13). 54

6.1 Various steps involved in tissue engineering of knee articular cartilage using electrical stimulation by replacing the defect site with a chondrocyte-seeded hydrogel (adapted with permission from [7]). . . . 56
6.2 Hydrogel sample immersed in NaCl bath solution under externally applied electric field. 57
6.3 Local mesh refinement used at the interface of the hydrogel sample and the NaCl bath solution. 57
6.4 Proposed open-source simulation workflow. 59
6.5 Cation concentration: **(a)** two-dimensional electrical stimulation, **(b)** comparison of chemical and electrical stimulation versus x-position at $y = 0.0075\,\mathrm{m}$. 64

6.6 Anion concentration: **(a)** two-dimensional electrical stimulation, **(b)** comparison of chemical and electrical stimulation versus x-position at $y = 0.0075\,\mathrm{m}$. 64
6.7 Electric potential: **(a)** two-dimensional electrical stimulation, **(b)** comparison of chemical and electrical stimulation versus x-position at $y = 0.0075\,\mathrm{m}$. 65
6.8 Cation-concentration profile at initial time $t = 0$ for a hydrogel scaffold immersed in solution. 66
6.9 Anion concentration profile at initial time $t = 0$ for a hydrogel scaffold immersed in solution. 67
6.10 Electric potential distribution at initial time $t = 0$ for a hydrogel scaffold immersed in solution. 68
6.11 Transient variation of quantities for a hydrogel scaffold immersed in solution along the x-direction at $y = 0.0075\,\mathrm{m}$: (**a**) cation concentration, (**b**) anion concentration, (**c**) electric potential. 69
6.12 Relative error according to Equation (6.21) as observed at the representative point: **(a)** cation concentration, **(b)** anion concentration, **(c)** electric potential. 71
6.13 Global convergence by evaluating L^2 error according to Equation (6.22): **(a)** cation concentration, **(b)** anion concentration, **(c)** electric potential. 72

7.1 Different steps for the cartilage–tissue repair employing electrical stimulation by transplanting chondrocyte-seeded hydrogel at the defect site (adapted with permission from [7]). 74
7.2 Sketch of a hydrogel in a electrolyte solution exposed to an external electric field. 75
7.3 Local mesh refinement used at the interface. 75
7.4 Simulation flow chart of the problem. 80
7.5 Comparison for the distribution of horizontal displacement of the hydrogel. 81
7.6 Cation concentration distribution: **(a)** under electrical stimulation, **(b)** under chemical or electrical stimulation, respectively, at $y = 0.0075\,\mathrm{m}$ versus the x-direction. 83
7.7 Anion concentration distribution: **(a)** under electrical stimulation, **(b)** under chemical or electrical stimulation, respectively, at $y = 0.0075\,\mathrm{m}$ versus the x-direction. 83

7.8 Electric potential distribution: **(a)** under electrical stimulation, **(b)** under chemical or electrical stimulation, respectively, at $y = 0.0075\,\mathrm{m}$ versus the x-direction. 84
7.9 Ionic concentration distributions to evaluate the osmotic pressure difference for the electro-chemo-mechanical coupling scheme under electrical stimulation. 86
7.10 Osmotic pressure in the hydrogel due to variation of ionic concentrations. 86
7.11 Comparison for the distribution of horizontal displacement of the hydrogel. 87
7.12 Relative error according to Equation (7.23): **(a)** cation concentration, **(b)** anion concentration, **(c)** electric potential. 89
7.13 Global convergence by evaluating L^2 error according to Equation (7.24): **(a)** cation concentration, **(b)** anion concentration, **(c)** electric potential. 90

List of Tables

3.1 Electrical stimulation studies of articular cartilage. 27

4.1 Electrical stimulation studies. 44
4.2 Mechanical stimulation studies. 45
4.3 Other stimulation studies. 46

5.1 Principal set of parameters. 53

6.1 Simulation parameters used in accordance with [8]. 65

7.1 Quantities used for simulations in accordance with [9]. 84

List of Symbols

Symbol	Description
$\mathbf{A}$	Arbitrary vector
$\mathbf{B}$	Magnetic flux density
b_{11}	Open-circuit hydraulic resistivity
b_{12}, b_{21}	Electrokinetic coefficients
b_{22}	Electrical resistivity
$\mathbf{b}$	Arbitrary vector
B_w	Coupling coefficient
c	Ionic content of the cartilage
c^k	Concentration of ion k
c^+	Cation concentration
c^-	Anion concentration
c^F	Fixed charge density
c_o^F	Initial fixed charge density
c_i^k	Previous time step
c_{i+1}^k	New time step
c_{gel}^+	Cation concentration in the hydrogel
c_{gel}^-	Anion concentration in the hydrogel
c_{sol}^+	Cation concentration in the solution
c_{sol}^-	Anion concentration in the solution
Cl^-	Chloride ion
Ca^{+2}	Calcium ion
dx	One-dimensional differential element of integration
dA	Two-dimensional differential element of integration
ds	Differential element of integration over the boundary $\partial\Omega$
$d\Omega$	Differential element of integration for the domain Ω
$\mathbf{d}$	Body force
$\mathbf{D}$	Electric flux density
$\mathbf{D}^k$	Diffusion tensor for ion k

Symbol	Description
D^k	Diffusion coefficient of ion k
D	Diameter of sample
$\mathbf{E}$	Electric field intensity
f	Frequency
$f_{\alpha\beta}$	Frictional coefficients per unit tissue volume between the inter-diffusing α and β components
f^k	Chemical-activity coefficient of ion k
F_c	Faraday constant
$\mathbf{H}$	Magnetic field intensity
H_A	Compressive modulus
$\mathbf{I}$	Identity matrix
j	Imaginary unit
$\mathbf{J}$	Electric current density
J	Magnitude of current density
$\mathbf{J}^k$	Ionic molar flux
$\mathbf{J}^w$	Water volume flux
$\mathbf{J}^k_{\text{diff}}$	Ionic diffusion flux
$\mathbf{J}^k_{\text{elect}}$	Ionic flux due to electric transference
$\mathbf{J}^k_{\text{conv}}$	Ionic flux due to convection
$k = +, -$	Ionic species
k_{11}	Short-circuit hydraulic permeability
k_{12}, k_{21}	Electrokinetic coefficients
k_{22}	Electrical conductivity
k_d	Open-circuit hydraulic (Darcy) permeability
$\mathbf{K}$	Hydraulic permeability tensor
m^α	Mass of component α
M^k	Molar weight of the kth ionic species
NaCl	Sodium chloride
Na^+	Sodium ion
p_{osm}	Osmotic pressure
p_{ini}	Initial osmotic pressure
P	Fluid pressure
q	Test function for the finite element method
r	Residual value

Symbol	Description
R	Gas constant
$\mathbf{S}$	Strain tensor
$\mathrm{tr}(\mathbf{S})$	Trace of the strain tensor
t	Time
T	Temperature
$\mathbf{u}^s$	Solid displacement
u_i	Current value of the degrees of freedom
u_{i-1}	Previous value of the degrees of freedom
p	Trial function for the finite element method
u	Displacement magnitude
$\mathbf{u}$	Displacement vector
$\mathbf{U}$	Relative fluid velocity
U_o	Constant of integration
v_k	Test function for the ionic concentration of ion k
v_u	Test function for the displacement
v_ψ	Test function for the electric potential
$\mathbf{v}^\alpha$	Velocity of component α
$\mathbf{v}^w$	Fluid velocity
$\mathbf{v}^k$	Ionic velocity
V	Total volume of the mixture
V^α	True volume of phase α
V_i	Input voltage
V_o	Output voltage
w_j	Weighting functions
x, y, z	Coordinates in the Cartesian coordinate system
z^k	Valence of ion k
z^f	Valence of fixed charge

Greek Symbols

Symbol	Description
$\alpha = s, w, k$	Solid, fluid, and ionic constituents of the mixture
σ	Total stress

Symbol	Description
κ	Conductivity of the medium
σ_I	Current-generated stress
ε	Permittivity of the medium
ε_r	Relative permittivity of the medium
ε_o	Permittivity of the vacuum
ε^w	Modified chemical potential of water
ε^k	Modified chemical potential of ion k
μ	Permeability of the medium
μ_r	Relative permeability of the medium
μ_o	Permeability of the vacuum
μ^α	Electrochemical potential of phase α
μ_o^α	Chemical potential of phase α at the reference configuration
ϑ^k	Ionic mobility of ion k
ρ	Electric charge density
ρ^α	Mass density of phase α
ρ^k	Density of ion k
ρ_T^α	True density of phase α
ρ_{mix}	Density of the mixture (tissue)
Ω	Problem domain
ϕ_i	Polynomial basis function
ϕ^α	Volume fraction of phase α
ϕ^w	Water volume fraction (porosity)
ϕ^s	Solid volume fraction (solidity)
ϕ^k	Volume fraction of ion k
ϕ_o^s	Volume fraction of solid phase at the reference configuration
ϕ_o^w	Volume fraction of water phase at the reference configuration
γ^k	Activity coefficient of ion k
φ^k	Osmotic coefficient of ion k
φ^w	Osmotic coefficient of water
ψ	Electric potential
ξ	Drag coefficient between the solid and water phase

Symbol	Description
ω	Angular frequency
Λ	Dynamic stiffness
Λ_s	Platen stiffness
λ_s, μ_s	Lamé constants
δ	Thickness of sample
δ_{ij}	Kronecker delta function
ν	Area-averaged fluid velocity through the hydrogel
Υ	Viscous damping between the electrolyte and polymer fibers
Ψ	Effective density of the gel
ζ	Source term
Δt	Time-step parameter
$\Delta\phi$	Donnan potential
$\nabla\times$	Curl operator
$\nabla\cdot$	Divergence operator
∇	Gradient operator
∇^2	Laplace operator
$\approx$	Approximately equal to
$:=$	Defined as

1 Introductory Remarks

1.1 Motivation

Articular hyaline cartilage is an inhomogeneous, hierarchically ordered, and multiphasic tissue that covers opposing bone surfaces in diarthrodial joints [10]. It is an avascular tissue comprised of chondrocytes surrounded by the extracellular matrix [11]. Chondrocytes are responsible for synthesizing and maintaining the extracellular matrix [12], which mainly consists of collagen fibers, proteoglycans, and the interstitial fluid phase [13]. Based on the distinct matrix composition and cellular properties, different zones of articular cartilage can be distinguished [1, 14]. The compositional and structural environment of the tissue is altered due to the progression of osteoarthritis or injury [15, 16]. Ideally, such alterations should be reversed for the proper functionality of the tissue.

Mechanical, electromagnetic, and electrical stimuli can promote growth, differentiation, and maturation of the cartilage tissue [17]. Articular cartilage exhibits electromechanical properties due to the electrically charged nature and depth-dependent properties of the tissue [18]. The mechanical deformation that occurs in cartilage tissue during weight-bearing produces internal electrical signals through streaming potentials, by the flow of charged particles across negatively charged proteoglycans of the tissue [17]. Conversely, applying an external electrical signal to the cartilage tissue can produce stress and deformation in the tissue [19, 20]. Upon removal of the external electrical or mechanical excitation, the deformed cartilage tissue recovers to its initial dimensions, due to the elasticity of the solid matrix, increased osmotic pressure, and fluid redistribution within the tissue [10, 21–23]. Thus, externally applied electrical signals that resemble the endogenous electrical fields have the promising potential to treat osteoarthritis patients in a less invasive manner.

Extensive studies have been carried out for the *in silico*, *in vitro*, and *in vivo* investigation of mechanical stimulation on articular cartilage [24–29]. However, few studies are available for electromagnetic and electrical stimulation. Specifically, the electromagnetic stimulation of cartilage has been investigated more in comparison to electrical stimulation. The limited research available for electrical and electromagnetic stimulation mainly considers the effect of these stimuli for *in vitro* animal and human samples and for *in vivo* animal models. So far, only a few simple *in silico* studies have been conducted for these two stimulation types. However, *in silico* investigation of these modes of stimuli for cartilage regeneration is required to obtain an optimal strategy for the tissue engineering of neocartilage [17].

Computational models of human musculoskeletal systems are a valuable tool for studying biomechanics in the healthy population, as well as the effects of injury and disease and their respective treatments. Designing of *in silico* strategies helps in understanding the complex biological processes and supports in enhancing the *in vitro* or *in vivo* behavior [30]. Another factor that may make incorporating computational models into experiments seem less daunting is that even solving a single simple equation can improve an experiment design [31], as repeating experiments is difficult due to ethical, logistical, and budgetary constraints.

Hydrogels have gained much attention for biomedical applications as they possess excellent biocompatibility and biodegradability [32]. They are versatile materials that can encapsulate the seeded cells mimicking the natural cartilage structure [33]. In addition, they can be designed into any form, shape, composition, and size and can reversibly swell or de-swell upon small biophysical changes of the environment [34]. Since articular cartilage is essentially a form of a natural polyelectrolyte hydrogel [35], electroactive hydrogel scaffolds are a promising approach to mimic its properties to improve cartilage–tissue engineering strategies [36]. The chondrogenic phenotype of chondrocytes inside these hydrogel matrices can be maintained by applying suitable biophysical stimuli [37].

1.2 Thesis Outline

This thesis is based on three journal publications, which have already been published. These three publications together with some additional information material have been reformulated for the thesis to maintain continuity and consistency. The articles are listed below.

- **A. R. Farooqi**, R. Bader, U. van Rienen, Numerical study on electromechanics in cartilage tissue with respect to its electrical properties, Tissue Eng. Part B Rev. 25 (2019) 152–166; `https://doi.org/10.1089/ten.teb.2018.0214`.

- **A. R. Farooqi**, J. Zimmermann, R. Bader, U. van Rienen, Numerical simulation of electroactive hydrogels for cartilage-tissue engineering, Materials (Basel). 12 (2019) 2913; `https://doi.org/10.3390/ma12182913`.

- **A. R. Farooqi**, J. Zimmermann, R. Bader, U. van Rienen, Computational study on electromechanics of electroactive hydrogels for cartilage-tissue repair, Comput. Methods Programs Biomed. 197 (2020) 105739; `https://doi.org/10.1016/j.cmpb.2020.105739`.

The thesis is organized as follows: Chapter 1 provides the introduction and motivation for choosing the topic. In Chapter 2, basic concepts related to the structure, injuries, and repair techniques of the cartilage tissue are presented. In addition, fundamentals of the computational electromagnetics and finite element method are introduced. In Chapter 3, the *in vitro* and *in vivo* state of the art that has been reported using either direct or indirect electrical stimulation for chondrocytes, cartilage tissue, or cell-seeded hydrogels is briefly discussed. In Chapter 4, the general framework of continuum mechanics is outlined, which is used for mathematical modeling of the induced electrical properties of cartilage tissue. Furthermore, a detailed literature survey for *in silico* electrical properties of cartilage induced due to different biophysical stimuli is presented. Chapter 5 describes the implementation of the linear electromechanical transduction in a cartilage sample using FEniCS. In Chapter 6, an open-source software framework is described for the finite-element simulation of electroactive scaffolds for cartilage-tissue repair. Moreover, solutions of a validated finite-element model and an extension of the model using circular geometry are reported. In Chapter 7, a finite-element simulation model on electromechanics of electroactive hydrogels seeded with chondrocytes is presented for cartilage–tissue repair using electric and osmotic stimulation. Moreover, the usage of the presented finite-element simulation model of electroactive scaffolds for designing cartilage–tissue repair experiments is discussed. The main conclusions drawn from this thesis are described in Chapter 8 together with some perspectives and recommendations for future work.

2 Background and Basic Concepts

This chapter introduces the structure, pathologies, and traditional as well as tissue–engineering approaches for the treatement of articular cartilage defects. Moreover, the significance of hydrogels and biophysical stimuli i.e., electrical stimulation for the cartilage–tissue repair is highlighted. Subsequently, the elementary equations of electromagnetic theory for studying the electrical stimulation response of hydrogels are described. Finally, the finite-element formulation for solving the partial differential equations is presented.

2.1 Articular Cartilage Structure

Depending upon composition and function, the three major types of cartilage in the human body are classified as elastic, fibrous, and hyaline [38]. These three types of cartilage perform multiple functions in the human body e.g., load bearing in intervertebral discs and articular joints, maintaining joint lubrication, forming the outer ears and nose, supporting the trachea, and forming long bones during growth and development [39].

Articular cartilage is a bradytrophic and avascular tissue that is synthesized and maintained by chondrocytes. Articular cartilage consists of two distinct phases: a fluid phase composed of water and electrolytes, and a solid phase, composed of chondrocytes, collagen fibrils, proteoglycans, and other glycoproteins [10]. Generally, 60–80% of total wet weight of the articular cartilage is fluid phase and the remaining 20–40% is the solid phase [40]. Furthermore, collagen fibrils, particularly type II, make up ∼50–75% and chondrocytes less than 5–10% of the solid phase [41], respectively, while proteoglycans and other glycoproteins compose most of the remaining solid phase [42]. Articular cartilage is divided into four zones: superficial, transitional, deep, and calcified zone. Each zone has varying matrix composition, morphology, and cellular and metabolic properties [29]. The detailed anatomy of the articular cartilage is depicted in Figure 2.1.

Mechanics of cartilage and chondrocytes is a function of complicated load sharing between musculoskeletal joints of the body, individual tissue structures within the joint, organization and properties of cells, and the microstructure within the

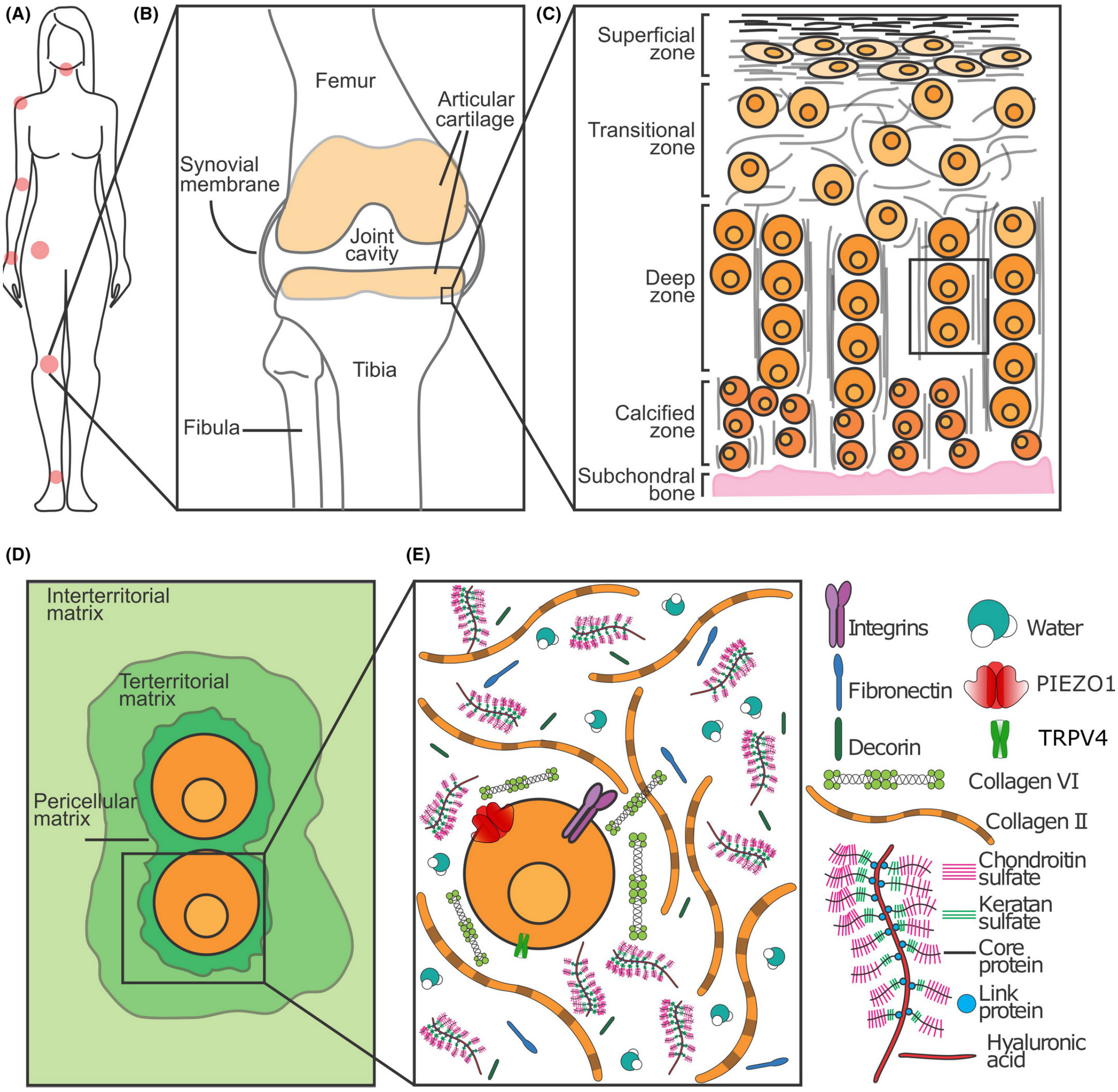
(A)
(B)
Femur
Articular cartilage
Synovial membrane
Joint cavity
Tibia
Fibula
(C)
Superficial zone
Transitional zone
Deep zone
Calcified zone
Subchondral bone
(D)
Interterritorial matrix
Terterritorial matrix
Pericellular matrix
(E)
Integrins
Water
Fibronectin
PIEZO1
Decorin
TRPV4
Collagen VI
Collagen II
Chondroitin sulfate
Keratan sulfate
Core protein
Link protein
Hyaluronic acid

Figure 2.1: Detailed composition and structure of the articular cartilage. **(a)** Location of diarthrodial joints in the body (top to bottom): neck, shoulder, elbow, hip, wrist, knee, and ankle, **(b)** location of cartilage in the knee joint covering the femur and tibia, **(c)** zonal structure of the articular cartilage with varying shape and orientation of chondrocytes and collagen fibres, **(d)** extracellular matrix of the chondrocytes, **(e)** molecular structure of cartilage. The figure is taken with permission from [1].

tissue [43, 44]. Damage of the cartilage tissue may lead to osteoarthritis resulting in pain and limitation of mobility for many patients. Treatment of cartilage defects poses a clinical challenge owing to the lack of intrinsic regenerative capacity of the cartilage. Current therapies available for cartilage repair provide mainly palliative treatment [11].

The native composition and structure of articular cartilage changes due to osteoarthritis or trauma [14]. Some successes have been made for the regeneration of articular cartilage, however, the complex signal transduction pathways and molecular mechanisms involved in progression of disease and regeneration of the tissue have not been fully understood, which makes it difficult to establish precise proliferation and differentiation methods for chondrogenesis [45, 46].

2.2 Cartilage Pathologies

Lesions of the articular cartilage tissue can be grouped into the lesions that affect only the cartilage (chondral lesions) or those that affect the entire thickness of the cartilage until they penetrate into the subchondral bone (osteochondral lesions) [47]. The Outerbridge classification system [48] is a prominent classification system used to grade the severity of cartilage lesions, with Grade 0 representing the normal cartilage. Softening or swelling of the cartilage is classified as Grade I defect. Clinically most frequently observed defect is Grade II [49] which contains fissures that do not extend to the subchondral bone (i.e., a chondral defect). Grade III defect is same as the Grade II defect but it extends to the full cartilage thickness.

Finally, if the subchondral bone underneath the articular cartilage is exposed as well, the tissue defect is classified as Grade IV. Although each defect type leads to similar symptoms for the patient, each defect type requires a different treatment method with associated issues and challenges. For the Grade I injury, the lesions alter and deteriorate the extracellular matrix of the tissue. For this type of defect, usually the remaining viable chondrocytes increase their synthetic activity and repair the affected areas. All other defect types always require some surgical intervention for the repair and regeneration of the cartilage tissue. The various cartilage lesions categorized according to the International Cartilage Regeneration & Joint Preservation Society (ICRS) grading system are shown in Figure 2.2.

Osteoarthritis is characterized by the change in structure and compositional shift of water, solid matrix, and electrolytes in the tissue [14, 50]. Particularly, the fibril-reinforced models of articular cartilage can be used to separate the collagen, proteoglycan, and water content in the tissue to study the cartilage degeneration at

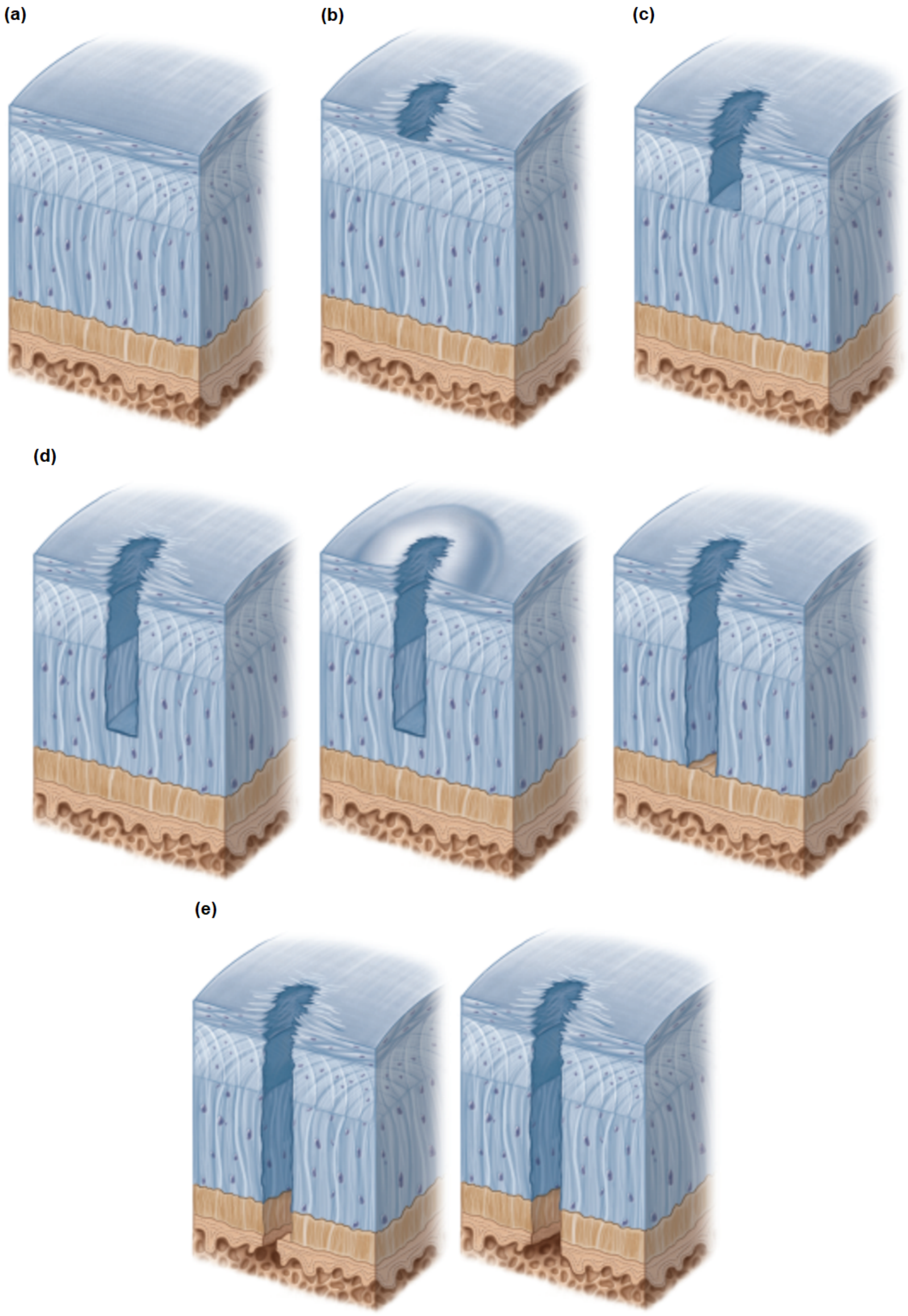

Figure 2.2: Types of defect for the knee articular cartilage. **(a)** Grade 0 (normal cartilage), **(b)** Grade I (Softening or swelling), **(c)** Grade II (partial-thickness defect), **(d)** Grade III (full-thickness defect), **(e)** Grade IV (osteochondral defect). The figure is taken with permission from [2].

the cell and tissue level [50–54]. These studies for the compositional change in the articular cartilage can further be extended using, for example, open-source software to include electrical stimulation for treatment of the cartilage tissue.

2.3 Repair Techniques/Therapeutic Alternatives

Treatment options for the damaged cartilage tissue depend on the level of progression and nature of the injury. Small cartilage defects can be managed non-invasively. For such defects, lifestyle changes, including weight loss and exercise, along with gait modification, are recommended to reduce progression of the disease [39]. Symptom relieving and non-surgical treatment options also include pain relief with paracetamol or non-steroidal anti-inflammatory drugs, and physical therapy to improve joint stability, muscle strength and neuromuscular control [55]. When nonsurgical treatments do not help the patient then surgical techniques are considered [56]. Rehabilitation and physical therapy are also important in aftercare of the surgical procedures.

The primary aim of the surgical treatments is to replace the defect site with a tissue that has the characteristics resembling to the native cartilage tissue. One of the treatment methods is bone marrow stimulation, which is creating microfractures through the articular cartilage until the subchondral bone is exposed [57] as indicated in Figure 2.3(a). These fractures allow the migration of mesenchymal cells to the affected site, and possibly their differentiation into chondrocytes to repair the lesion [58]. However, if the cells are not properly stimulated, the newly formed tissue is the fibrocartilage which degenerates with the passage of time due to its poor mechanical strength [59].

Another possible treatment method is the autologous tissue transfer procedure as illustrated in Figure 2.3(b), also known as mosaicoplasty [60]. In this method, small cylinders of healthy tissue are taken from the non-weight bearing edges of the articular cartilage, and then inserted into the same size holes drilled at the site of defect [61]. Similar treatment is the tissue grafting in which small fragments of healthy articular cartilage are taken from other joints of the body and inserted at the site of defected cartilage. Osteotomy is another surgical procedure in which a part of the bone-joint surface is removed to reduce load on the defected medial compartment and transferred to the intact lateral compartment [62, 63].

Osteochondral allograft transfer as indicated in Figure 2.3(c), is similar to the autograft transfer technique but here the replacement tissue used is from a cadaveric donor [64]. It is a promising technique for the repair of damaged tissue because it does not have the donor site limitation as in the osteochondral autograft transfer,

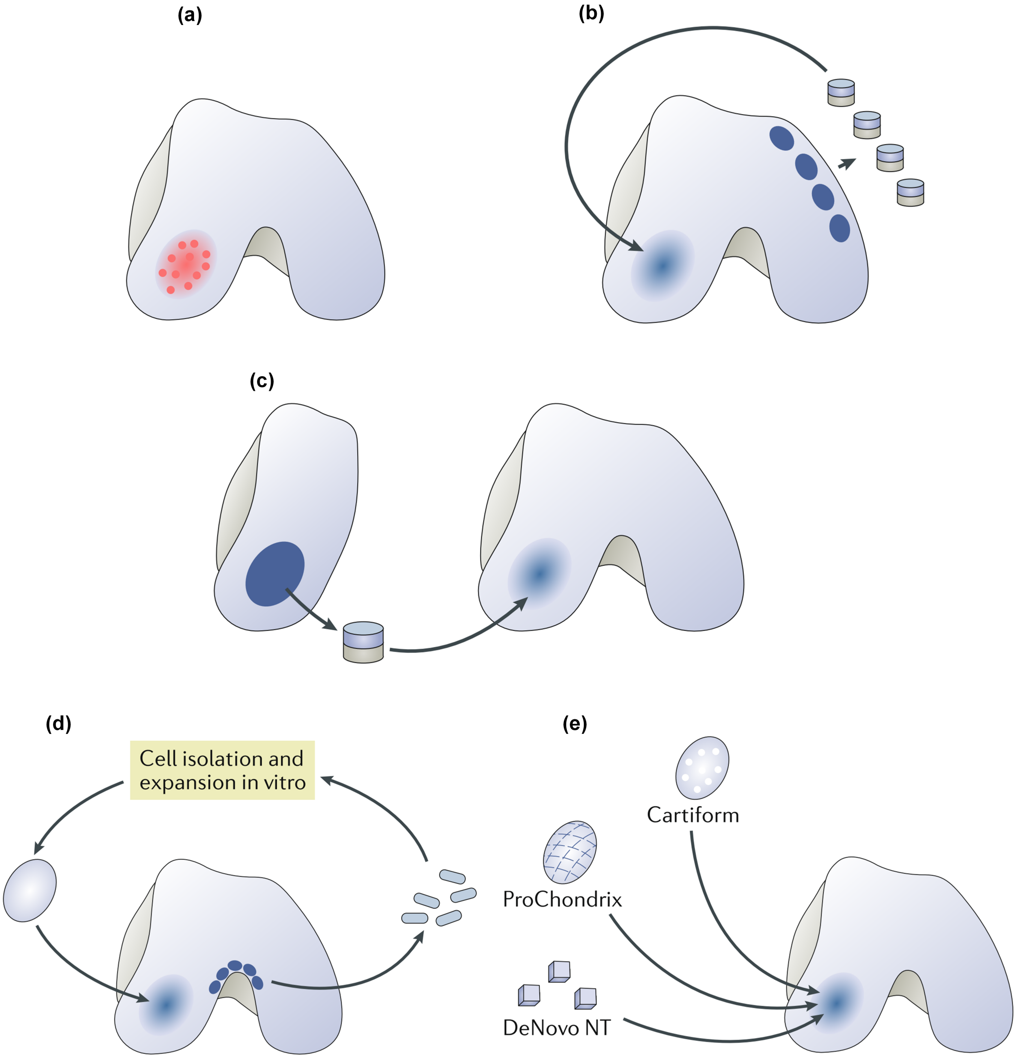
(a)
(b)
(c)
(d)
Cell isolation and expansion in vitro
(e)
Cartiform
ProChondrix
DeNovo NT

Figure 2.3: Currently used treatment methods of articular cartilage. **(a)** Microfracture, **(b)** osteochondral autograft transfer, **(c)** osteochondral allograft transplantation, **(d)** matrix-induced autologous chondrocyte implantation, **(e)** implantation of the processed allograft cartilage e.g. DeNovo NT, ProChondrix and Cartiform. The figure is taken with permission from [3].

but the availability of allograft tissue can limit its usage [65].

Autologous matrix-induced chondrogenesis is another innovative technique which combines the well-known microfracture method with commercially available porcine collagen scaffold [66]. First, mini-arthrotomy is performed which exposes and cleans the defect site. After this, microfracturing is done which releases blood and bone marrow containing mesenchymal stem cells. The acellular scaffold is then introduced into the defect site using fibrin glue. The scaffold matrix helps the mesenchymal stem cells to develop into chondrocytes, improve mechanical stability, control cell migration, and influence cartilage production [66–68]. Autologous matrix-induced chondrogenesis is a single-step surgical procedure and found to be safe and effective in several studies for treating full-thickness cartilage defects [69–71].

2.4 Tissue–Engineering Approaches for Cartilage Repair

The aim of tissue engineering is the development of bioartificial substitutes for the damaged tissues and organs by combining the engineering and life sciences tools [72]. Tissue engineering modalities can be classified as the *in vivo* and *ex vivo* [73]. In the first approach, the construct is implanted with or without prior partial *in vitro* cultivation and is allowed to mature *in vivo* for tissue repair and regeneration. For the second approach, the tissue is generated entirely *in vitro* with full functionality before transplantation. In both approaches, the three components that crucially influence the outcome of a tissue–engineered construct are the responsive cells, biomaterial scaffolds, and an appropriate biophysical stimuli or the growth factors [74]. Various combinations of these elements produce a variety of interesting approaches. Some of the recent clinically used tissue–engineering approaches are discussed below.

The goal of cartilage–tissue engineering is to meet the clinical need for repair of the damaged cartilage tissue by employing unique combinations of materials, cells, and signals for the formation of neocartilage tissue. One such technique is the autologous chondrocyte implantation which was first introduced in an animal model by Grande *et al.* [75]. Later, this procedure was performed for the human knee and the results were reported by Brittberg *et al.* [76]. It is a two-step surgical procedure, first the chondrocytes from patient's own knee are harvested from a less weight bearing surface. These cells are then expanded *in vitro* cultures to increase the cell yield. After suitable duration, second surgical procedure is done and the cells are re-implanted at the site of cartilage defect [77]. Autologous chondrocyte implantation has shown encouraging results for the repair of full-thickness cartilage defects in the long-term clinical evaluation studies [78]. But, the procedure is technically challenging, costly, and the availability of autologous chondrocdrocytes limit its use [79].

Matrix-induced autologous chondrocyte implantation is an improved version of the autologous chondrocyte implantation technique which provides the chondrocytes with a supportive scaffold material for the matrix formation and mechanical stability [80, 81]. These scaffolds are specifically engineered from animal-origin collagen to promote chondrocyte proliferation, differentiation, and maintenance of the chondrogenic phenotype *in vitro* [79]. The cell-seeded scaffolds are then implanted at the defect site in a way that the cell-laden side faces the subchondral bone and the low-friction surface faces the joint cavity [82]. The procedure is schematically illustrated in Figure 2.3(d). Matrix-induced autologous chondrocyte implantation technique also requires two surgical procedures, however, the use of scaffolds enables the repair of large defects, provides enhanced defect filling, and improves the overall surgical consistency [83, 84].

Some novel experimental and emerging technologies such as particulated juvenile allograft cartilage (DeNovo NT Graft; Zimmer Biomet), fresh osteochondral allografts (ProChondrix), and cryopreserved osteochondral allografts (Cartiform) are also being used [85]. In the DeNovo NT technique, ‘minced’ allograft cartilage in the form of cubes is harvested from young donors and kept viable for some time [86]. Then, similar to the autologous chondrocyte implantation and matrix-induced autologous chondrocyte implantation procedures, the cartilage lesion is debrided and filled with the cartilage allograft [87] as shown in Figure 2.3(e). Juvenile articular cartilage has a higher rate of proteoglycan and collagen synthesis as compared to an adult [88]. This technique has some advantages compared to others e.g., single-step surgical technique, no donor morbidity, and excellent integration of the transplanted tissue with the surrounding native articular cartilage [89, 90].

Despite some promising improvements in the cartilage repair techniques in recent years, the neocartilage formed from these clinical interventions still differ from the native cartilage tissue [91]. It does not have the same mechanical strength and biochemical composition as of the native tissue and often degrades over a period of time.

2.5 Hydrogels for Cartilage–Tissue Repair

Hydrogels are three-dimensional polymeric networks of high water-uptake capacity, being capable of mimicing native tissue environments [92]. Due to the potential of tailoring the structural and compositional properties of hydrogels toward relevant biological types of tissue, they are considered optimal for becoming a substitute for damaged tissue [93]. In cartilage–tissue engineering, hydrogels should provide adequate mechanical strength, physiological swelling, lubrication, and piezoelectric behavior to replicate the biomimetic environment, similar to native articular cartilage [7, 92]. With tissue-engineered hydrogel scaffolds fabricated from biologically derived or synthesized polymeric materials featuring controlled degradation profiles, the opening of voltage-activated channels of the seeded cells which is responsible for tissue growth can be achieved using external stimuli [94].

Hydrogels can be used either as acellular scaffolds or as cell-seeded biomaterials for healing the articular-cartilage defect using tissue-engineering approaches [37]. Acellular scaffolds function as cellfree implants replacing weak or damaged cartilage tissue. Efforts are made to engineer acellular biomaterial scaffolds to replicate the architectural features, mechanical properties, and thus biological functions of native cartilage tissue [95, 96]. Using cell–biomaterial combinations, the concept is to deliver suitable cell-laden biomaterials as artificial extracellular matrix to promote chondrocyte attachment and matrix formation at the defect site [95]. The aim is to present the residing cells' developmental and microenvironmental cues to trigger chondrogenesis by the presence of the surrounding hydrogel that can be further enhanced by the application of external biophysical stimuli [97, 98].

Polyelectrolyte hydrogels can be tailored to mimic the native cartilage tissue [99]. Hydrogels can either be used as acellular scaffolds for the replacement of injured tissue or as cell-seeded constituents to encourage regeneration and formation of the cartilage tissue [33, 100]. Cartilage–tissue repair approaches discussed here involve the cell-seeded hydrogel scaffolds with appropriate biophysical stimuli like electrical and osmotic stimulation to create a relatively mature cartilage before its implantation to the defect site *in vivo* [101].

2.6 Electrical Stimulation for Tissue Engineering

Various biophysical stimuli like mechanical [102], electrical [103, 104], and pulsed electromagnetic fields [105, 106] were reported for *in silico*, *in vitro*, and *in vivo* applications. In these approaches, electrical stimulation is one of the beneficial methods for enhancing cartilage–tissue repair and regeneration, while it has been less investigated as compared to mechanical stimulation and pulsed electromagnetic fields [17]. The electrical-stimulation response of articular cartilage has been investigated mainly *in vitro* and in few *in vivo* studies. There, the focus was on the medical

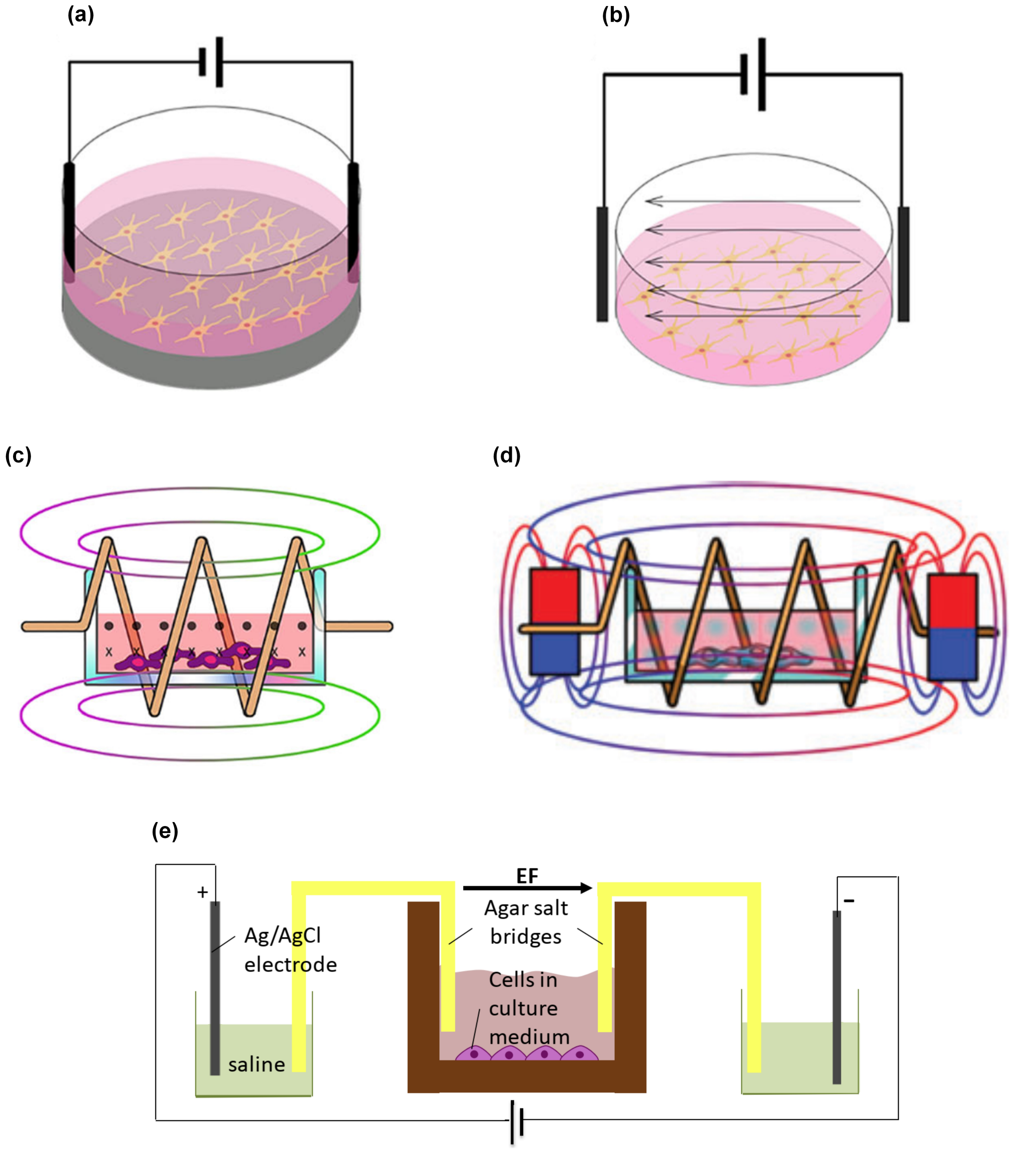
(a)
(b)
(c)
(d)
(e)
EF
+
Ag/AgCl electrode
Agar salt bridges
Cells in culture medium
saline
-

Figure 2.4: Schematic representation of various approaches for delivering electrical stimulation. **(a)** Direct stimulation, **(b)** capacitive stimulation, **(c)** inductive stimulation, **(d)** combined stimulation, **(e)** agar salt bridge configuration. The figure is taken with permission from [4–6].

and biological part of the experiment, while the electrical part has not often been investigated in detail. An option to shed light on the electrical processes are *in silico* studies. To date, only few studies have been performed *in silico* [103]. Thus, there is a need for *in silico* studies to enhance the understanding of the electrical effects and subsequently find an optimal protocol for neocartilage–tissue engineering.

The application of external electric fields is a promising therapeutic approach for healing and regeneration of the biological tissues [107]. The methods to deliver electrical stimulation can be mainly divided into three main types namely: direct coupling, capacitive coupling, and inductive coupling [4] as schematically described in Figures 2.5(a)–(c). In direct coupling, the electrodes are in contact with the sample, while the other two coupling schemes use electrodes not in direct contact of the sample [5]. Direct coupling can be used either with a direct-current or alternating-current signal, while indirect coupling always works with alternating-current signals [108].

Direct methods are widely used because of easy operation [108]. Yet, these methods have certain drawbacks like insufficient bio-compatibility of the electrodes, contact to the medium resulting in temperature rise, change in pH, and formation of harmful by-products stemming from redox reactions occurring at the electrodes [109]. On the other hand, capacitive and inductive coupling are biologically more safe as the tissue or sample is not in direct contact with the electrodes [6]. However, this method has the drawback of high voltage requirement to induce an optimal field strength and longer times of operation as compared to the direct coupling [6, 110].

There exist subtypes of the basic stimulation methods as well to optimize the electrical stimulation. For example, in the case of indirect coupling, to have optimized stimulation, the capacitive and inductive stimuli can be combined in a single setup [111] as shown in Figure 2.5(d). Similarly, in the direct-contact scheme, the electrically exposed sample could be isolated from the reactive products of electrolysis stemming from redox reactions occurring at the electrode surface [109] by using agar salt bridges [112] as shown in Figure 2.5(e). The chondrogenic differentiation of articular cartilage can be enhanced by the application of either direct or indirect electrical stimulation [26].

2.7 Computational Electromagnetics

Computational science can be regarded as intersection of the fields of applied sciences, computer sciences, and mathematics. A rapid growth in this field has been observed in recent years because of increasing collaborations among researchers of different fields, and the development of computer software and hardware [113]. Computational science has played a significant role in solving problems of many different fields including complex biological processes.

James Clark Maxwell laid the foundations of electromagnetic field theory [114]. The theory is valid in many areas of science and engineering. The Maxwell's equations are the fundamental of this theory for describing the behavior and interaction of electric and magnetic fields.

Computational electromagnetics deals with numerical methods for computationally efficient approximations to solve Maxwell's equations. These equations are explained in the following section.

2.7.1 Maxwell's Equations

In classical electromagnetic field theory, Maxwell's equations in differential form for Euclidean space can be described as [115, 116]:

$$\begin{aligned}
\nabla \times \mathbf{H} &= \mathbf{J} + \frac{\partial \mathbf{D}}{\partial t} && \text{(Ampère's law with Maxwell's extension)} \quad (2.1)\\
\nabla \times \mathbf{E} &= -\frac{\partial \mathbf{B}}{\partial t} && \text{(Faraday's law of magnetic induction)} \quad (2.2)\\
\nabla \cdot \mathbf{D} &= \rho && \text{(Gauss' law for electric fields)} \quad (2.3)\\
\nabla \cdot \mathbf{B} &= 0 && \text{(Gauss' law for magnetic fields)} \quad (2.4)
\end{aligned}$$

where $\mathbf{E}$ is the electric field intensity ($\mathrm{V\,m^{-1}}$), $\mathbf{H}$ is the magnetic field intensity ($\mathrm{A\,m^{-1}}$), $\mathbf{D}$ is the electric flux density ($\mathrm{C\,m^{-2}}$), $\mathbf{B}$ is the magnetic flux density ($\mathrm{V\,s\,m^{-2}}$), $\mathbf{J}$ is the electric current density ($\mathrm{A\,m^{-2}}$), and ρ is the electric charge density ($\mathrm{A\,s\,m^{-3}}$). All these quantities are functions of space variables x, y, z and time t.

Additionally, there exist the constitutive laws that characterize electromagnetic properties of the medium. For the linear isotropic medium these laws are,

$$\begin{aligned}
\mathbf{B} &= \mu_o \mu_r \mathbf{H} = \mu \mathbf{H} \quad (2.5)\\
\mathbf{D} &= \varepsilon_o \varepsilon_r \mathbf{E} = \varepsilon \mathbf{E} \quad (2.6)\\
\mathbf{J} &= \kappa \mathbf{E} \quad (2.7)
\end{aligned}$$

where μ, ε, and κ are the permeability ($\mathrm{V\,s\,A^{-1}\,m^{-1}}$), permittivity ($\mathrm{A\,s\,V^{-1}\,m^{-1}}$), and conductivity ($\mathrm{S\,m^{-1}}$) of the medium, respectively. μ_o is the permeability of vacuum with value $4\pi \times 10^{-7}\,\mathrm{V\,s\,A^{-1}\,m^{-1}}$ and ε_o is the permittivity of the vacuum having value $8.854 \times 10^{-12}\,\mathrm{A\,s\,V^{-1}\,m^{-1}}$.

The continuity equation governing the flux of ionic species through the hydrogel and solution is used in the following chapters which is implicit in Maxwell's equations. A short description of the continuity equation is presented below.

For any vector **A**, the relation

$$\nabla\cdot (\nabla \times \mathbf{A}) = 0 \tag{2.8}$$

is always satisfied. Applying divergence to both sides of the Ampère's law of Equation (2.1) and using Equation (2.8),

$$\nabla\cdot \left(\mathbf{J} + \frac{\partial \mathbf{D}}{\partial t}\right) = \nabla\cdot (\nabla \times \mathbf{H}) = 0. \tag{2.9}$$

Rearranging the Equation (2.9),

$$\nabla\cdot \mathbf{J} = -\frac{\partial(\nabla\cdot \mathbf{D})}{\partial t}. \tag{2.10}$$

Applying the Gauss' law for electric field given in Equation (2.3), the continuity equation is,

$$\nabla \cdot \mathbf{J} = -\frac{\partial \rho}{\partial t}. \tag{2.11}$$

In addition to the continuity equation (2.11), Poisson equation derived from the Equation (2.3) is used as well in the following chapters.

2.7.2 The Finite Element Method

In general, most of the processes in nature can be described using partial differential equations which relate different quantities of interest. Solving these equations for an arbitrary geometrical shape through classical methods is not always possible. Therefore, computational methods to solve such equations have been developed in the last decades, among which the most prominent is the finite element method. It is a rich and versatile approach for constructing computational schemes to solve governing partial differential equations for a particular domain [117]. The finite element method is a numerical technique to obtain approximate solution of a partial differential equation, interpreted as a prediction for development of the process under specific conditions [113]. This method yields a continuous solution and can easily be adapted to different geometries.

If a model expressed as a partial differential equation is given, the typical numerical solution procedure includes a discretization step to generate a mesh. The next goal is to approximate the continuous problem by a discrete model which is rewriting the partial differential equation, also called the strong form, to the Galerkin form. After this, the resulting matrix equation is solved numerically using a finite element software. Three common discretization techniques are the finite difference, finite volume, and finite elements [113]. The finite element discretizations have been used in this thesis, as they have a rich mathematical theory behind the numerical approximation, and can relatively easily handle unstructured meshes and complex domains. A general finite element formulation consists of the following steps [117]:

- Subdividing the domain of problem into finite elements.
- Element formulation by the development of equations for elements.
- Assembling equations for the entire system from individual element equations.
- Solution of equations.
- Postprocessing for determining the quantities of interest and obtaining visulizations of the results.

Consider a general form of the differential equation for a domain Ω enclosed by the boundary $\partial\Omega$ with the given boundary conditions,

$$L[p] = \zeta \tag{2.12}$$

where L is the differential operator, ζ is the source term, and p is the unknown function to be evaluated.

The basic of finite-element method is to transform the given differential equation into a system of linear equations having the form

$$\mathbf{A}\mathbf{x} = \mathbf{b}. \tag{2.13}$$

The Equation (2.13) is then computationally solved using either direct or iterative solver with $\mathbf{x}$ containing the unknown values p_i of interest. The unknown function p can be approximated as,

$$\hat{p}(x, y, z) \approx \sum_{i=1}^{N} p_i \phi_i(x, y, z) \tag{2.14}$$

where ϕ_i are the polynomial basis function and p_i belong to the vector representing degrees of freedom to be computed. In other words, p_i are the values of the unknown function p on the nodes $i(i = 1, 2, ..., N)$ of the discretization grid for domain Ω. It is an appropriate approach to find the scalar potential.

The Equation (2.12) can be rewritten as

$$L\left[\sum_{i=1}^{N} p_i\phi_i(x, y, z)\right] = \zeta. \tag{2.15}$$

The approximated form of u represented by the Equation (2.14) usually does not exactly solve the partial differential equation, instead a residual value r is left over:

$$r = L\left[\sum_{i=1}^{N} p_i\phi_i(x, y, z)\right] - \zeta \neq 0. \tag{2.16}$$

Next, N independent test or weighting functions w_j are multiplied with Equation (2.16) and integration over the complete domain Ω yields:

$$\int_\Omega r w_j d\Omega = \int_\Omega L\left[\sum_{i=1}^{N} p_i\phi_i - \zeta\right] w_j d\Omega \neq 0 \tag{2.17}$$

where $\phi_i = \phi_i(x, y, z)$. Often, the weighting functions are same as the basis functions i.e., $w_j = \phi_j$ which is called Galerkin's method [113]. The weighted residuals are then set to zero and solved for the unknowns p_i such that:

$$\int_\Omega \phi_j L\left[\sum_{i=1}^{N} p_i\phi_i - \zeta\right] d\Omega = 0. \tag{2.18}$$

Rearranging Equation (2.18),

$$\int_\Omega \phi_j L \sum_{i=1}^{N} p_i\phi_j d\Omega - \int_\Omega \zeta\phi_j d\Omega = 0. \tag{2.19}$$

Alternatively, Equation (2.18) can be written as,

$$\underbrace{\sum_{i=1}^{N} p_i}_{\mathbf{x}} \underbrace{\int_\Omega L[\phi_i]\phi_j d\Omega}_{\mathbf{A}} = \underbrace{\int_\Omega \zeta\phi_j d\Omega}_{\mathbf{b}}. \tag{2.20}$$

The term **A** has the matrix form where **A** can be calculated because the functions ϕ_i, ϕ_j, and the operator L are known. The vector **b** on the right hand side can also be calculated and the system of equations represented as $\mathbf{Ax} = \mathbf{b}$ can be solved computationally with p_i having the unknown values of interest. The system of equations can be solved computationally by using either direct or iterative solvers [115].

Some more concepts related to the finite element method are introduced in the next section in context of FEniCS.

2.8 Finite Element Computational Software Employed

Finite element computational software (FEniCS) [118, 119] is used in this thesis as the finite element solver using Python interface. FEniCS is an open source computing tool to solve differential equations. It allow users to transform physical models into finite element programs. The high level languages like Python and C++ allows utilizing its powerful capabilities and its routines can run over wide range of operating systems.

FEniCS is the collection of open-source packages to enable automated solution of differential equations. It provides scientific computing tools to deal with computational meshes, variational formulations of the partial differential equations, and linear algebra. The user of FEniCS has much control over many aspects of the model while bulk of the finite element code (i.e. assembling the matrices and solving the system) is easily handled by various FEniCS functions. Thus, FEniCS offers a more streamlined approach as compared to traditional code development techniques and also provides more flexibility than a prebuilt model [120].

In order to use FEniCS, a partial differential equation needs to be transformed into a variational problem, so it is multiplied with a test function v. The resulting equation is then integrated over the domain Ω, and integration by parts is performed for the terms with second-order derivatives. The unknown function u which is to be approximated is called a trial function. The trial and test function terms are used in FEniCS programs as well and they belong to certain function spaces that specify the properties of the functions. The function space is created by specifying the type of element and the degree of the finite element. FEniCS supports various finite element families and the notations are defined in the Periodic Table of the Finite Elements (www.femtable.org) [121].

Consider a boundary value problem involving the Poisson equation [122],

$$\begin{aligned} -\nabla^2 p &= \zeta \quad \text{in } \Omega && (2.21) \\ p &= p_o \quad \text{on } \partial\Omega && (2.22) \end{aligned}$$

where p is the unknown function, ζ is the source term, ∇^2 (or written as Δ) is the Laplace operator, Ω is the spatial domain, and $\partial\Omega$ is the boundary of Ω.

The Poisson equation (2.21) is multiplied by the test function q and integrated over Ω,

$$-\int_\Omega (\nabla^2 p) v dx = \int_\Omega \zeta q dx \tag{2.23}$$

here dx denote the differential element for integration over the domain Ω. As equation (2.23) involves second-order derivative of p, it is transformed into the first-order derivative by using the integration by parts,

$$-\int_{\Omega}(\nabla^2 p)q dx = \int_{\Omega} \nabla p \cdot \nabla q dx - \int_{\partial\Omega} \frac{\partial p}{\partial n} q ds \tag{2.24}$$

where ds is the differential element for integration over the boundary $\partial\Omega$, and $\partial p/\partial n$ is the derivative of p in the outward normal direction on the boundary. The test function v is required to vanish on parts of the boundary where solution p is known. It implies that $q = 0$ on the whole boundary $\partial\Omega$ and the second term on the right-hand side of equation (2.24) vanishes. From equations (2.23) and (2.24), it follows that

$$\int_{\Omega} \nabla p \cdot \nabla q dx = \int_{\Omega} \zeta q dx. \tag{2.25}$$

The variational problem, with suitable definition of the function spaces, and appropriate boundary conditions i.e. Dirichlet, Neumann, and Robin, uniquely define the approximate numerical solution of the given partial differential equation.

3 Electrical-Stimulation Studies of Articular Cartilage

In this chapter, reported research studies to date are summarized using either the direct or indirect electrical stimulation of chondrocytes, cartilage tissue, and cell-seeded hydrogel scaffolds. These studies have been performed for *in vivo* animal models and for *in vitro* animal as well as human samples.

3.1 Direct Coupling

3.1.1 *In Vivo* Studies

As early as 1974, Baker *et al.* [123] observed the enhancement of the latent potential for the repair of hyaline cartilage in New Zealand white rabbits by using a bimetallic device inserted into articular-cartilage defects. The repair response appeared to stem from proliferating chondrocytes and spread from the defect margin over the entire surface of the defect [123]. Later, they also reported that the regrowing potential of articular hyaline cartilage at the defect site could be enhanced by changing the electrochemical environment by the application of electrical stimulation [124]. Lippiello *et al.* [125] observed improved repair quality of the articular cartilage by application of a pulsing direct current to rabbit joints in which an osteochondral defect was surgically created.

3.1.2 *In Vitro* Studies

Electrokinetic transduction in cartilage occurs due to the presence of charged groups of the macromolecules in the extracellular matrix, mostly the proteoglycans. Frank *et al.* [19, 126] experimentally and theoretically demonstrated this transduction phenomenon in bovine articular-cartilage tissue. Later, current-generated stress was also measured, and its dependence on the applied current's amplitude and frequency was characterized [127]. Similarly, Akkin *et al.* [128] and Youn *et al.* [129] studied this phenomenon using phase-sensitive optical low coherence reflectometry (PS-OLCR) and differential-phase optical coherence tomography (DP-OCT), respectively.

In the doctoral thesis of Gray, the response of an epiphyseal plate in organ culture was determined over a current-density range of 50 to $1000\,\mu\mathrm{A\,cm^{-2}}$ at frequencies between 0.1 and 100 Hz [130]. The motivation for these experiments was to examine the sensitivity of chondrocytes to currents similar in magnitude and frequency to those expected to occur *in vivo* loading situations. MacGinitie *et al.* [131, 132] developed an experimental model to observe the effect of electrical stimulation on cartilage tissue manifesting itself in field-induced changes of stress protein and total protein synthesis. Furthermore, the choice of electrical parameters such as frequency and field magnitude that could influence the protein synthesis in cartilage explants were addressed [133]. Nogami *et al.* [134] investigated the effect of direct current electrical stimulation of $5\,\mu\mathrm{A}$ on mesenchymal cell differentiation into cartilage using bone matrix gelatin and fetal rat muscle.

Since the ability to guide chondrocyte movement may pave the way for strategies to achieve cartilage healing or repair and for further development of cartilage substitutes, Chao *et al.* [135] reported that cathodal migration occurs for cultured chondrocytes subjected to directly coupled electrical stimulation. Furthermore, an electric field was applied to chondrocytes seeded in a homogeneous agarose culture system and the changes in cell proliferation and extracellular matrix biosynthesis were quantified with an emphasis on the cellular signaling pathways responsible for the observed changes [112].

Using the three-dimensional chondrocyte–agarose model system, Akanji *et al.* [136] investigated the effects of direct current on matrix synthesis and cell proliferation. Kwon *et al.* [137] investigated the effect of electrical stimulation during chondrogenesis of mesenchymal stem cells. Most recently, it was observed by Hiemer *et al.* [138] that exposure to a directly connected alternating electric field ($0.7\,\mathrm{V_{RMS}}$, 1 kHz) significantly increased the synthesis of collagen type II in human chondrocytes under hypoxic culture conditions.

3.2 Indirect Coupling

3.2.1 *In Vivo* Studies

Farr *et al.* [139] used a capacitively coupled device in 288 patients with knee osteoarthritis and reported that those patients who received electrical stimulation for more than 750 h, profited from pain relief and hence decrease in anti-inflammatory drug use. Moreover, Garland *et al.* [140] reported that an optimized capacitively coupled electrical stimulation device for treating knee osteoarthritis significantly improved symptoms and function without causing any significant side effects.

3.2.2 *In Vitro* Studies

Rodan *et al.* [141] demonstrated that an external, capacitively coupled electric stimulation applied to chondrocytes in suspension stimulates DNA synthesis. This effect could be attributed to Ca^{+2} and Na^{+} fluxes. Fitzsimmons *et al.* [142] used the capacitively coupled pulsed electric field for human chondrocytes and, based on the results, suggested that nitric oxide is involved in the transduction pathway for chondrocyte proliferation, and that its production may be the result of a cascade involving calcium, calmodulin, and cGMP production. The capacitively coupled electric stimulation with 60 kHz and 20 mV/cm was found to be a proper and effective inducer of differentiation of human adipose-derived stem cells (ADSCs) into the chondrogenic direction [143]. Later, the same study was extended with a frequency of 1 kHz [144] showing the same principal results.

The group of Brighton *et al.* conducted many studies on the effect of capacitively coupled electric stimulation on chondrocyte proliferation [145–150]. In one of their first studies, they observed that articular cartilage chondrocytes from Holstein calf in pellet form showed increased glycosaminoglycan synthesis or increased cell proliferation by appropriate capacitively coupled electric stimulation [145]. Similarly, they observed upregulation of gene expression as well as the matrix accumulation of structural cartilage macromolecules (such as type II collagen and aggrecan) with specific capacitively coupled electric stimulation *in vitro* [146]. Later, this study was extended to adult bovine articular cartilage explants, and similar positive results could be reported [147].

Brighton *et al.* [148] observed significant upregulation of cartilage matrix protein expression and production while simultaneously significantly attenuating the upregulation of metalloproteinase expression by the use of capacitively coupled electric stimulation. Thus, it was concluded that the use of electrical stimulation to both diminish matrix destruction and increase matrix production has promising potential to noninvasively treat osteoarthritis patients. The mechanisms through which capacitively coupled electric stimulation stimulates matrix production and inhibits matrix destruction were previously unknown. Thus, Xu *et al.* [149] conducted a study to ascertain that the effect of electrical stimulation does not involve intracellular Ca^{+2} repositories but solely extracellular Ca^{+2} influx via voltage-gated calcium channels. At the same time, calmodulin, calcineurin, and the nuclear factor of activated T-cells (NF-AT) decrease rather than phospholipase C and IP_3. Finally, they reported the use of reflectance spectrophotometric analysis to demonstrate the structural modification of osteoarthritic articular human cartilage explants [150].

The capability of adipose-derived stem cells was assessed to differentiate into osteocytes, chondrocytes, or adipocytes. Clear patterns of differentiation into three cell lineages were observed after two weeks in differentiating medium [151]. Recently, Vaca-González *et al.* [152] presented a combined computational and experimental approach to better understand hyaline-cartilage biology and its response to electrical stimulation using different *in vitro* models in three different scenarios. Initially, cell proliferation and the glycosaminoglycans synthesis of chondrocytes, cultured in a monolayer and stimulated with electric fields, were analyzed. Then, histomorphometric analysis was performed to chondroepiphysis explants that were electrically stimulated [153]. Finally, the effects of electrical stimulation on chondrogenic differentiation of mesenchymal stem cells cultured in hydrogels were assessed [154].

All the *in vitro* and *in vivo* electrical stimulation studies which have been noted in this chapter using either direct or indirect electrical stimulation for the chondrocytes, cartilage tissue samples, and cell-seeded hydrogel scaffolds are summarized in the Table 3.1.

3.3 Concluding Remarks

It is evident that both direct and indirect electrical stimulation could be beneficial for cartilage–tissue engineering approaches. However, a complete understanding of the transduction pathways and interaction mechanisms due to electrical stimulation is still lacking for designing an optimized electrical-stimulation protocol. Moreover, there is a lack of standard documentation format of electrical stimulation experiments and sometimes it is not clear which stimulation parameters have exactly been used.

Table 3.1: Electrical stimulation studies of articular cartilage.

Coupling	*Model*	*Study*	*Type*
direct coupling	*in vivo*	Baker *et al.* [123]	Rabbit knee
		Baker *et al.* [124]	Rabbit knee
		Lippiello *et al.* [125]	Rabbit knee
	in vitro	Frank *et al.* [126]	Bovine knee plug
		Berkenblit *et al.* [127]	Bovine knee disc
		Akkin *et al.* [128]	Porcine nasal sample
		Youn *et al.* [129]	Porcine nasal sample
		Gray *et al.* [130]	Calf epiphyseal plate cartilage
		MacGinitie *et al.* [131–133]	Calf chondrocytes in agarose gel
		Nogami *et al.* [134]	Rat MSCs in bone gelatin
		Chao *et al.* [135]	Bovine articular chondrocytes
		Szasz *et al.* [112]	Calf chondrocytes in agarose gel
		Akanji *et al.* [136]	Steer chondrocytes in agarose gel
		Kwon *et al.* [137]	Mouse MSCs
		Hiemer *et al.* [138]	Human chondrocytes
indirect coupling	*in vivo*	Farr *et al.* [139]	Human knee
		Garland *et al.* [140]	Human knee
	in vitro	Rodan *et al.* [141]	Chick chondrocytes
		Fitzsimmons *et al.* [142]	Human chondrocytes
		Mardani *et al.* [144]	Human ADSCs
		Esfandiari *et al.* [143]	Human ADSCs
		Brighton *et al.* [145]	Calf chondrocytes
		Wang *et al.* [146]	Bovine chondrocytes
		Brighton *et al.* [147]	Cow knee cartilage plugs
		Brighton *et al.* [148]	Human knee cartilage plugs
		Xu *et al.* [149]	Bovine knee chondrocytes
		Brighton *et al.* [150]	Human knee cartilage plugs
		Hernández-Bule *et al.* [151]	Human ADSCs
		Vaca-González *et al.* [152]	Rat chondrocytes
		Vaca-González *et al.* [153]	Rat chondrocytes
		Vaca-González *et al.* [154]	Porcine MSCs

*MSCs, mesenchymal stem cells; ADSCs, adipose derived stem cells.

4 Continuum Mechanics: Framework for Modeling Cartilage Properties

4.1 Overview

Hyaline cartilage undergoes many substantial age-related physiochemical and biomechanical changes that reduce its ability to overcome the effects of mechanical stress and injury. In quest of therapeutic options, electromagnetic and electrical stimulation have been proposed for improving tissue engineering approaches for the repair of articular cartilage. The aim of this chapter is to summarize *in silico* investigations involving induced electrical properties of cartilage tissue due to various biophysical stimuli along their respective mathematical descriptions.

4.2 Continuum Mechanics

Using continuum mechanics, poroelastic and mixture formulations are commonly employed to describe the mechanics and electrical properties of connective tissues like cartilage [155]. In the poroelastic model, material is considered as a porous elastic solid, saturated by the pore fluid which flows relative to the deforming solid. This model is further classified into porohyperelastic (PHE) [155], poroviscoelastic (PVE) [156], and poroviscohyperelastic (PVHE) models [157]. In the mixture model, material is considered a continuum mixture of a deformable solid phase and a fluid phase. This model is further characterized as biphasic [21], triphasic [158], and quadphasic [159], and then generalized to a multiphasic model [160].

The biphasic theory models the tissue as a homogeneous mixture of two phases: a charged porous permeable solid phase (collagen-proteoglycan matrix) and an interstitial fluid phase [161]. In triphasic theory, two phases are same as in the biphasic model, and third, an ion phase with two species (anion and cation) is added [158]. The quadphasic theory considers the ionic phase further divided into cation and anion phases [159], and finally, the multiphasic theory consists of multielectrolytes in addition to a solid and a fluid phase [160]. The basic structure of the articular cartilage is schematically illustrated in Figure 4.1. When applied to biomechanical studies, the poroelastic and biphasic mixture models are equivalent.

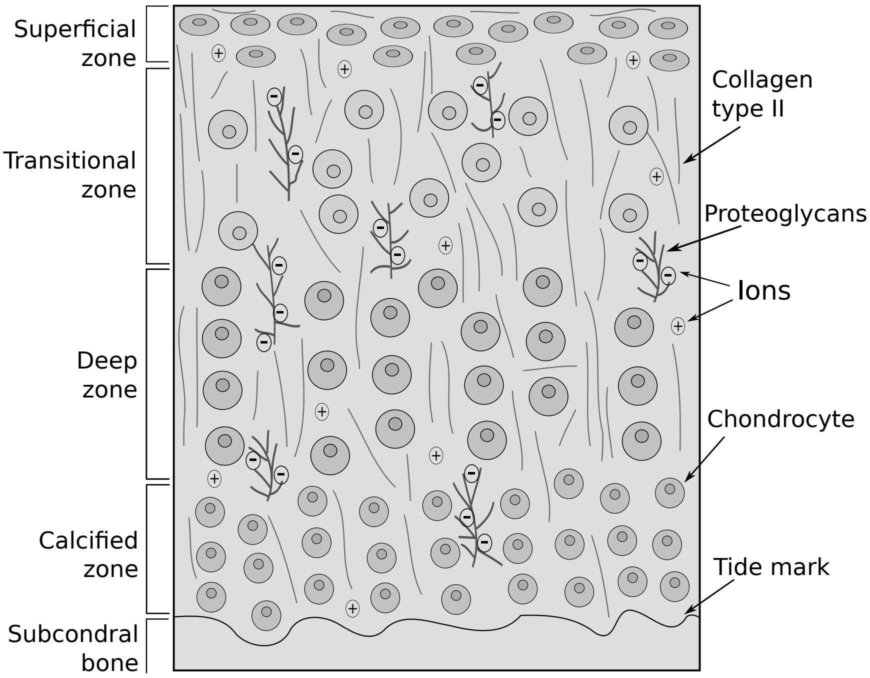

Figure 4.1: Schematic illustration of composition and structure of articular cartilage lining the bone adapted from Servin-Vences *et al.* [1] (not drawn to scale).

Although most of the continuum mechanics formulations mentioned have been used in literature to discuss the induced electrical properties of cartilage, the triphasic theory is considered the most appropriate for *in silico* description of the induced electrical properties of cartilage tissue due to various biophysical stimuli [162].

Following the approach developed by Lai *et al.* [158] and Gu *et al.* [163], a charged hydrated soft tissue is modeled as a continuum mixture consisting of solid phase, interstitial fluid phase, and k different species of monovalent or multivalent ions. Thus, there are a total of $k+2$ constituents in the tissue. Any component other than water and mobile ions within a tissue is considered the solid phase in this model. Unless stated otherwise, $\alpha = s, w, k$ always represents solid, fluid, and ionic constituents of the mixture, respectively, in the discussion to follow. For the case of biphasic theory ($\alpha = s, w$) and for the triphasic and multiphasic theories ($\alpha = s, w, k$), where $k = 1, 2, 3, ..., n$ are n ionic species of the mixture. The true mass density ρ_T^α for a component α in the mixture is given by

$$\rho_T^\alpha = \frac{m^\alpha}{V^\alpha}, \tag{4.1}$$

where m^α is the mass of component α and V^α is the true volume of phase α. The local apparent mass density ρ^α is defined as follows:

$$\rho^\alpha = \frac{m^\alpha}{V}, \tag{4.2}$$

where V is the total volume of the mixture. The volume fraction ϕ^α of each phase α is given by

$$\phi^\alpha = \frac{V^\alpha}{V}. \tag{4.3}$$

If α is w, then ϕ^w is the porosity, which is the volume fraction of the extrafibrillar water available to fixed charges on the proteoglycans [164]. If α is s, then ϕ^s is solidity of the tissue. From Equations (4.1)–(4.3), ρ^α can be related to the true density ρ^α_T by

$$\rho^\alpha = \phi^\alpha \rho^\alpha_T. \tag{4.4}$$

The apparent densities of ion species can also be written as follows:

$$\rho^k = c^k M^k \phi^w \tag{4.5}$$

where c^k and M^k are the concentration and molar weight of the kth ionic species, respectively, and ϕ^α satisfies the following saturation condition of the mixture,

$$\phi^s + \phi^w + \sum_{k=1}^{n} \phi^k = 1. \tag{4.6}$$

The law of mass conservation requires that the velocities of the solid, liquid, and ionic phases must satisfy the continuity equation

$$\frac{\partial \rho^\alpha}{\partial t} + \nabla \cdot (\rho^\alpha \mathbf{v}^\alpha) = 0 \tag{4.7}$$

where $\mathbf{v}^\alpha$ is the velocity of component α.

The total density of the mixture, i.e. the tissue, is

$$\rho_{mix} = \sum_{\alpha=s,w,k} \rho^\alpha = \sum_{\alpha=s,w,k} \phi^\alpha \rho^\alpha_T. \tag{4.8}$$

From Equations (4.4)–(4.7), assuming the true densities are constant, the continuity equation for the mixture can be written as follows:

$$\nabla \cdot \left(\phi^s \mathbf{v}^s + \phi^w \mathbf{v}^w + \mathbf{v}^k \sum_{k=1}^{n} \phi^k \right) = 0. \tag{4.9}$$

The electroneutrality condition is as follows:

$$z^F c^F + \sum_{k=1}^{n} z^k c^k = 0 \tag{4.10}$$

in which z^k is the valence (including sign, positive for cations and negative for anions) of ion k and c^F represents the fixed charge density. In Equation (4.10), the solid matrix is assumed to be negatively charged.

As in the triphasic theory, the fixed charges on the solid phase are conserved, so the fixed charge density is a function of tissue deformation and water volume fraction (porosity). Thus,

$$\frac{\partial(\phi^w c^F)}{\partial t} + \nabla\cdot(\phi^w c^F \mathbf{v}^s) = 0 \tag{4.11}$$

or it can be expressed with the tissue deformation as follows:

$$c^F = \frac{c_o^F}{1 + \mathrm{tr}(\mathbf{S})/\phi_o^w} \tag{4.12}$$

where $\mathbf{S}$ is the strain tensor measured from the physicochemical reference configuration corresponding to a hypertonic salt bath and $\mathrm{tr}(\mathbf{S})$ is the trace of the strain tensor. The solidity of the tissue is expressed as

$$\phi^s = \frac{\phi_o^s}{1 + \mathrm{tr}(\mathbf{S})}. \tag{4.13}$$

Since the values of ϕ^k are small in magnitude as compared to ϕ^s and ϕ^w, the saturation condition (4.6) can be written as $\phi^s + \phi^w = 1$, and the following is obtained:

$$\phi^w = 1 - \frac{\phi_o^s}{1 + \mathrm{tr}(\mathbf{S})} \tag{4.14}$$

where c_o^F, ϕ_o^s and ϕ_o^w represent the fixed charge density, and the volume fractions of solid and water phases in the reference configuration, respectively.

If the gravity and magnetic effects are neglected, the gradients of the chemical and electrochemical potential, respectively, are the only driving forces, balanced by the frictional forces between different phases for their movement. The momentum equations for the tissue, water, anion, and cation are as follows:

$$\nabla\cdot\sigma = 0 \tag{4.15}$$

$$-\rho^\alpha \nabla\mu^\alpha + K^\alpha = 0 \tag{4.16}$$

where K^α can be written as

$$K^\alpha = \sum_{\beta=s,w,k}^{n} f_{\alpha\beta}(\mathbf{v}^\beta - \mathbf{v}^\alpha), \qquad (\alpha = s, w, k). \tag{4.17}$$

Here, σ is the total stress of the mixture (tissue) and μ^α is the electrochemical potential of phase α, respectively. The parameters $f_{\alpha\beta}$ are the frictional coefficients per unit tissue volume between the interdiffusing α and β components. Following the classical mixture theories, it is assumed that $f_{\alpha\beta} = f_{\beta\alpha}$ holds in consistence with the Onsager reciprocity relations [165, 166].

If both the body and the inertial forces are neglected, the governing equations of the multiphasic model can then be derived as follows:

$$\sigma = -P\mathbf{I} + \lambda_s \mathrm{tr}(\mathbf{S})\mathbf{I} + 2\mu_s\mathbf{S} \tag{4.18}$$

$$\mu^w = \mu_o^w + \frac{1}{\rho_T^w}\left(P - RT\sum_{k=1}^{n}\varphi^k c^k + B_w \mathrm{tr}(\mathbf{S})\right) \tag{4.19}$$

$$\mu^k = \mu_o^k + \frac{RT}{M^k}\ln(\gamma_k c^k) + z^k\frac{F_c\psi}{M^k}. \tag{4.20}$$

Here, R is the universal gas constant, F_c is the Faraday constant, γ_k are the activity coefficients of kth ionic species, μ_o^α $(\alpha = w, k)$ are the chemical potential of phase α at the reference configuration, $\mathbf{I}$ is the identity tensor, φ^k is the osmotic coefficient of ion k, and B_w is the coupling coefficient.

The laws for linear electrokinetic transduction in isotropic media [167, 168] can be used to relate the relative fluid velocity $\mathbf{U}$ and the current density $\mathbf{J}$ in the tissue to the gradients in fluid pressure P and electrical potential ψ without considering the effects of diffusion potential [162],

$$\begin{aligned} \mathbf{U} &= -k_{11}\nabla P + k_{12}\nabla\psi \\ \mathbf{J} &= k_{21}\nabla P - k_{22}\nabla\psi \end{aligned} \tag{4.21}$$

where k_{11} is the “short-circuit” hydraulic permeability, k_{12} and k_{21} are the electrokinetic coupling coefficients that are equal ($k_{12} = k_{21}$) by the Onsager reciprocity theorem [165, 166], and k_{22} is the electrical conductivity. The coupling coefficients can be expressed in terms of the fixed charge density of the cartilage extracellular matrix using the microscopic continuum models for cartilage [169]. The fixed charge density is negative for materials like cartilage, so k_{12} and k_{21} are defined negative.

Inversion of Equation (4.21) leads to the expressions for gradients of pressure and potential,

$$\begin{aligned} \nabla P &= -b_{11}\mathbf{U} + b_{12}\mathbf{J} \\ \nabla\psi &= b_{21}\mathbf{U} - b_{22}\mathbf{J} \end{aligned} \tag{4.22}$$

where b_{11} is the (open-circuit) Darcy hydraulic resistivity, b_{12} and b_{21} are the coupling coefficients that are equal ($b_{12} = b_{21}$) according to the Onsager reciprocity theorem [165, 166], and b_{22} is the (no flow) electrical resistivity.

If the change in electric potential is required, then Equation (4.21) can be reformulated to obtain the following:

$$\begin{aligned} \nabla\psi &= k_e \nabla P - \frac{1}{k_{22}}\mathbf{J} \\ \mathbf{U} &= -k_d \nabla P - k_i \mathbf{J} \end{aligned} \tag{4.23}$$

where $k_d = k_{11} - (k_{12}k_{21}/k_{22})$, $k_e = k_{21}/k_{22}$, and $k_i = k_{12}/k_{22}$. Note that k_d is the open-circuit hydraulic (Darcy) permeability.

For the case of triphasic materials, the relative water volume flux $\mathbf{J}^w$ and ionic molar flux $\mathbf{J}^k$ are defined as follows [170]:

$$\mathbf{J}^w = \phi^w(\mathbf{v}^w - \mathbf{v}^s) \tag{4.24}$$

and

$$\mathbf{J}^k = \phi^k c^k(\mathbf{v}^k - \mathbf{v}^s) \tag{4.25}$$

where the fluid $\mathbf{v}^w$ and ion velocities $\mathbf{v}^k$ are defined as

$$\mathbf{v}^w = -\left[\rho^w \nabla\mu^w + \rho^+ \nabla\mu^+ + \rho^- \nabla\mu^-\right]/f_{ws} \tag{4.26}$$

$$\mathbf{v}^+ = -\left[\rho^w \nabla\mu^w + \rho^+(1 + f_{ws}/f_{w+})\nabla\mu^+ + \rho^- \nabla\mu^-\right]/f_{ws} \tag{4.27}$$

$$\mathbf{v}^- = -\left[\rho^w \nabla\mu^w + \rho^+ \nabla\mu^+ + \rho^-(1 + f_{ws}/f_{w-})\nabla\mu^-\right]/f_{ws}. \tag{4.28}$$

Similarly, the electrical current density inside the tissue assuming k ion species is

$$\mathbf{J} = F_c\phi^w \left(\sum_{k=1}^{n} z^k c^k \mathbf{v}^k + z^F c^F \mathbf{v}^s\right) = F_c \sum_{k=1}^{n} z^k \mathbf{J}^k \tag{4.29}$$

or it can also be written as

$$\mathbf{J} = F_c\left(\mathbf{J}^+ - \mathbf{J}^-\right) = F_c\phi^w[c^+(\mathbf{v}^+ - \mathbf{v}^s) - c^-(\mathbf{v}^- - \mathbf{v}^s)]. \tag{4.30}$$

Thus, from Equations (4.5), (4.10), (4.24), and (4.30), the relations for water flux and the electrical current density are [170],

$$\begin{aligned} \mathbf{J}^w &= -k_{11}\nabla P + k_{12}\nabla\psi \\ \mathbf{J} &= k_{21}\nabla P - k_{22}\nabla\psi \end{aligned} \tag{4.31}$$

where the values of the coefficients can be expressed as follows, while neglecting osmotic and strain effects:

$$\begin{aligned}
k_{11} &= -\frac{(\phi^w)^2}{f_{ws}} \\
k_{12} &= k_{21} = -c^F F_c \frac{(\phi^w)^2}{f_{ws}} \\
k_{22} &= -(F_c \phi^w)^2 \left[\frac{(c^+)^2}{f_{w+}} + \frac{(c^F)^2}{f_{ws}} + \frac{(c^-)^2}{f_{w-}} \right].
\end{aligned} \tag{4.32}$$

If the quadphasic mixture theory is considered, it consists of four components: solid (s), water (w), cations ($+$), and anions ($-$). There are two phases: a solid (s) and a fluid (f) phase. A distinction is made here between the water and fluid. In this case, the fluid phase consists of three components: the water, the cations, and the anions. The relationships for the relative fluid and ion fluxes to the gradients in fluid pressure, ion concentrations, and the electrical potential are as follows [159, 171]:

$$\mathbf{J}^w = -\mathbf{K}[\nabla P + (\varphi^w - \varphi^+)RT\nabla c^+ + (\varphi^w - \varphi^-)RT\nabla c^- + z^F c^F F_c \nabla\psi] \tag{4.33}$$

$$\mathbf{j}^k = -\mathbf{D}^k[(2 - \varphi^k)\nabla c^k + z^k \frac{F_c}{RT} c^k \nabla\psi + \frac{M^k}{RT} c^k \nabla P], \tag{4.34}$$

where $\mathbf{J}^w = \phi^w(\mathbf{v}^w - \mathbf{v}^s)$ and $\mathbf{j}^k = c^k(\mathbf{v}^k - \mathbf{v}^s)$ are the relative fluid and ion fluxes, respectively, $\mathbf{K}$ is the hydraulic permeability tensor, $\mathbf{D}^k$ is the diffusion tensor of ion k, and φ^w is the osmotic coefficient of the water component.

4.2.1 Triphasic Theory with Diffusion Potential

The magnitude and polarity of the resultant electric potential for the cartilage tissue depend on the relative magnitudes of the streaming potential and diffusion potential. The streaming potential is caused by a pressure gradient (hydraulic and/or osmotic), while the diffusion potential arises by the gradients of mobile ions in the presence of a fixed charge density gradient [162].

As the fixed charge density of cartilage tissue is non-uniform (intrinsic and/or induced by matrix deformation), so for the studies involving the mechano-electrochemical responses of the cartilage, the existence of a diffusion potential should not be neglected.

If this effect is also considerd, Equation (4.31) for the linear electrokinetic transduction becomes as follows [160, 162]:

$$\mathbf{J}^w = -k_o \nabla P - \sum_{k=1}^{n} b_k \nabla \left(\frac{RT}{z^k F_c} \ln(\gamma_k c^k) \right) - \chi_o \nabla \psi \tag{4.35}$$

$$\mathbf{J} = -g_o \nabla P - \sum_{k=1}^{n} g_k \nabla \left(\frac{RT}{z^k F_c} \ln(\gamma_k c^k) \right) - \chi_o \nabla \psi \tag{4.36}$$

where $k_o, b_k, g_o, g_k,$ and χ_o are material parameters that are functions of the ion concentrations and the frictional coefficients $f_{\alpha\beta}$ between α and β constituents.

When external circuits are not provided for the tissue to sustain a net charged flow of ions and electrons, the tissue is in a state of zero current. For such cases, at every point in the tissue, the sum of three currents must vanish, that is, $\mathbf{J} =$ Convection Current + Diffusion Current + Conduction Current = 0 or, from Equation (4.36), the gradient of the electric potential becomes as follows:

$$\nabla \psi = \left[-g_o \nabla P - \sum_{k=1}^{n} g_k \nabla \left(\frac{RT}{z^k F_c} \ln(\gamma_k c^k) \right) \right] / \chi_o. \tag{4.37}$$

For this case, there is no externally applied electric potential; the potential is entirely induced by the convection current and the diffusion current. This induced potential generates a conduction current to oppose the convection and diffusion currents to achieve the zero-current condition.

4.2.2 Modified Triphasic Theory

An equivalent formulation for the triphasic theory has been proposed, which allows easy implementation for the finite element analysis [172]. By using a simple transformation, the modified electrochemical/chemical potential functions are defined as follows:

$$\varepsilon^w = \frac{\rho_T^w(\mu^w - \mu_o^w)}{RT} = \frac{P}{RT} - \phi(c^+ - c^-) + \frac{B_w}{RT}\mathrm{tr}(\mathbf{S}) \tag{4.38}$$

$$\varepsilon^+ = \exp\left[\frac{M^+(\mu^+ - \mu_o^+)}{RT} \right] = \gamma_+ c^+ \exp\left(\frac{F_c \psi}{RT} \right) \tag{4.39}$$

$$\varepsilon^- = \exp\left[\frac{M^-(\mu^- - \mu_o^-)}{RT} \right] = \gamma_- c^- \exp\left(-\frac{F_c \psi}{RT} \right). \tag{4.40}$$

With the above definitions, the solid displacement $\mathbf{u}^s$ (for infinitesimal deformation, it is related to the solid matrix velocity $\mathbf{v}^s$ as $\mathbf{v}^s = \partial \mathbf{u}^s / \partial t$) and modified chemical potentials ε^w and ε^k compose the four primary unknowns of the system; all the other unknowns can be derived from them. Multiplying Equations (4.39) and (4.40),

$$\varepsilon^{+}\varepsilon^{-} = \gamma_{+}\gamma_{-}c^{+}c^{-}. \tag{4.41}$$

Substituting Equation (4.41) in the electroneutrality Equation (4.10),

$$c^{+} = \frac{1}{2}\left(c^{F} + \sqrt{(c^{F})^{2} + \frac{4\varepsilon^{+}\varepsilon^{-}}{\gamma_{+}\gamma_{-}}}\right) \tag{4.42}$$

$$c^{-} = \frac{1}{2}\left(-c^{F} + \sqrt{(c^{F})^{2} + \frac{4\varepsilon^{+}\varepsilon^{-}}{\gamma_{+}\gamma_{-}}}\right) \tag{4.43}$$

Similarly, from Equations (4.39) and (4.40), the electric potential is,

$$\psi = \frac{RT}{2F_{c}}\ln\left(\frac{\gamma_{-}c^{-}\varepsilon^{+}}{\gamma_{+}c^{+}\varepsilon^{-}}\right). \tag{4.44}$$

With the triphasic momentum Equations (4.15) and (4.16), all the fluxes can be expressed with the combination of the gradients of the chemical potentials as follows:

$$\mathbf{J}^{w} = -\frac{RT\phi^{w}}{\xi}\left(\nabla\varepsilon^{w} + \frac{c^{+}}{\varepsilon^{+}}\nabla\varepsilon^{+} + \frac{c^{-}}{\varepsilon^{-}}\nabla\varepsilon^{-}\right) \tag{4.45}$$

$$\mathbf{J}^{+} = -\frac{RT\phi^{w}c^{+}}{\xi}\nabla\varepsilon^{w} - \frac{RT\phi^{w}c^{+}c^{-}}{\xi\varepsilon^{-}}\nabla\varepsilon^{-} - \left[\frac{\phi^{w}c^{+}D^{+}}{\varepsilon^{+}} + \frac{RT\phi^{w}(c^{+})^{2}}{\xi\varepsilon^{+}}\right]\nabla\varepsilon^{+} \tag{4.46}$$

$$\mathbf{J}^{-} = -\frac{RT\phi^{w}c^{-}}{\xi}\nabla\varepsilon^{w} - \frac{RT\phi^{w}c^{+}c^{-}}{\xi\varepsilon^{+}}\nabla\varepsilon^{+} - \left[\frac{\phi^{w}c^{-}D^{-}}{\varepsilon^{-}} + \frac{RT\phi^{w}(c^{-})^{2}}{\xi\varepsilon^{+}}\right]\nabla\varepsilon^{-}. \tag{4.47}$$

In the above derivation, the following relations have been used [168, 173]:

$$\begin{aligned} f_{sw} &= \xi\phi^{w} \\ f_{+w} &= \frac{RT\phi^{w}c^{+}}{D^{+}} \\ f_{-w} &= \frac{RT\phi^{w}c^{-}}{D^{-}} \end{aligned} \tag{4.48}$$

where ξ is the drag coefficient between the solid and water phase, and D^{+} and D^{-} are the diffusivities of the cation and anion, respectively. ξ, D^{+}, and D^{-} were assumed to be constants. In the triphasic theory, the hydraulic permeability k is related to ξ by

$$k = \frac{\phi^{w}}{\xi} = \frac{(\phi^{w})^{2}}{f_{ws}} \tag{4.49}$$

and f_{+s}, f_{-s}, f_{+-}, and f_{-+} are neglected [159, 174]. With the four primary unknowns and the definitions of fluxes, the governing equations can be written as follows:

$$\nabla\cdot\sigma = 0 \tag{4.50}$$

$$\nabla\cdot\mathbf{v}^s + \nabla\cdot\mathbf{J}^w = 0 \tag{4.51}$$

$$\frac{\partial\phi^w c^+}{\partial t} + \nabla\cdot\mathbf{J}^+ + \nabla\cdot(\phi^w c^+\mathbf{v}^s) = 0 \tag{4.52}$$

$$\frac{\partial\phi^w c^-}{\partial t} + \nabla\cdot\mathbf{J}^- + \nabla\cdot(\phi^w c^-\mathbf{v}^s) = 0. \tag{4.53}$$

All flux quantities must be calculated relative to the porous-permeable solid matrix. Using the triphasic momentum equations and writing the fluxes with combination of the gradients of chemical potentials, that is, using Equation (4.30) [158, 172], the electrical current density can be expressed with the modified electrochemical potentials as follows:

$$\mathbf{J} = \left(-\frac{\phi^w c^+ D^+}{\varepsilon^+}\nabla\varepsilon^+ + \frac{\phi^w c^- D^-}{\varepsilon^-}\nabla\varepsilon^-\right) + c^F\mathbf{J}^w. \tag{4.54}$$

By considering the triphasic constitutive equations, the electrical current density can be expressed as follows:

$$\mathbf{J} = \phi^w(D^-\nabla c^- - D^+\nabla c^+) - \frac{F_c}{RT}\phi^w(c^+D^+ + c^-D^-)\nabla\psi + c^F\mathbf{J}^w. \tag{4.55}$$

In the above equation, the three terms are the diffusion current due to the ion concentration gradients, the conductive current due to the electrical potential gradient, and the streaming current due to the water convection, respectively. Under a condition with no current, $\mathbf{J} = 0$, the electrical potential gradient can be expressed as

$$\nabla\psi = \frac{RT}{F_c}\frac{D^-\nabla c^- - D^+\nabla c^+}{\phi^w(c^+D^+ + c^-D^-)} + \frac{RT}{F_c}\frac{c^F}{\phi^w(c^+D^+ + c^-D^-)}\mathbf{J}^w \tag{4.56}$$

that is, the electrical potential ψ consists of two components, the diffusion potential due to the ion concentration gradients and the streaming potential due to the water convection. This is consistent with the existing literature on this subject [168], which is the most recent to our knowledge, although it dates back to 1965.

4.3 Electrical Properties of Cartilage for *In Silico* Studies

The electromechanical properties of articular cartilage arise from the electrically charged nature of the tissue and its depth-dependent properties. There exists a unique environment in which chondrocytes are exposed to multiple biophysical cues [104]. The extracellular matrix of the cartilage and its associated interstitial water, solutes, and ions are considered as a signal transducer receiving input in the form of biophysical stimuli generating different signals for the growth and maintenance of the tissue [13]. Various configurations used for *in silico* investigation of electrical properties of the cartilage have been schematically represented in Figure 4.2. In this section, the electrical properties of cartilage due to different biophysical stimuli are summarized as described in literature.

4.3.1 Electrical Stimulation

To our knowledge, only eight *in silico* studies are available in literature where the cartilage tissue has been discussed with regard to direct electrical stimulation [19, 163, 174–179]. Frank and Grodzinsky formulated a continuum model for the one-dimensional linear electrokinetic transduction in a bovine cartilage sample. They derived analytical expressions for the streaming potential and the current induced by oscillatory, uniaxially confined compression of the tissue. Furthermore, they deduced expressions for the mechanical stress generated by a current density or potential difference applied to the tissue and compared these results to their own experimental results [19]. Later, Sachs and Grodzinsky extended this problem with two-dimensional applied current density instead of one-dimensional and considered the cartilage tissue that was finite in thickness, while infinite in length [178]. Furthermore, Kojic *et al.* [176, 177] reproduced the same experimental results numerically using a finite-element package for structural analysis (PAK). Ateshian *et al.* [179] simulated the current-generated stress phenomenon in FEBio [180] using the triphasic material theory [158], but they did not compare their results to the experimental study reported by Frank and Grodzinsky [19].

Gu *et al.* [174] studied the cartilage fluid flow and ion transport effects under an applied streaming current or potential using the triphasic theory. In another study, they reported the transport of interstitial water and ions in charged hydrated soft tissue like cartilage using a continuum mixture model, while also considering the electrical effects [163]. Furthermore, they derived the well-known Hodgkin-Huxley equation for the resting potential of the cell membrane and investigated the phenomenon of electro-osmotic flow in charged hydrated soft tissue [163]. Finally, Levenston *et al.* [175] proposed a finite deformation theory for the analysis of confined compression configuration for a disk of cartilage and studied the electrokinetic phenomenon for the cartilage tissue.

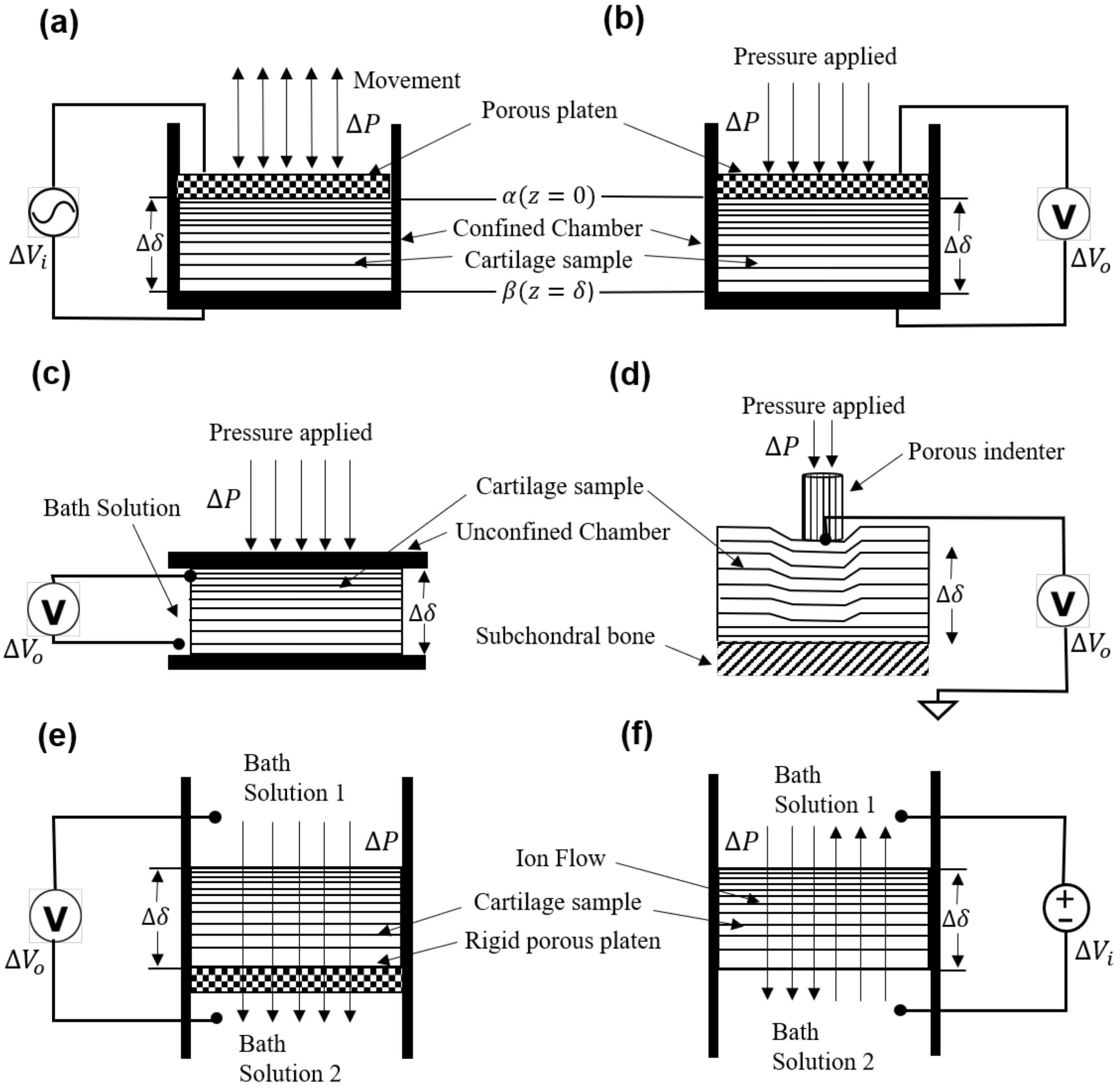
(a)
Movement
ΔP
Porous platen
ΔV_i
$\Delta\delta$
$\alpha(z = 0)$
Confined Chamber
Cartilage sample
$\beta(z = \delta)$
(b)
Pressure applied
ΔP
$\Delta\delta$
V
ΔV_o
(c)
Pressure applied
Bath Solution
ΔP
Cartilage sample
Unconfined Chamber
V
ΔV_o
$\Delta\delta$
(d)
Pressure applied
ΔP
Porous indenter
$\Delta\delta$
V
ΔV_o
Subchondral bone
(e)
Bath Solution 1
ΔP
V
ΔV_o
$\Delta\delta$
Cartilage sample
Rigid porous platen
Bath Solution 2
(f)
Bath Solution 1
ΔP
Ion Flow
$\Delta\delta$
+ −
ΔV_i
Bath Solution 2

Figure 4.2: Schematic representation showing various approaches to observe the electrical properties in cartilage tissue. **(a)** Electrical stimulation, **(b)** confined compression, **(c)** unconfined compression, **(d)** indentation, **(e)** permeation configuration, **(f)** electro-osmosis/diffusion (without V_i). ΔP is the change in pressure, $\Delta\delta$ is the change in thickness of the cartilage sample, ΔV_i and ΔV_o are the change in input and output voltages, respectively.

4.3.2 Mechanical Stimulation

The application of mechanical stimulation generates electrical streaming potentials which can influence the chondrocyte metabolism and thus enhance the tissue growth [27]. There are *in silico* studies available where electrical properties of the cartilage tissue have been investigated due to mechanical stimulation. Lee *et al.* [181] measured simultaneously the dynamic streaming potential amplitude with the stiffness for a disk of normal articular cartilage in oscillatory confined compression over a frequency range of 0.001–20 Hz relevant to impact loading. Then, theoretical and measured values of the streaming potential and stiffness were compared [181].

Kim *et al.* [182] analyzed the streaming potential behavior of cartilage in unconfined compression and they compared to their analytical poroelastic model which can predict the oscillatory streaming potential, stiffness, and the spatial profiles of the physical stimuli. Similarly, Chen *et al.* [183] theoretically predicted the streaming potential response of cartilage in the confined compression creep configuration and then tested these predictions through experiments in normal and proteoglycan-depleted tissue using biphasic theory along with the laws of linear electrokinetic transduction. In another study, Chen *et al.* [184] tested the full-thickness bovine articular cartilage by oscillatory confined compression superimposed on a static offset up to 45%. With that data fit, they obtained the electrokinetic coefficient assuming homogeneity [184].

The objective of the study performed by Lai *et al.* [162] was to determine the nature of electric fields inside an articular cartilage, while accounting for the effects of both streaming potential and diffusion potential. In the said study, the transient one-dimensional confined compression, stress-relaxation problem (in an open-circuit condition) using the triphasic theory was discussed to calculate the compressive strain, electric potential, and the fixed charge density inside the cartilage [162]. Similarly, Lai *et al.* [185] also provided a complete description of the electric field in and around a cell inside a layer of tissue in a one-dimensional confined compression stress relaxation experiment incorporating the triphasic theory.

Frijns *et al.* [171, 186] using a mixed finite-element method and quadphasic theory, simulated the mechanical and electrical behavior of a cartilage substitute caused by a change in the mechanical load or by a chemical load. They showed that the estimated parameter values were in the same range as reported by other studies in literature for a uniaxially confined swelling and compression experiment [171, 186].

Further studies performed triphasic analysis of the articular cartilage explicitly incorporating the fixed charge density and ions, both diffusion and streaming potential, under unconfined compression [187, 188]. This analysis provided new information regarding the mechano-electrochemical signal transduction behavior of the tissue [187, 188]. Li and Herzog [189] developed a finite-element formulation of streaming potentials in articular cartilage and incorporated it into a fibril-reinforced model, and subsequently used it to simulate interactions between an arthroscopic probe and articular cartilage in a knee joint.

Wan *et al.* [190] briefly discussed some *in silico* electrical properties of the cartilage tissue in an unconfined compression experiment. Sachs and Grodzinsky [191] have also discussed the linear electrical properties in the nondestructive assessment of cartilage degeneration for the electromechanical spectroscopy of cartilage using a surface probe with applied mechanical displacement.

4.3.3 Other Stimuli

In literature, there are also few *in silico* studies available where electrical properties of the cartilage tissue have been investigated due to other stimuli, including permeation, osmosis, and convection. These studies were performed by Gu *et al.* [170, 173, 192, 193] and by Quenneville and Buschmann [194].

In their first study, Gu *et al.* [170] derived the expressions for streaming current and potential within the cartilage tissue under one-dimensional steady permeation condition, as a function of the intrinsic triphasic material coefficients. After this, they performed a study in which the relationships describing the dependence of the streaming potential on the negative fixed charge density of the tissue were derived analytically using the triphasic theory and its dependency was proven when compared to the experimental data on streaming potential obtained from bovine femoral cartilage [173]. Later, in another study, Gu *et al.* [192] analyzed the negative osmotic flows through charged hydrated cartilage tissue caused by an applied osmotic pressure gradient using the triphasic mixture theory, and they discussed the quantitative results of ion fluxes and electric potential across the tissue during diffusion process.

In their fourth study, Gu *et al.* [193] analyzed a one-dimensional dynamic permeation of a monovalent electrolyte solution through a negatively charged hydrated cartilaginous tissue using the triphasic mechano-electrochemical theory developed by Lai *et al.* [158] as the constitutive model for the tissue. The spatial distributions of stress parameters, ion concentrations, electrical potential, and ion fluxes within and across the tissue were analyzed [193].

Finally, Quenneville and Buschmann [194] developed a model of electrolyte transport across a charged membrane and examined the distribution of electric potential and mobile ion concentrations in response to forced convection.

All the stimulation techniques for the *in silico* investigation of electrical properties of the cartilage described are summarized in the Tables 4.1 - 4.3 for the electrical, mechanical, and other stimulations, respectively, along with the respective mathematical equations which have been noted in this chapter to describe these properties.

Table 4.1: Electrical stimulation studies.

Study	*Theory*	*Diffusion potential*	*Kinematics*	*Configuration type*	*Equations*
Frank and Grodzinsky [19]	Biphasic	X	Electrokinetics	Confined compression	(4.21)
Sachs and Grodzinsky [178]	Biphasic	X	Electrokinetics	Unconfined compression	(4.22)
Kojic *et al.* [177]	Biphasic	X	Electrokinetics	Confined/ unconfined compression	(4.21)
Kojic *et al.* [176]	Biphasic	X	Electrokinetics	Confined compression	(4.21)
Ateshian *et al.* [179]	Multiphasic	✓	Electrokinetics	Confined compression	(4.35)
Gu *et al.* [174]	Triphasic	X	Electrokinetics	Electro-osmosis	(4.21)
Gu *et al.* [163]	Multiphasic	✓	Continuity equation	Electro-osmosis	(4.35) & (4.36)
Levenston *et al.* [175]	poroelastic	X	Electrokinetics	Cconfined/ unconfined compression	(4.21)

Table 4.2: Mechanical stimulation studies.

Study	*Theory*	*Diffusion potential*	*Kinematics*	*Configuration type*	*Equations*
Lee *et al.* [181]	Biphasic	X	Electrokinetics	Confined compression	(4.21)
Kim *et al.* [182]	Biphasic	X	Electrokinetics	Unconfined compression	(4.23)
Chen *et al.* [183]	Biphasic	X	Electrokinetics	Confined compression	(4.21)
Chen *et al.* [184]	Biphasic	X	Electrokinetics	Confined compression	(4.21)
Lai *et al.* [162]	Triphasic	✓	Electrokinetics	Permeation/ confined compression	(4.35) & (4.36)
Lai *et al.* [185]	Triphasic	✓	Continuity equation	Confined compression	(4.36)
Frijns *et al.* [186]	quadphasic	✓	Electrokinetics	Confined compression	(4.33) & (4.34)
Frijns *et al.* [171]	quadphasic	✓	Electrokinetics	Confined compression	(4.33) & (4.34)
Mow *et al.* [187]	Triphasic (modified)	✓	Continuity equation	Unconfined compression	(4.55)
Sun *et al.* [188]	Triphasic (modified)	✓	Continuity equation	Unconfined compression	(4.56)
Li and Herzog [189]	Biphasic	X	Electrokinetics	Indentation	(4.21)
Sachs and Grodzinsky [191]	Biphasic	X	Electrokinetics	Spectroscopy	(4.21)
Wan *et al.* [190]	Triphasic	✓	Electrokinetics	Unconfined compression	(4.21)

Table 4.3: Other stimulation studies.

Study	*Theory*	*Diffusion potential*	*Kinematics*	*Configuration type*	*Equations*
Gu *et al.* [170]	Triphasic	✗	Electrokinetics	Permeation	(4.31)
Gu *et al.* [173]	Triphasic	✗	Continuity equation	Permeation	(4.31)
Gu *et al.* [192]	Triphasic	✓	Electrokinetics	Negative osmosis	(4.21)
Gu *et al.* [193]	Triphasic (modified)	✓	Continuity equation	Permeation	(4.56)
Quenneville and Buschmann [194]	Nernst-Planck/ Poisson equation	✓	Continuity equation	Convection	(4.21)

5 One-dimensional Electrokinetic Transduction Model Based on Continuum Theory

5.1 Overview

In this chapter, a numerical study involving electromechanical transduction in bovine cartilage tissue has been carried out using the open-source finite element computational software FEniCS. The simulation results have been compared to experimental results from the literature. This study serves as a basis for further *in silico* studies to better understand the behavior of hyaline cartilage tissue due to electrical stimulation and to find an optimal stimulation protocol for the cartilage regeneration.

5.2 Model Formulation

The electrokinetic model consists of electrical-to-mechanical and mechanical-to-electrical transductions. The transduction model was introduced in Chapter 4, schematically illustrated in Figures 5.1(a) and (b), respectively. The one-dimensional electrokinetic transduction in a charged, homogeneous, isotropic, hydrated bovine cartilage sample was analyzed and compared by the analytical and finite-element solutions using FEniCS with the experimental data from the studies reported by Frank and Grodzinsky [19, 126]. The data points were extracted from the references using the software WebPlotDigitizer [195].

The laws for linear electrokinetic transduction [167] in ionized media are combined with linear biphasic theory for cartilage [21]. A constitutive law for the total stress σ_{ij} in a homogeneous, isotropic tissue valid for small strains ε_{ij} is

$$\sigma_{ij} = 2G(c)\varepsilon_{ij} + (\lambda(c)\varepsilon_{kk} - P)\delta_{ij}, \tag{5.1}$$

where the Lamé constants μ_s and λ_s are functions of the ionic content (c) of the cartilage, P is the fluid pressure, ε is the strain, and the subscripts i, j, and k represent the axes.

The laws for linear electrokinetic transduction in isotropic media [167] are used to relate the relative fluid velocity $\mathbf{U}$ and the current density $\mathbf{J}$ in the tissue to the gradients in fluid pressure P, and electrical potential ψ already described by Equation (4.21), which is,

$$\begin{aligned}\mathbf{U} &= -k_{11}\nabla P + k_{12}\nabla\psi \\ \mathbf{J} &= k_{21}\nabla P - k_{22}\nabla\psi\end{aligned} \tag{5.2}$$

where k_{11} is the "short-circuit" hydraulic permeability, k_{12} and k_{21} are the electrokinetic coupling coefficients that are equal ($k_{12} = k_{21}$) by the Onsager reciprocity theorem [165, 166], and k_{22} is the electrical conductivity.

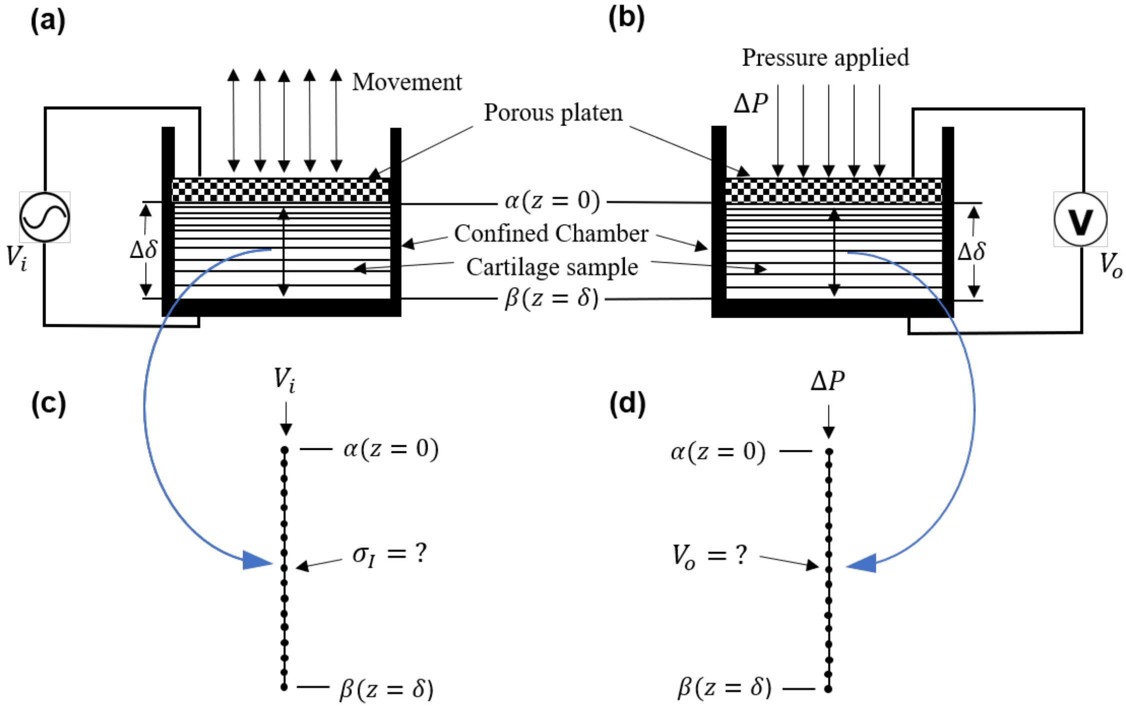

Figure 5.1: Schematic representation and discretization for electrokinetic transduction model. **(a)** Electrical-to-mechanical transduction, **(b)** mechanical-to-electrical transduction, **(c)** discretization to find current-generated stress, **(d)** discretization to find the streaming potential due to applied stress. ΔP is the change in pressure, $\Delta\delta$ is the change in thickness of the cartilage sample, V_i and V_o are the input and output voltages, respectively.

For the case of incompressible fluid and solid constituents, continuity relates the fluid and solid velocities $\mathbf{v}^w$ and $\mathbf{v}^s$ [196],

$$\phi^w\nabla\cdot\mathbf{v}^w + (1-\phi^w)\nabla\cdot\mathbf{v}^s = 0. \tag{5.3}$$

Since the confined uniaxial configuration is considered, only deformations in the z direction have been taken as described in Figure 5.1. After some mathematical steps, the equation of motion in the complex frequency domain reads as follows:

$$j\omega u = H_A k_d \frac{\partial u^2}{\partial z^2} + k_i J + U_o, \tag{5.4}$$

where ω is the angular frequency, $H_A = 2G + \lambda$ is the equilibrium confined compression modulus [197], k_i is the electrokinetic constant, J is the magnitude of the current density, and U_o is the constant of integration.

A general solution to the complex equation of motion (5.4) is given by

$$u(z) = \frac{(u^\alpha - u_J)\sinh\gamma(\delta - z) + (u^\beta - u_J)\sinh\gamma z}{\sinh\gamma\delta}, \tag{5.5}$$

where

$$u^\alpha = u(z = 0) \text{ and } u^\beta = u(z = \delta), \tag{5.6}$$

are the displacement amplitudes imposed at the top (α) and bottom (β) surfaces of the tissue as schematically illustrated in Figure 4.2, $\gamma^2 = j\omega/H_A k_d$, $u_J = (k_i J + U_o)/j\omega$.

Following the approach of Frank and Grodzinsky [19], first, the sinusoidal streaming potential and dynamic stiffness of a cartilage sample in response to sinusoidal displacement was considered under open-circuit condition ($\mathbf{J} = 0$). Then the stress generated by a sinusoidal current density applied to the electrodes was considered with the jaw-to-jaw displacement held fixed ($u = 0$).

Equation (5.5) is solved analytically to obtain the expression for dynamic stiffness (Λ), streaming potential (V_o), and current-generated stress (σ_I)

$$\Lambda = \frac{\Lambda_s \Lambda_{OC}}{\Lambda_s + \Lambda_{OC}} \tag{5.7a}$$

$$V_o = -k_e \left[\frac{\Lambda_s \Lambda_V}{\Lambda_s + \Lambda_{OC}}\right] \frac{u}{\delta} \tag{5.7b}$$

$$\sigma_I = -\frac{k_i J}{j\omega\delta} \left[\frac{\Lambda_s \Lambda_V}{\Lambda_s + \Lambda_{OC}}\right], \tag{5.7c}$$

where $\Lambda_{OC} = H_A\delta\coth\gamma\delta$, $\Lambda_V = H_A\delta\tanh(\gamma\delta/2)$, and Λ_s is the stiffness of the porous platen (see Figure 5.1). The analytical solutions for the amplitudes of dynamic stiffness, streaming potential, and current-generated stress for the frequency range of 0.005–1 Hz (relevant to impact loading) are shown in Figures 5.2–5.4, respectively.

5.3 Galerkin Form of the Finite Element Formulation

For the mechanical-to-electrical transduction, the applied current density is zero i.e., $J = 0$ and the Galerkin form of Equation (5.4) is,

$$j\omega \int_{\Omega} uv dz = H_A k_d \int_{\Omega} \frac{\partial u^2}{\partial z^2} v dz, \tag{5.8}$$

Using integration by parts, Equation (5.8) can be written as,

$$H_A k_d \int_{\Omega} \frac{\partial u}{\partial z}\frac{\partial v}{\partial z} dz + j\omega \int_{\Omega} uv dz = 0. \tag{5.9}$$

Solving Equation (5.9) numerically for the unknown u and using Equation (5.7b), the generated potential across the specimen is obtained as plotted in Figure 5.3.

For the electrical-to-mechanical transduction, the Galerkin form of Equation (5.4) is,

$$j\omega \int_{\Omega} uv dz = H_A k_d \int_{\Omega} \frac{\partial u^2}{\partial z^2} v dz + k_i \int_{\Omega} Jv dz. \tag{5.10}$$

Applying integration by parts, Equation (5.10) can be written as,

$$j\omega \int_{\Omega} uv dz + H_A k_d \int_{\Omega} \frac{\partial u}{\partial z}\frac{\partial v}{\partial z} dz = k_i \int_{\Omega} Jv dz. \tag{5.11}$$

The relation to find the current-generated stress is,

$$\sigma_I = -H_A \frac{\partial u}{\partial z}. \tag{5.12}$$

Solving Equation (5.11) numerically for the unknown u and using Equation (5.12), the current-generated stress for the specimen is obtained as plotted in Figure 5.4.

5.4 Results and Discussion

The numerical solution of the partial differential Equation (5.4) is performed using the open-source tool FEniCS together with a Python interface. The simulation was performed using the ‘LinearVariationalSolver’ of FEniCS [118] with Lagrange elements [116, 198] of order 1. The computation time was 0.65 seconds with 20,002 degrees of freedom on a computer with 32GB RAM, Intel(R) Xeon(R) CPU E5-1630 v3 @ 3.00 GHz. The finite-element simulation results for the amplitudes of dynamic stiffness, streaming potential, and current-generated stress for the frequency range of

0.005–1 Hz (relevant to impact loading) are shown in Figures 5.2–5.4, respectively. In the same figures, the finite-element simulation results are compared to the analytical results and experimental data extracted from the experimental results of Frank and Grodzinsky [19].

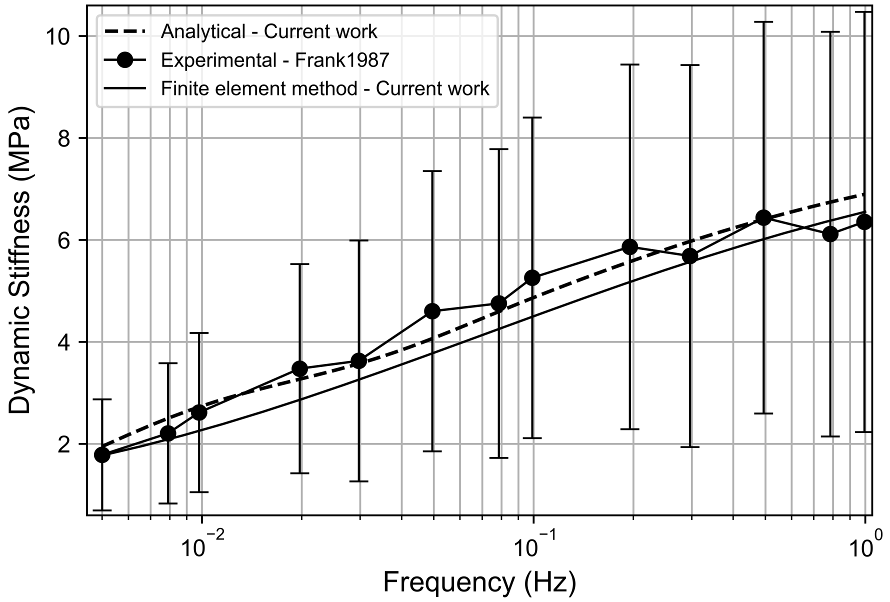

Figure 5.2: Mechanical-to-electrical transduction–amplitude of the dynamic stiffness versus frequency.

Table 5.1 lists all the parameters used for the simulations. The fit of theoretical values to the analytical and experimental values does not employ any adjustable parameter in contrast to the studies reported by Frank and Grodzinsky [19] and Kojic *et al.* [176]. The frequency-dependent viscoelastic behavior of cartilage tissue is evident from these graphs [156]. This open-source numerical implementation allows relatively easy implementation without any complex coding techniques. The Python scripts used in this study are available in an online repository (`https://github.com/arfarooqi/Cartilage_electromechanics`).

The numerical simulation results compare well to the analytical and experimental results [19, 126] in general. There is a small difference between the analytical and finite element solution which is due to the fact that the finite element formulation considered here is geometrically linear. This variation can be removed if the change of porosity and geometrical non-linearity is taken as well in the finite element formulation [176]. Some small variations could also be due to the fact that the actual experimental setup is in three dimensions, but the analysis only considers

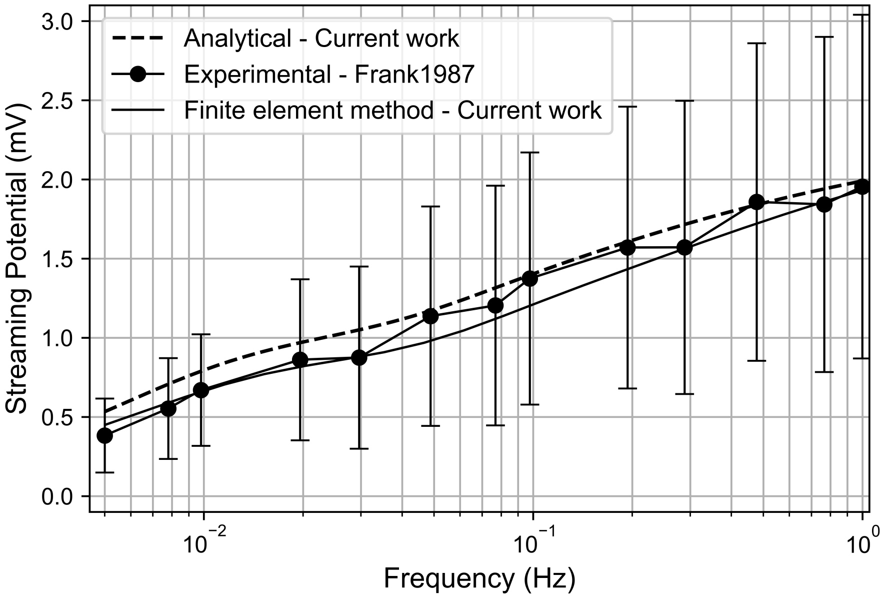

Figure 5.3: Mechanical-to-electrical transduction–amplitude of streaming potential versus frequency.

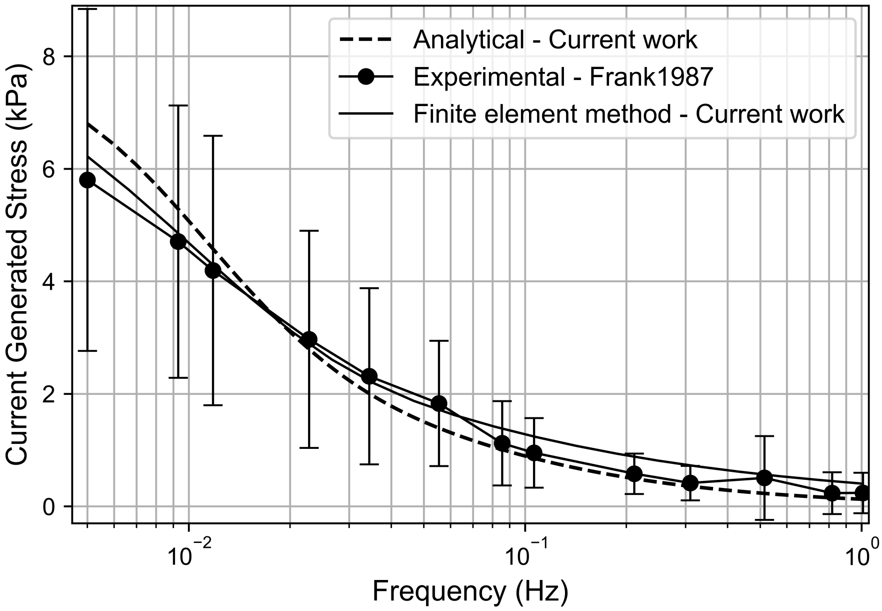

Figure 5.4: Electrical-to-mechanical transduction–amplitude of current-generated stress versus frequency.

the amplitudes in one dimension. In addition, the analysis only regarded z-directed amplitudes, while neglecting those in x and y directions, while in reality, there can be small contributions to the amplitudes from the other two directions as well.

Table 5.1: Principal set of parameters.

Compressive modulus, H_A	1 MPa
Platen stiffness, Λ_s	8.3 MPa
Applied displacement, u	10×10^{-6} m
Thickness of sample, δ	680×10^{-6} m
Diameter of sample, D	6.35×10^{-6} m
Applied current density, J	3.80 A/m^2
Hydraulic permeability, k_d	3×10^{-15} m^2/Pa·s
Electrokinetic constant, k_i	-2.07×10^{-8} V/Pa
Electrokinetic constant, k_e	-2.18×10^{-8} V/Pa

5.5 Convergence Study

To determine the convergence of the finite-element analysis for mechanical-to-electrical transduction, the relative error in the streaming potential at a representative frequency of 0.3 Hz was examined, while refining the mesh. The relative error is found using the relation

$$\text{relative error} := \frac{|u_i - u_{i-1}|}{|u_i|} \tag{5.13}$$

where u_i and u_{i-1} are the current and previous values, respectively. Figure 5.5 depicts the results of this convergence study using Equation (5.13). Obviously, the relative error in the amplitude of the streaming potential approaches zero if the mesh incorporates more than 460 elements, corresponding to more than 922 degrees of freedom. The relative error for the mechanical-to-electrical transduction descends with the order 4.5.

Similarly, the convergence of the finite-element analysis for the electrical-to-mechanical transduction for the current-generated stress was analyzed at a representative frequency of 0.7 Hz using Equation (5.13). Figure 5.6 makes evident that the relative error in the amplitude of the current-generated stress approaches zero if the mesh incorporates more than 850 elements, corresponding to more than 1702 degrees of freedom. The relative error for the electrical-to-mechanical transduction descends with the order 4.3. Thereby, good mesh convergence is achieved with almost

460 and 850 elements for the mechanical-to-electrical and electrical-to-mechanical transductions, respectively.

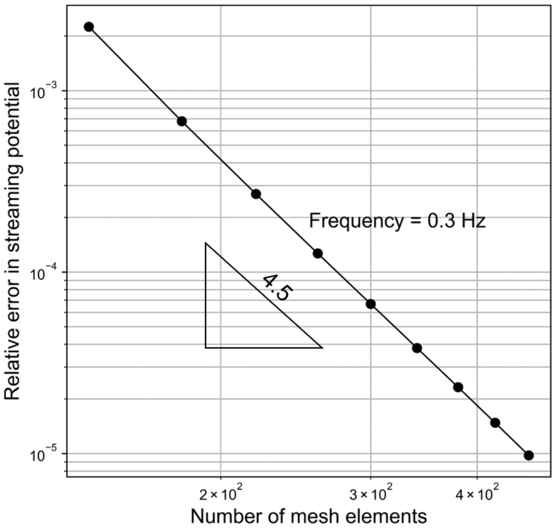

Figure 5.5: Relative error in amplitude of streaming potential as a function of mesh elements taken at a representative value of $f = 0.3\,\text{Hz}$ using the Equation (5.13).

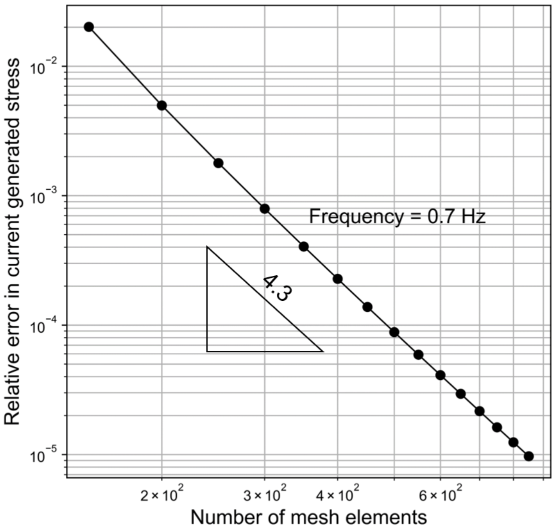

Figure 5.6: Relative error in amplitude of current-generated stress as a function of mesh elements taken at a representative value of $f = 0.7\,\text{Hz}$ using the Equation (5.13).

6 Electroactive Scaffolds for Cartilage–Tissue Repair

6.1 Overview

The intrinsic regeneration potential of hyaline cartilage is highly limited due to the absence of blood vessels, lymphatics, and nerves, as well as a low cell turnover within the tissue. Despite various advancements in the field of regenerative medicine, it remains a challenge to remedy articular cartilage defects resulting from trauma, aging, or osteoarthritis. Among various approaches, tissue engineering using tailored electroactive scaffolds has evolved as a promising strategy to repair damaged cartilage tissue. In this approach, hydrogel scaffolds are used as artificial extracellular matrices, and electric stimulation is applied to facilitate proliferation, differentiation, and cell growth at the defect site. In this regard, a simulation model of electroactive hydrogels to be used for cartilage–tissue engineering is presented employing the open-source finite-element software FEniCS together with a Python interface. The proposed mathematical formulation was first validated with an example from the literature. Then, the effect of electric stimulation on a circular hydrogel sample is computed that serves as a model for a cartilage-repair implant.

6.2 Introduction

In general, developing a computational or mathematical model presents a critical prerequisite to design informative and comprehensible experiments [31]. These models can be used to replicate the physical experiments and can be manipulated in ways that would otherwise be too costly and complex. The modeling approach enables to simulate surgical conditions without damaging the biological specimen. Hence, experiments can be easily optimized with respect to electrical input parameters. Various cartilage–tissue engineering approaches were experimentally performed but appropriate computational models are still lacking [74, 199, 200]. Keeping this in mind, an open-source simulation workflow is proposed to develop better experimental procedures for cartilage–tissue engineering using electrical stimulation.

It is known that application of electrical stimulation results in ion motion and the opening of voltage-gated calcium channels [201]. The increased activity of intracellular-calcium concentration activates the underlying mechanisms that facilitate cell growth, proliferation, and differentiation in a tissue-engineered sample. The complete tissue-engineering approach is schematically described in Figure 6.1. In the current study, the *in vitro* electrical stimulation part of the tissue-engineering approach is considered here, as illustrated in Figure 6.2. By means of numerical simulations, these mechanisms can be studied at different length scales.

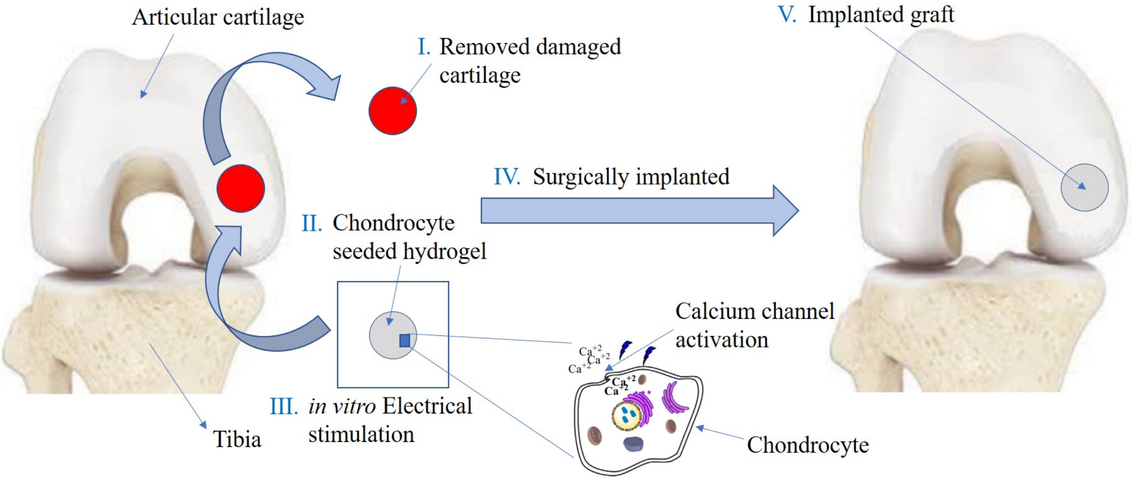
Articular cartilage
I. Removed damaged cartilage
V. Implanted graft
IV. Surgically implanted
II. Chondrocyte seeded hydrogel
Calcium channel activation
Ca+2
III. in vitro Electrical stimulation
Tibia
Chondrocyte

Figure 6.1: Various steps involved in tissue engineering of knee articular cartilage using electrical stimulation by replacing the defect site with a chondrocyte-seeded hydrogel (adapted with permission from [7]).

The sample consisting of a hydrogel embedded with chondrocytes was immersed in NaCl solution subject to an externally applied electrical stimulation as shown in Figure 6.2. The corresponding finite-element discretization of the geometry is given in Figure 6.3. The implementation of the simulation model consisted of solving nonlinear coupled Poisson–Nernst–Planck partial differential equations numerically using FEniCS to find the distribution of the electric potential, and the concentration of anions and cations with the given set of boundary conditions. The distinction between hydrogel and solution phases was realized by using different material parameters for each domain. The most important feature of the hydrogel phase in this model was the presence of bound anionic charges c^f with z^f valence. The complete mathematical description, the Galerkin formulation, and the parameters for the Poisson–Nernst–Planck equations are given in the next sections.

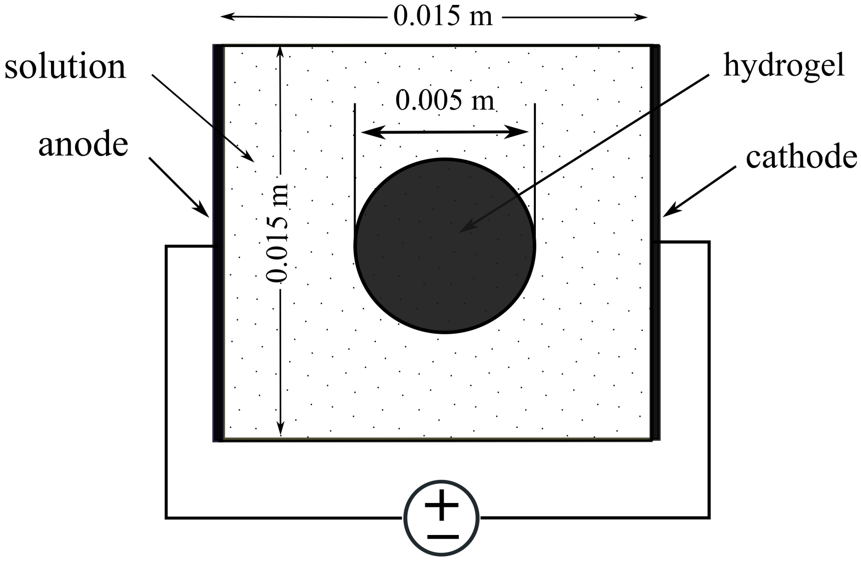
0.015 m
solution
anode
0.005 m
hydrogel
cathode
0.015 m
±

Figure 6.2: Hydrogel sample immersed in NaCl bath solution under externally applied electric field.

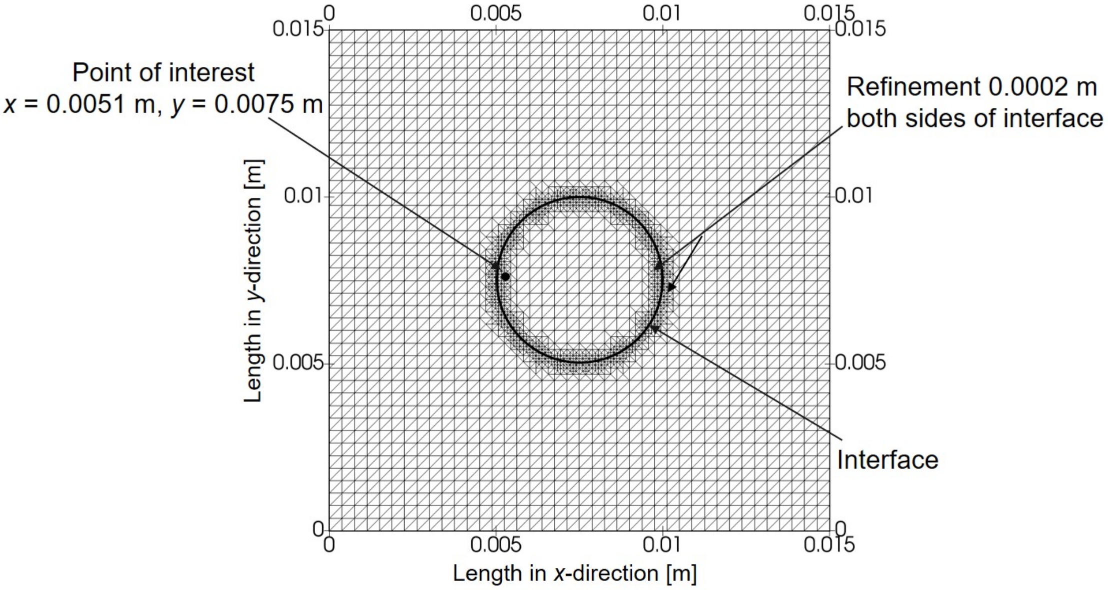
Point of interest
x = 0.0051 m, *y* = 0.0075 m
Refinement 0.0002 m
both sides of interface
Interface
Length in *y*-direction [m]
Length in *x*-direction [m]
0
0.005
0.01
0.015

Figure 6.3: Local mesh refinement used at the interface of the hydrogel sample and the NaCl bath solution.

6.3 Mathematical Model

Several mathematical formulations were proposed to simulate the electrochemical behavior of electroactive hydrogels immersed in a solution bath. Based on Flory's theory [202] and the Donnan equilibrium [203], Shiga *et al.* [204], and Doi *et al.* [205] developed models to investigate the hydrogel behavior under an applied electric field. Grimshaw *et al.* [206] presented a macroscopic continuum theory to explain the dynamic response of hydrogels to electric stimulation. However, these models were not able to precisely simulate the behavior of electroactive hydrogels.

A significant amount of the literature to simulate the electroactive behavior of hydrogels originates from the studies of hydrogel-like biological tissue like articular cartilage. It includes the triphasic theory of Lai *et al.* [158] and the multiphasic theory of Gu *et al.* [160], which are based on the classical biphasic theory of Mow *et al.* [21]. However, these theories are not suitable in simulating electrochemical phenomena in hydrogels, such as ion diffusion and the effect of fixed-charge density on ionic-concentration distribution. Zhou *et al.* [207] extended the triphasic model to describe the behavior of electroactive hydrogels immersed in the solution, but the computational domain only covered the hydrogel, which limited its applicability.

Based on multiphasic mixture theory, Li *et al.* [208] proposed a comprehensive model to describe the coupling effects and the multiphasic interactions in the electroactive hydrogels. Similarly, the transport model of polyelectrolyte hydrogels was developed by Wallmersperger *et al.* [8, 209]. Both these models were similar as they consisted of nonlinear coupled Poisson–Nernst–Planck equations to describe diffusive ionic species and electric potential, but differed in coupling the electrochemical response to the mechanical equilibrium equation. As only the electrochemical behavior is considered here, either of these two models could be used for result comparison.

In the current study, the model proposed by Wallmersperger *et al.* [8] was adapted to carry out finite-element simulations. The geometry of the problem is shown in Figure 6.2, where a square hydrogel sample was first considered for validation instead of the circular hydrogel sample. The model comprised two coupled nonlinear differential equations, i.e., Poisson and Nernst–Planck equations, described below. The Poisson–Nernst–Planck equations present several difficulties when computing approximate solutions. It is a strongly coupled system of $n + 1$ nonlinear equations, so computational efficiency plays a critical role in the implementation of the numerical solution, where n is the number of mobile ion species.

To date, the Poisson–Nernst–Planck model for hydrogels has been simulated using custom programs implemented in individual workgroups [208] that are not generally publicly available. Few of them have also been implemented using commercial software [210]. These models have mostly been implemented for one-dimensional cases, and a small number of them for two-dimensional cases. None of the models has been implemented so far using any open-source software and for the electrical-stimulation response of the hydrogels in context of cartilage–tissue engineering. Therefore, simulations of electroactive hydrogels for cartilage–tissue engineering have been performed using the open-source numerical software FEniCS [118].

As the geometry considered here is relatively simple, the geometry creation, meshing, and solving the variational problem could all be done using FEniCS, and then visualizing the results using Paraview [211]. For physiologically more complicated geometries, a more comprehensive open-source simulation workflow was implemented as well, which consisted of SALOME (www.salome-platform.org) for geometry creation, Gmsh [212] for meshing, the solution of the variational problem using FEniCS, and then result visualization using Paraview. The complete open-source workflow is shown in Figure 6.4. The results presented here are the same by using either of the two simulation workflows discussed here. The models and the Python scripts used in this study are available in an online repository (`https://github.com/arfarooqi/Electro-active-hydrogels`).

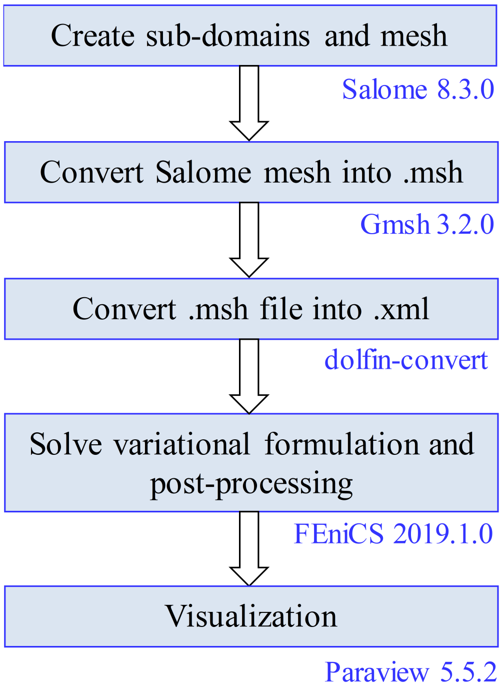
Create sub-domains and mesh
Salome 8.3.0
Convert Salome mesh into .msh
Gmsh 3.2.0
Convert .msh file into .xml
dolfin-convert
Solve variational formulation and post-processing
FEniCS 2019.1.0
Visualization
Paraview 5.5.2

Figure 6.4: Proposed open-source simulation workflow.

6.3.1 Poisson Equation

The Poisson equation for the electric potential is derived from Gauss' law, which states that

$$\nabla \cdot \mathbf{D} = \rho \tag{6.1}$$

where $\mathbf{D}$ and ρ are the electric flux density and the charge density, respectively, which are defined as

$$\mathbf{D} = \varepsilon_r \varepsilon_o \mathbf{E} = -\varepsilon_r \varepsilon_o \nabla \psi \tag{6.2}$$

$$\nabla \cdot (-\varepsilon_r \varepsilon_o \nabla \psi) = \rho \tag{6.3}$$

where ε_r is the relative permittivity of the surrounding medium, ε_o is the vacuum permittivity or dielectric constant, and ψ is the electric potential. As the electric field may be assumed to be curl-free, i.e., according to Faraday's law the time derivative of the magnetic flux density is negligibly small, a scalar potential can be used as a solution approach [115]. The charge density ρ was related to the mobile and fixed ion concentrations as

$$\rho = F_c \left(\sum_{k=1}^{n} z^k c^k + z^f c^f \right) \tag{6.4}$$

where F_c is Faraday's constant, c^k represent the ionic concentrations with valence $z^k (k = 1, 2, ..., n)$, and c^f is the concentration of fixed ionic species with valence z^f. From Equations (6.1) and (6.2), Poisson's equation is obtained as

$$\nabla^2 \psi + \frac{F_c}{\varepsilon_r \varepsilon_o} \left(\sum_{k=1}^{n} z^k c^k + z^f c^f \right) = 0. \tag{6.5}$$

Applying homogeneous Neumann boundary conditions at the top and bottom surface of the solution bath, the Galerkin formulation of Poisson's equation is [122]

$$\int_\Omega \nabla \psi \cdot \nabla v_\psi dA = \frac{F_c}{\varepsilon_r \varepsilon_o} \int_\Omega \left(z^+ c^+ + z^- c^- + z^f c^f \right) v_\psi dA \tag{6.6}$$

where two ionic species were considered, i.e., cation ' + ' and anion ' − ', v_ψ is the test function, and dA denotes the two-dimensional differential element for integration over the domain Ω. Here, integration by parts is used and the test function is assumed to vanish on the boundary of the domain Ω.

6.3.2 Nernst–Planck Equation

The total flux $\mathbf{J}^k$ of ion k is composed of three components: diffusion flux $\mathbf{J}^k_{\text{diff}}$ caused by the chemical potential gradient of ions, electric transference $\mathbf{J}^k_{\text{elect}}$ caused by the electrical potential gradient, and transfer $\mathbf{J}^k_{\text{conv}}$ caused by the convection. They are written as [213],

$$\begin{aligned}
\mathbf{J}^k_{\text{diff}} &= -D^k c^k \nabla \vartheta^k, & (6.7)\\
\mathbf{J}^k_{\text{elect}} &= -z^k \vartheta^k c^k \nabla \psi, & (6.8)\\
\mathbf{J}^k_{\text{conv}} &= c^k \nu & (6.9)
\end{aligned}$$

where D^k is the diffusivity of the kth ionic species, ϑ^k is the ionic mobility, and ν is the area-averaged fluid velocity through the hydrogel, relative to the hydrogel's polymer network. If the effect of the activity coefficient is explicitly taken into account, the diffusion flux becomes

$$\mathbf{J}^k_{\text{diff}} = -D^k \left(\nabla c^k + c^k \nabla \ln f^k \right) \tag{6.10}$$

where f^k is the chemical-activity coefficient of the kth species. The total flux $\mathbf{J}^k$ can now be written as

$$\mathbf{J}^k = -\left(D^k \nabla c^k + D^k c^k \nabla \ln f^k + z^k \vartheta^k c^k \nabla \psi \right) + c^k \nu. \tag{6.11}$$

The continuity equation that governs the flux of ionic species throughout the hydrogel and the surrounding solution is given as

$$\frac{\partial c^k}{\partial t} + \nabla \cdot \mathbf{J}^k = 0. \tag{6.12}$$

The first term in Equation (6.12) represents the change of concentrations with time, while the second term is the combination of the following four contributive terms: the migrative term due to a gradient in the electric potential, the diffusive term resulting from concentration differences, the convective term due to an applied velocity of the solvent, and the source term due to chemical reactions inside the gel-solution domain or at the electrodes.

In Equation (6.11), it was then assumed that no chemical reactions occurred and convection was neglected. Then, continuity Equation (6.12) becomes [214–216]

$$\frac{\partial c^k}{\partial t} = \nabla \cdot \left(D^k \nabla c^k + z^k \vartheta^k c^k \nabla \psi \right). \tag{6.13}$$

Next, the mobility ϑ^k could be determined from the Nernst–Einstein relationship, which relates diffusivity to ionic mobility [217],

$$\vartheta^k = \frac{D^k F_c}{RT}. \tag{6.14}$$

where R is the universal gas constant, and T is the absolute temperature. So, Equation (6.13) becomes

$$\frac{\partial c^k}{\partial t} = \nabla\cdot \left(D^k \nabla c^k + \frac{z^k F}{RT} D^k c^k \nabla \psi \right). \tag{6.15}$$

Now, the Galerkin formulation of Equation (6.15) considering two ionic species is obtained by multiplying with a test function v_k and integrating over domain Ω,

$$\int_\Omega \frac{\partial c^k}{\partial t} v_k dA = D^k \int_\Omega \nabla c^k \cdot \nabla v_k dA + D^k \frac{z^k F}{RT} \int_\Omega c^k \nabla \psi \cdot \nabla v_k dA, \quad (k = +, -). \tag{6.16}$$

The time derivative can be approximated by using the backward (or implicit) Euler difference method [218]

$$\frac{\partial c^k}{\partial t} \approx \frac{c^k_{i+1} - c^k_i}{\Delta t} \tag{6.17}$$

where Δt is the time-step parameter, and c^k_{i+1} and c^k_i represent the concentration of ions for the new and the previous time step, respectively. Using the above notation, Equation (6.16) was rewritten as

$$\int_\Omega c^k_{i+1} v_k dx - \int_\Omega c^k_i v_k dx = \Delta t D^k \int_\Omega \nabla c^k \cdot \nabla v_k dx + \Delta t D^k \frac{z^k F}{RT} \int_\Omega c^k \nabla \psi \cdot \nabla v_k dx, \quad (k = +, -). \tag{6.18}$$

where dx denotes the one-dimensional differential element for integration over the domain Ω. For the numerical solution of the Poisson–Nernst–Planck equations, a mixed-function space [219] consisting of three scalar functions, i.e., anion, cation, and electric potential was used with Lagrange elements [116, 198] of order 2. Mixed finite element methods use two or more finite element spaces to approximate the separate variables. A mixed function space can be created by the arbitrary combinations of function spaces to represent the full system as a single entity. The benefit of such methods becomes evident when equations involve several variables and elimination of any of the variables is not possible.

The given nonlinear problem was solved using the ‘NonLinearVariationalSolver’ of FEniCS [118] based on Newton’s method with the associated solver ‘MUMPS’ (MUltifrontal Massively Parallel sparse direct Solver) [220]. MUMPS is a direct solver used for the solution of linear system occurring within Newton’s iterations [118].

6.4 Results and Discussion

6.4.1 Chemical Stimulation

In the simulation model, it is assumed that initially, the hydrogel was taken out of a solution bath with concentration of $2\,\mathrm{mM} = 2\,\mathrm{mmol/l} = 2\,\mathrm{mol/m^3}$ and put into another with concentration of $1\,\mathrm{mM}$. Thus, the concentration of bound anionic groups in the hydrogel was $2\,\mathrm{mM}$ at time $t = 0$ and the boundary conditions for the ions at the solution boundary were set to $1\,\mathrm{mM}$. Biological tissue like cartilage and hydrogels exhibit the phenomenon of swelling. It is caused by electric charges fixed to the porous solid. They attract free ions of the opposite charge, present in the fluid. Fluid flow took place between the hydrogels and the salt solution until equilibrium was reached. The Donnan equilibrium concentration of ions in the hydrogel was calculated using [159, 221]

$$\begin{aligned} c^{+}_{\mathrm{gel}} &= \frac{1}{2}\left(-c^{f} + \sqrt{[c^{f}]^{2} + 4[c^{+}_{\mathrm{sol}}]^{2}}\right) \\ c^{-}_{\mathrm{gel}} &= \frac{1}{2}\left(c^{f} + \sqrt{[c^{f}]^{2} + 4[c^{-}_{\mathrm{sol}}]^{2}}\right). \end{aligned} \tag{6.19}$$

The corresponding Donnan potential created due to the concentration difference inside and outside the hydrogel could be found either in terms of cation or anion concentrations [222–224],

$$\Delta\phi = \frac{RT}{z^{+}F_c}\ln\left(\frac{c^{+}_{\mathrm{gel}}}{c^{+}_{\mathrm{sol}}}\right) \quad \text{or} \quad \Delta\phi = \frac{RT}{z^{-}F_c}\ln\left(\frac{c^{-}_{\mathrm{gel}}}{c^{-}_{\mathrm{sol}}}\right). \tag{6.20}$$

Using Equation (6.19), the concentration of anions and cations in the hydrogel due to chemical stimulation are 0.4142 and $2.4142\,\mathrm{mM}$, respectively. Similarly, from Equation (6.20), the value of the Donnan potential was $-22.252\,\mathrm{mV}$. The numerical solution for the chemical stimulation was performed at initial time $t = 0$ using Equations (6.6) and (6.18) considering two ionic species with the concentration of $1\,\mathrm{mM}$ for both species at the solution boundaries. For the chemical stimulation, an externally applied electric field was set to zero at the solution boundaries. The parameters used for the numerical simulation are listed in Table 6.1, and one-dimensional results of the chemical stimulation are shown in Figures 6.5–6.7, which were the same as by using Donnan theory. These results were also in agreement with the numerical results of Wallmersperger *et al.* [8].

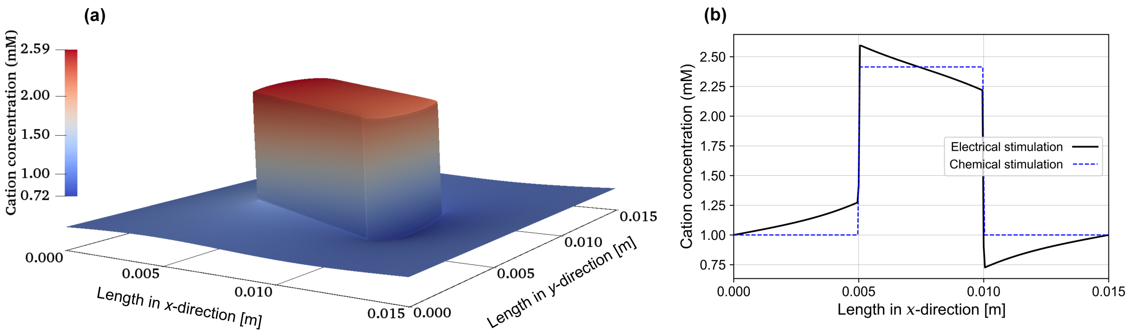

Figure 6.5: Cation concentration: **(a)** two-dimensional electrical stimulation, **(b)** comparison of chemical and electrical stimulation versus x-position at $y = 0.0075\,\mathrm{m}$.

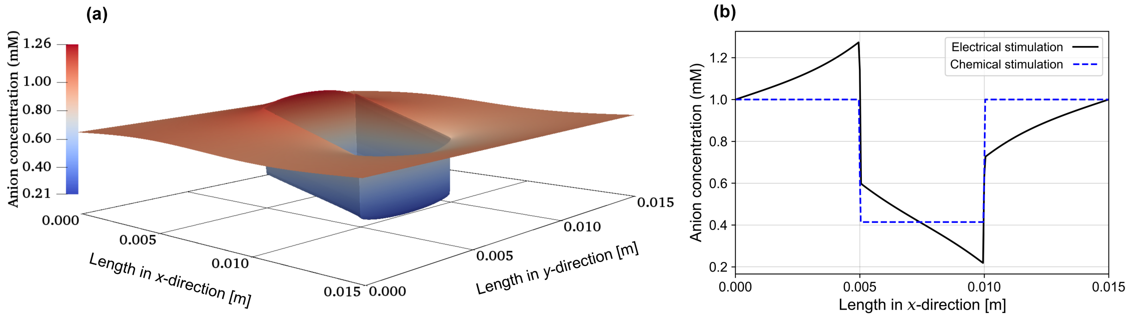

Figure 6.6: Anion concentration: **(a)** two-dimensional electrical stimulation, **(b)** comparison of chemical and electrical stimulation versus x-position at $y = 0.0075\,\mathrm{m}$.

6.4.2 Electrical Stimulation

For the electrical stimulation, Equations (6.6) and (6.18) were again solved numerically for two ionic species using FEniCS with the parameters listed in Table 6.1. The convective flux was assumed to be zero and no chemical conversion was considered in the equations. The values obtained due to the chemical stimulation were taken as initial conditions for the electrical-stimulation problem, and an external electric potential of 50 mV was applied at the solution boundaries. To achieve the rapid convergence of the solution, local mesh refinement was used, which extends 0.002 m on both sides of the hydrogel–solution interface.

As the electrical stimulation was applied to the bath solution in which the hydrogel was immersed, mobile ions were redistributed in both the hydrogel and the surrounding solution. Due to the fixed-charge groups bound to the cross-linked macromolecular chains of the hydrogel, the diffusion gave rise to ionic concentration differences between the interior hydrogel and the exterior bath solution. The graphs

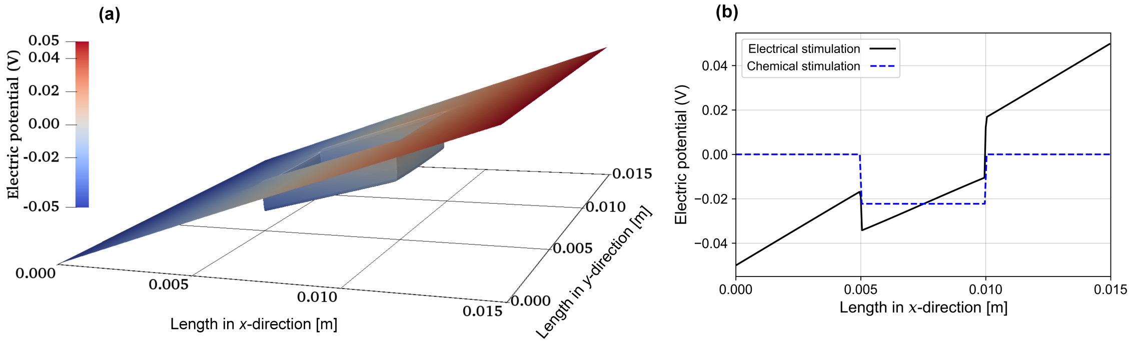

Figure 6.7: Electric potential: **(a)** two-dimensional electrical stimulation, **(b)** comparison of chemical and electrical stimulation versus x-position at $y = 0.0075\,\mathrm{m}$.

Table 6.1: Simulation parameters used in accordance with [8].

Parameter	**Value**
Cation valence z^+	1.0
Anion valence z^-	-1.0
Bound charge valence z^f	-1.0
Ion mobility ϑ^k	$3.9607 \times 10^{-6}\,\mathrm{m^2\,s^{-1}\,V^{-1}}$
Ion diffusion coefficient D^k	$1.0 \times 10^{-7}\,\mathrm{m^2\,s^{-1}}$
Faraday constant F_c	$9.6487\,\mathrm{C\,mol^{-1}}$
Temperature T	$293\,\mathrm{K}$
Gas constant R	$8.3143\,\mathrm{J\,mol^{-1}\,K^{-1}}$
Vacuum permittivity ε_o	$8.854 \times 10^{-12}\,\mathrm{A\,s\,V^{-1}\,m^{-1}}$
Relatively permittivity ε_r	100.0

for anion, cation, and electric potential distribution are shown in Figures 6.5–6.7, where 10,387,755 degrees of freedom were used. The one-dimensional graphs for the same quantities extracted from the two-dimensional plots at positions x and $y = 0.0075\,\mathrm{m}$ are also shown in the same figures. These results are in agreement to the numerical results of Wallmersperger *et al.* [8], and in qualitative agreement to the experiment results of Gülch *et al.* [225].

After validation, the finite-element model was modified for a two-dimensional circular specimen (approximation of a three-dimensional cylindrical sample) immersed in solution as used in cartilage–tissue engineering [226] and shown in Figure 6.1. Figures 6.8–6.10 show the graphs of the anion, cation, and electric potential distribution in the solution and in the hydrogel scaffold at initial time $t = 0$. Because of the presence of fixed-charge ions in the hydrogel, there was a sharp change in electric potential and in the concentrations of anions and cations to satisfy the electroneutrality condition. In comparison to the initial conditions, the concentrations of cations and anions were slightly higher in the hydrogel on the cathode side as compared to the anode side. Similarly, ion concentrations in the solution near the hydrogel–solution interface increased at the cathode side and decreased at the anode side. From these figures, it can be concluded that the ion concentrations and electric potential in the hydrogel sample could be optimized as the requirement by varying the different quantities. The computation time was ∼8 min with 9,257,499 degrees of freedom on a workstation with 256 GB RAM, Intel(R) Xeon(R) CPU E5-2687W v4 @ 3.00 GHz. The number of degrees of freedom was estimated by the convergence analysis as discussed in Section 6.4.3. This large number of the degrees of freedom is necessary as the coupled Poisson–Nernst–Planck equations are nonlinear, and the solution tends to become unstable at the hydrogel-solution interface by the occurrence of nonphysical negative ionic concentrations.

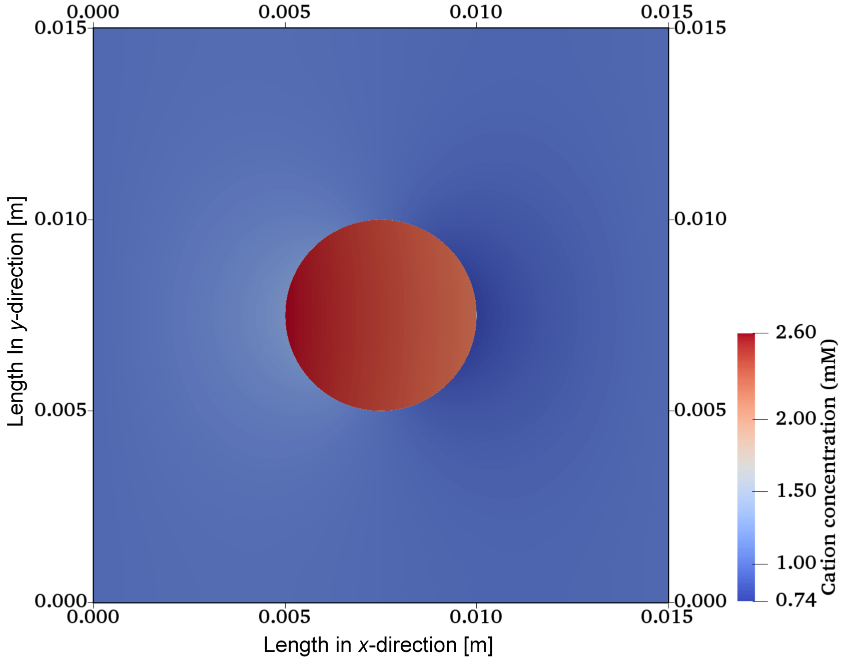

Figure 6.8: Cation-concentration profile at initial time $t = 0$ for a hydrogel scaffold immersed in solution.

Transient simulations for variations of the ionic concentration and electric potential are also presented in Figure 6.11. It was observed that, at initial time $t = 0$, the distributions of ionic concentrations are symmetric in the whole computational

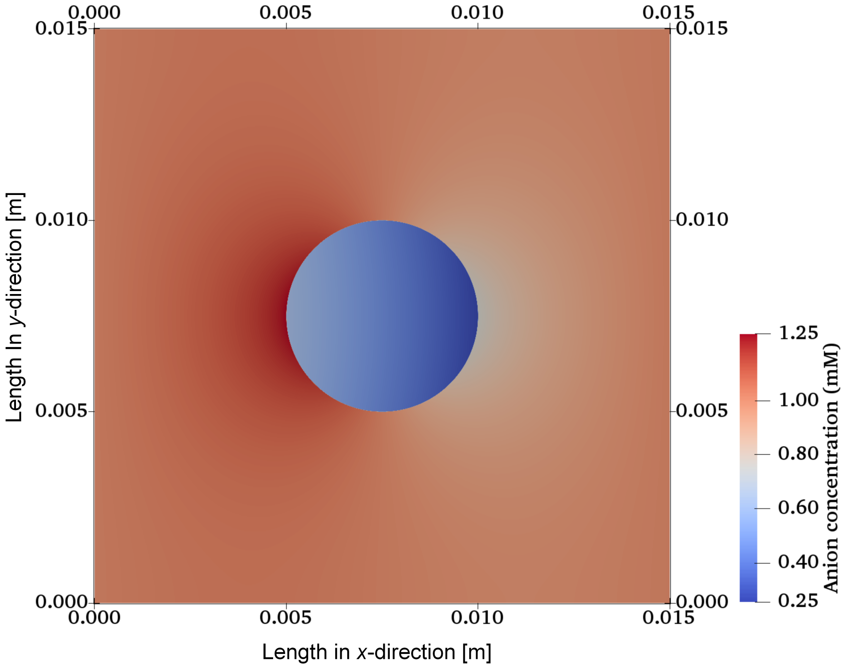

Figure 6.9: Anion concentration profile at initial time $t = 0$ for a hydrogel scaffold immersed in solution.

domain, same as from the chemical stimulation without external electric field. As time increased, the diffusive ions redistributed continuously in both the hydrogel and the 1 mM NaCl solution, and the ionic-concentration differences near the hydrogel–solution interfaces became increasingly larger. Ionic diffusion and convection reached the equilibrium state after a specific time, which was dependent on various parameters and conditions, including the electric field, fixed charge density, and NaCl solution concentration. Thus, the concentration of ions and the electric potential in the hydrogel sample could be optimized at various time intervals. For the current case, the steady-state solution for all variables was obtained at around 800 s, after which no further change in the ion concentrations and electric potential occurred. These results follow the same trend as observed by Wallmersperger *et al.* [8].

6.4.3 Convergence Study

To determine the convergence of the finite element analysis for the proposed simulation scheme, the relative error in the electric potential, and the concentration of anions and cations is examined at a representative point ($x = 0.0051\,\mathrm{m}$, $y = 0.0075\,\mathrm{m}$) just inside the hydrogel, while refining the mesh. A local mesh refinement

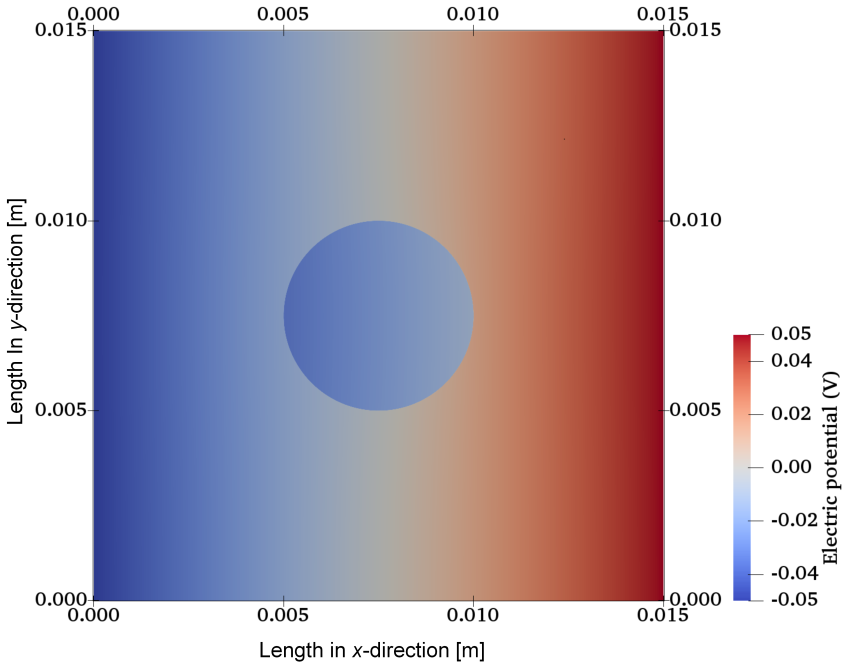

Figure 6.10: Electric potential distribution at initial time $t = 0$ for a hydrogel scaffold immersed in solution.

was used in a neighborhood of 0.0002 m on both sides of the interface as shown in Figure 6.3 because this is the region where the solution tends to become unstable and unphysical negative values observed. The convergence study was initiated from one refinement cycle in a distance of 0.0002 m on both sides of the interface, and ended at the sixth cycle while keeping the mesh in the remaining solution domain constant in each refinement cycle. The relative error is found using the relation

$$\text{relative error} := \frac{|u_i - u_{i-1}|}{|u_i|} \tag{6.21}$$

where u_i and u_{i-1} are the current and previous values of the degrees of freedom, respectively, corresponding to the each refinement cycle. The relative error in the concentrations of anions, cations, and electric potential distribution at the representative point ($x = 0.0051\,\text{m}$, $y = 0.0075\,\text{m}$) is plotted against the degrees of freedom as given in Figure 6.12. Expectedly the relative error reduces as the degrees of freedom increase. Obviously, the relative error in the values of anions, cations and electric potential approaches a stable value if the mesh incorporates more than 1 million degrees of freedom. The global convergence is checked as well by computing the L^2

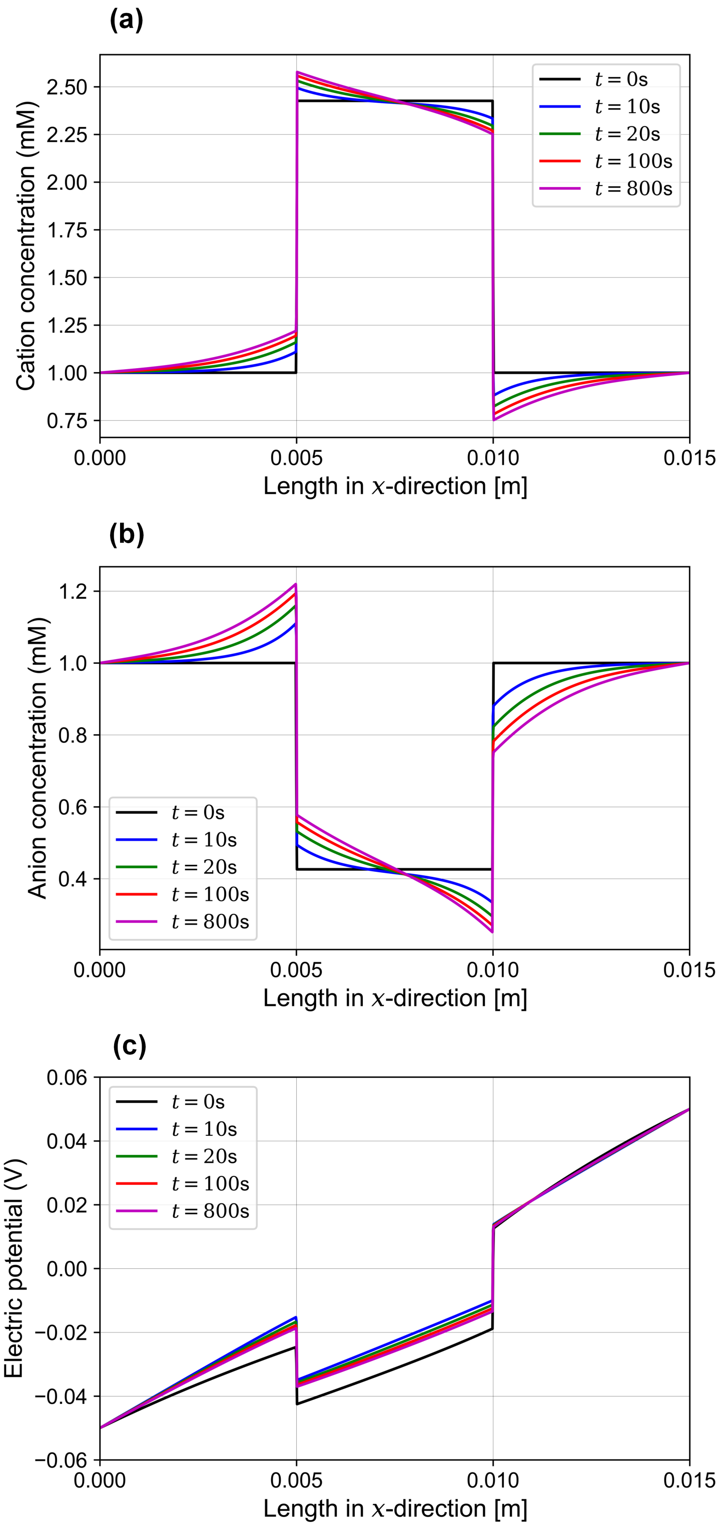

Figure 6.11: Transient variation of quantities for a hydrogel scaffold immersed in solution along the x-direction at $y = 0.0075\,\mathrm{m}$: (**a**) cation concentration, (**b**) anion concentration, (**c**) electric potential.

error using the relation

$$L^2 \text{ error} = \|u_i - u_{i-1}\|_2 = \sqrt{\int_\Omega (u_i - u_{i-1})^2 dA} \tag{6.22}$$

A steadily converging solution is observed as it is evident from Figure 6.13. The global convergence error for the ionic concentrations and the electric potential distribution has the descend of order 0.3.

6.4.4 Limitations

The presented model still has some limitations that are briefly mentioned here. The presented numerical method does not explicitly include cells and is thus not capable of estimating an effect on chondrocytes. The numerical method in its current state is also rather expensive and needs tuning on the numerical side. A quantitative comparison to experiment data cannot yet be established since some material parameters like ion mobility and diffusion coefficient have not yet been experimentally measured by the scientific community.

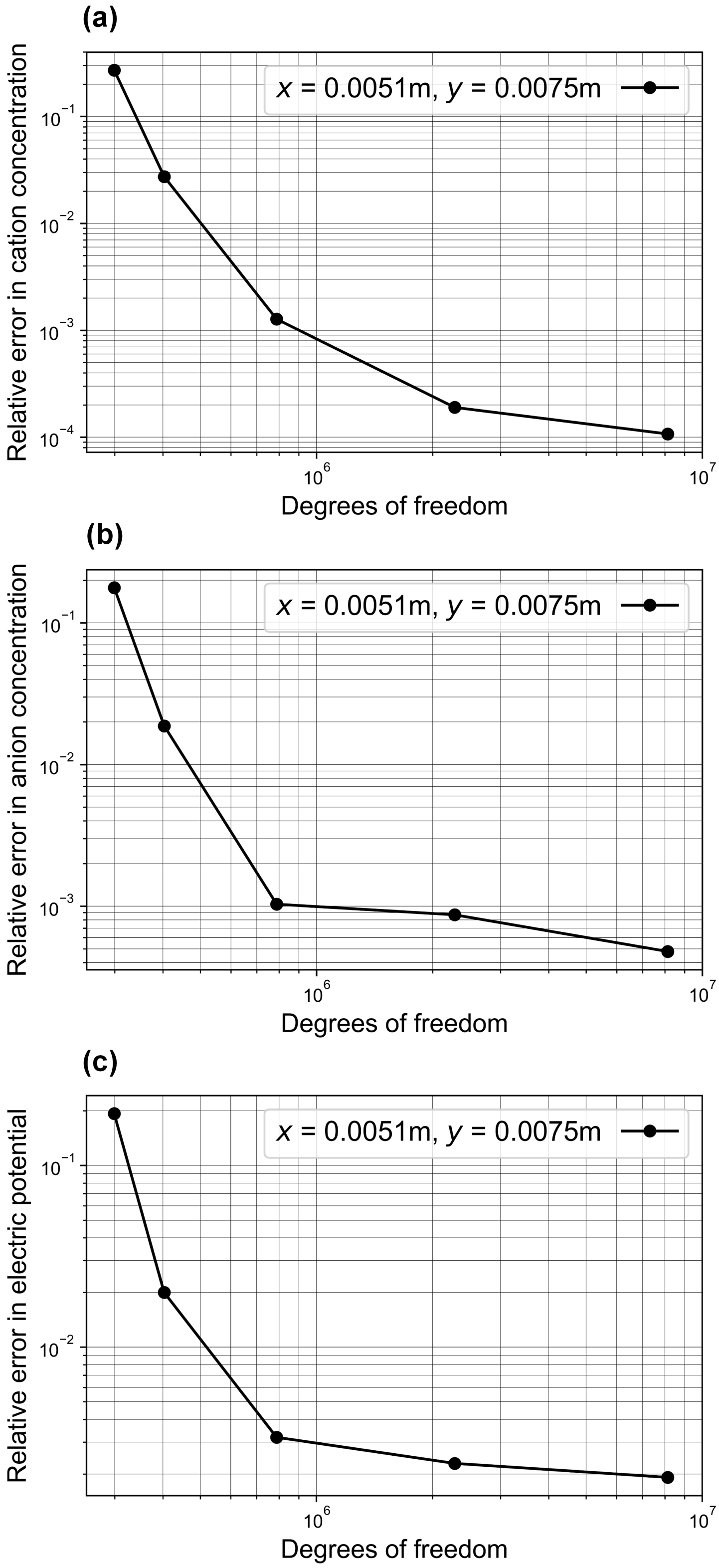

Figure 6.12: Relative error according to Equation (6.21) as observed at the representative point: **(a)** cation concentration, **(b)** anion concentration, **(c)** electric potential.

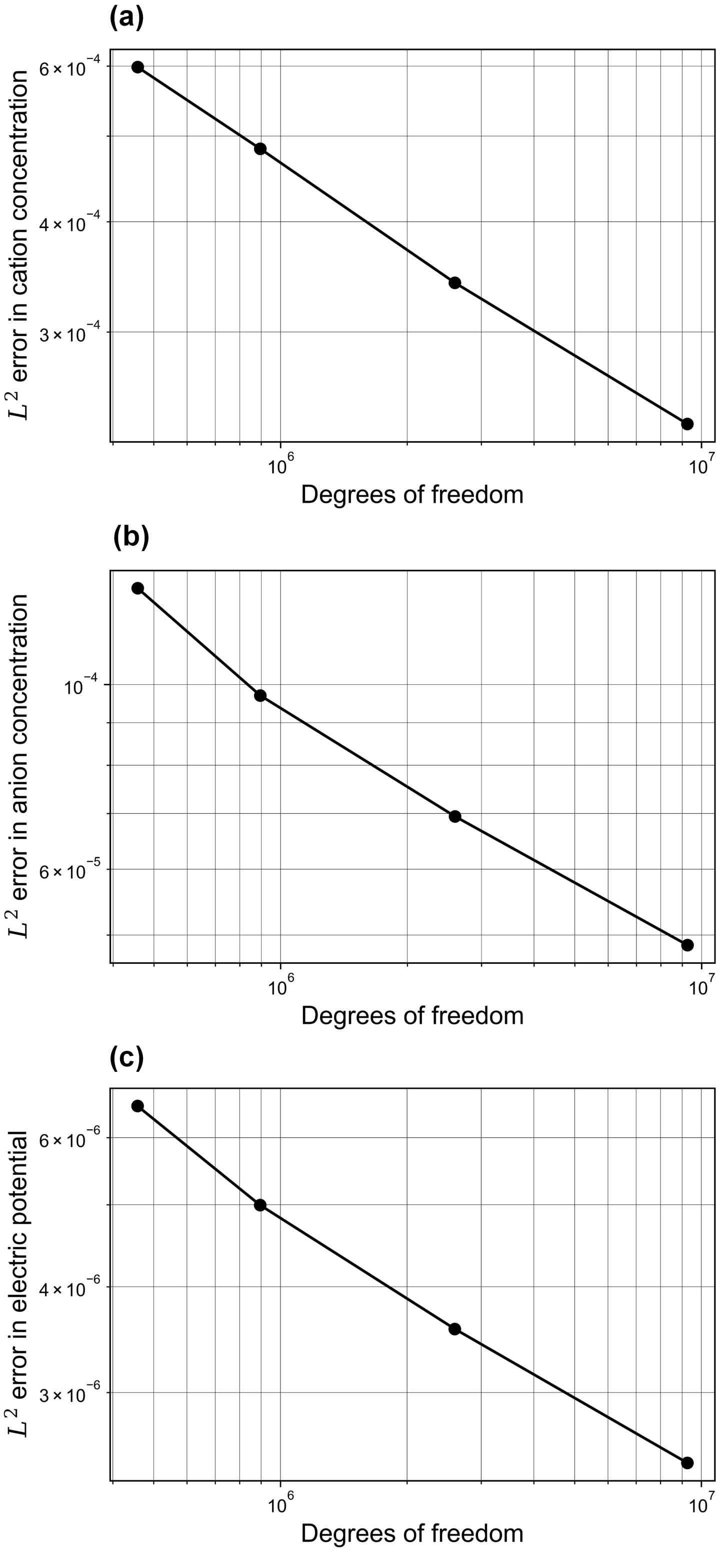

Figure 6.13: Global convergence by evaluating L^2 error according to Equation (6.22): **(a)** cation concentration, **(b)** anion concentration, **(c)** electric potential.

7 Electromechanics of Electroactive Scaffolds for Cartilage–Tissue Repair

7.1 Overview

Repair of articular cartilage tissue using electroactive scaffolds and biophysical stimuli like electrical and osmotic stimulation may have the potential to heal cartilage defects occurring due to trauma, osteoarthritis or sport-related injuries. So, the focus of current study was to present a model for the numerical simulation of electroactive hydrogels for the cartilage–tissue repair as the first step towards an optimized experimental design. The multiphysics transport model that includes the Poisson–Nernst–Planck equations and the mechanical equation is used to find the electrical stimulation response of the polyectrolyte hydrogels. Based upon this, a numerical model on electromechanics of electroactive hydrogels seeded with chondrocytes is presented employing the open-source software FEniCS, which is a Python library for finite-element analysis. The ionic concentrations and electric potential in a hydrogel sample and the cell culture medium, the osmotic pressure created due to ionic concentration variations and the resulting hydrogel displacement were analyzed. The proposed mathematical model was validated at various steps with examples from literature. The presented formulation for the electrical and osmotic stimulation of a hydrogel sample can serve as a model for the development and analysis of a cartilaginous scaffold employing electrical stimulation. By analyzing various parameters, the way is paved for future research on a finer scale using open-source software.

7.2 Introduction

Computational or mathematical modeling has the key role in the improvement of tissue-repair approaches [227]. Experimentalists can test certain hypotheses *in silico* as performing them physically might be prohibitive due to ethical, technical, and safety reasons [228]. Furthermore, studying even a simplified mathematical model which ignores much details of biological processes can still be useful in improving the experimental design [31, 229].

Application of biophysical stimuli results in difference of ionic concentrations between the extracelluar matrix and the electrolyte solution which creates an osmotic pressure and swelling in the cartilage [230]. The osmotic pressure plays a significant role for the exchange of essential nutrients and waste products which are ultimately responsible for cartilage growth, stability, and flexibility [11, 17]. Variation in calcium ion concentration is the first and fundamental response of the chondrocytes to different biophysical cues (electrical, magnetic, and osmotic etc.), although each type of stimulation has a different mechanism to induce the calcium ion oscillations [231–233]. Moreover, multiple biophysical cues similar to those experienced by the native cartilage are crucial for tissue-engineering of functional and viable neocartilage [17, 104].

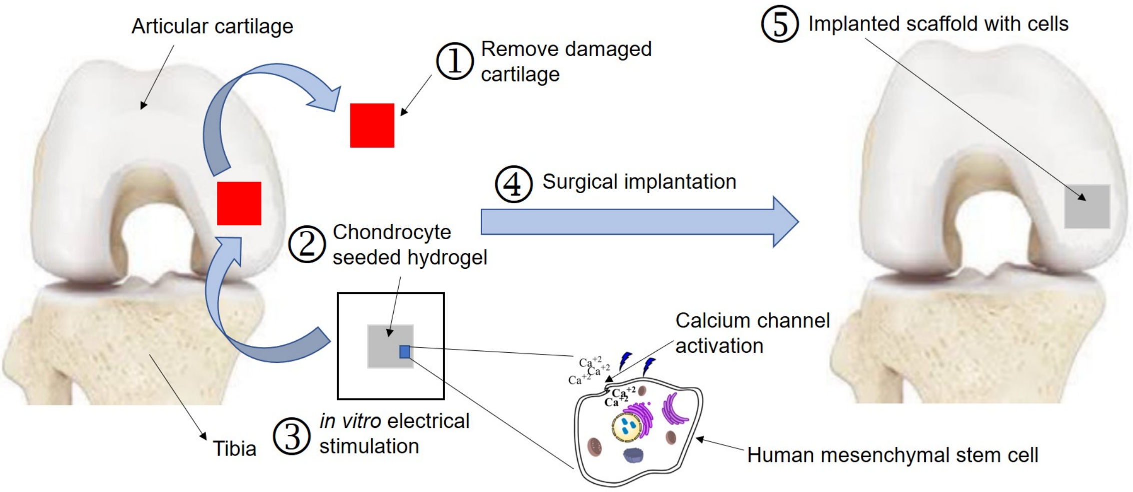
Articular cartilage
① Remove damaged cartilage
⑤ Implanted scaffold with cells
④ Surgical implantation
② Chondrocyte seeded hydrogel
Calcium channel activation
Ca^{+2}
Tibia
③ *in vitro* electrical stimulation
Human mesenchymal stem cell

Figure 7.1: Different steps for the cartilage–tissue repair employing electrical stimulation by transplanting chondrocyte-seeded hydrogel at the defect site (adapted with permission from [7]).

One tissue-engineering strategy for the regeneration of cartilage is using a hydrogel scaffold seeded with chondrocytes to recapitulate the native tissue environment *in vitro* by applying biophysical stimuli like electrical and osmotic stimulation before implantation into the defect site [99]. The complete approach for tissue-engineering is illustrated in Figure 7.1. The electrical stimulation part of the tissue-engineering strategy and the osmotic pressure generated *in vitro* thereof are of interest here, as schematically illustrated in Figure 7.2. A two-dimensional square specimen immersed in solution bath is considered for the finite-element simulations in the following.

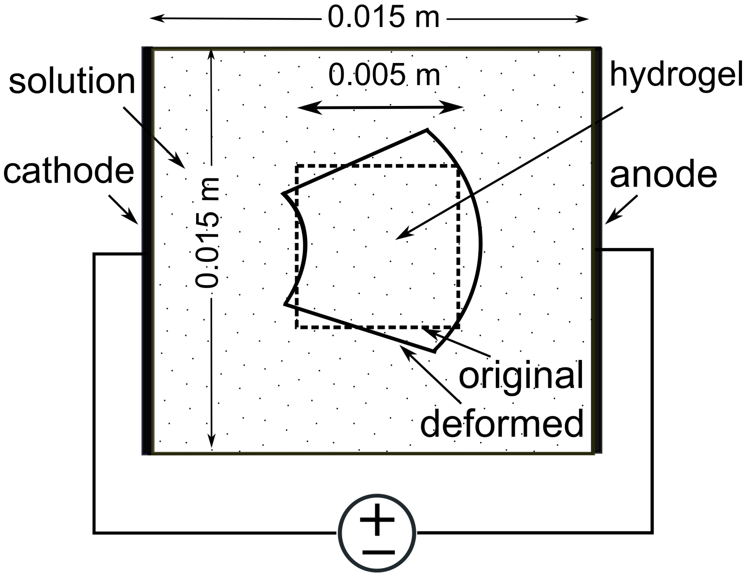
0.015 m
0.005 m
0.015 m
solution
cathode
hydrogel
anode
original
deformed
±

Figure 7.2: Sketch of a hydrogel in a electrolyte solution exposed to an external electric field.

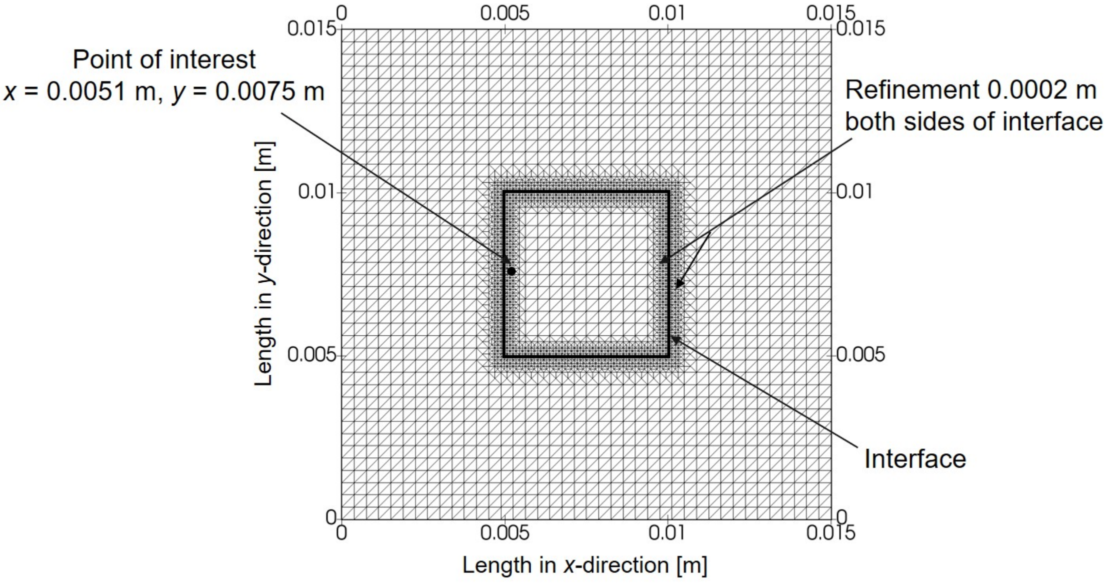
Point of interest
x = 0.0051 m, y = 0.0075 m
Refinement 0.0002 m
both sides of interface
Interface
Length in y-direction [m]
Length in x-direction [m]
0
0.005
0.01
0.015

Figure 7.3: Local mesh refinement used at the interface.

7.3 Mathematical Model

As experimental analysis alone cannot fulfill the requirements for novel and complex applications, progress has been made for theoretical modeling of electroactive hydrogels immersed in the electrolyte solution exposed to external electrical stimulation. For example, Doi *et al.* [205], and Shiga *et al.* [204, 234] investigated the behavior of electrically stimulated hydrogels incorporating the statistical treatment proposed by Flory and Rehner [202, 235, 236] and Donnan's equilibrium theory [203]. Similarly, Grimshaw *et al.* [206, 237] using Nernst-Planck and Donnan equations, highlighted the electrically induced swelling in the polyelectrolyte hydrogels. However, these models are not suited for accurately describing the behavior of hydrogels under electrical stimulation.

The biphasic theory was first communicated by Mow *et al.* [21] for modeling the electromechanical behavior of articular cartilage. Later, this theory was extended to include the ionic phase to give the triphasic [158], quadphasic [159], and then being generalized to a multiphasic theory [160]. Based upon these continuum theories, Gu *et al.* [163, 174] investigated the cartilage tissue under the electro-osmosis phenomenon. But all these theories were more suited for the mechanical stimulation response of the cartilage tissue. The multiphasic theory was used by Zhou *et al.* [207] and Hon *et al.* [238] for the modeling of hydrogels immersed in solution bath. However, this approach had limited applicability since the computational domain was restricted to the hydrogel sample.

Li *et al.* [208, 239] composed a comprehensive multiphasic model based upon mixture theories and added the Poisson–Nernst–Planck equations to study the deformation behavior of hydrogels under the effect of electrical stimulation. The multiphasic model is superior to others since it describes the solvent phase together with the ionic diffusion and deformation of the hydrogel. But it has more unknown independent variables as compared to any other model.

The transport model was first proposed by Grimshaw *et al.* [206] and later improved by Wallmersperger *et al.* [8, 209] for investigating the polyelectrolyte hydrogel behavior under electrical stimulation. The transport model only describes the ionic concentrations and the hydrogel deformation due to local variations of ion concentrations but neglects water flow. In place of the fluid pressure, the osmotic pressure, arising due to local ionic concentration differences, is considered. Knowing the distribution of ions, the osmotic pressure inside the hydrogel can be calculated.

Both multiphasic and the transport models rely on the nonlinear Poisson–Nernst–Planck equations for describing the ionic concentrations and electrical potential. However, the difference is in the way they couple the mechanical equilibrium equation and the electrochemical response. The transport model has the advantage of less number of unknowns. Hence, the transport model presented by Wallmersperger *et al.* [8] has been used for the finite-element simulations and comparison of results. The geometry comprising a square hydrogel sample is shown in Figure 7.2. As the cells occupy a very small volume (1–5%) [58], they have been ignored for the current mesoscale simulations. In the future, the model can be augmented to study effects on the cellular level as well. The electromechanical behavior of the hydrogel is dictated by the chemical, electrical, and the mechanical fields. Two nonlinear, coupled partial differential equations, namely Poisson and Nernst–Planck equations are employed for describing the electrical and chemical fields, respectively, while the momentum equation is used to describe the mechanical field. These equations are described below.

7.3.1 Poisson Equation

The electrical potential is described by the Poisson equation

$$\nabla^2\psi + \frac{F_c}{\varepsilon_r\varepsilon_o}\left(\sum_{k=1}^{n} z^k c^k + z^f c^f\right) = 0 \tag{7.1}$$

where ψ is the electric potential, F_c is Faraday's constant, ε_o is the dielectric constant, ε_r is the relative permittivity of the cell culture medium, $c^{k,f}$ are the ionic concentrations with valence $z^{k,f}$. Note that c^f corresponds to fixed (immobile) ions, while c^k corresponds to mobile ions.

For the two-dimensional problem of Figure 7.2, the homogeneous Neumann boundary conditions are considered at the top and bottom surface, whereas non-homogeneous Dirichlet boundary conditions are assumed at the left and right side of the bath solution. Then, Poisson's equation in Galerkin form of the finite-element formulation reads [122]

$$\int_\Omega \nabla\psi \cdot \nabla v_\psi dA = \frac{F_c}{\varepsilon_r\varepsilon_o}\int_\Omega \left(z^+c^+ + z^-c^- + z^f c^f\right) v_\psi dA \tag{7.2}$$

where dA represents the two-dimensional differential element for integration over the domain Ω, v_ψ is the test function, whereas two ionic species, i.e., cations ' $+$ ' and anions ' $-$ ', have been considered. The test function is considered to vanish, where boundary conditions are imposed.

7.3.2 Nernst-Planck Equation

The ionic concentrations are described using the total flux $\mathbf{J}^k$ of the Nernst-Planck equation, which reads

$$\mathbf{J}^k = -\left(D^k\nabla c^k + D^k c^k \nabla \ln f^k + z^k\vartheta^k c^k \nabla\psi\right) + c^k\nu \tag{7.3}$$

where ν is the area-averaged fluid velocity, D^k is the diffusivity of the kth ionic species, and ϑ^k is the ionic mobility. Under the assumption that neither chemical reactions nor convection occur, the continuity equation for the ionic flux through the hydrogel scaffold and the cell culture medium is

$$\frac{\partial c^k}{\partial t} + \nabla\cdot \mathbf{J}^k = 0. \tag{7.4}$$

Then the continuity Equation (7.4) for the stationary solution becomes [214–216]

$$\nabla\cdot \left(D^k \nabla c^k + z^k \vartheta^k c^k \nabla\psi \right) = 0. \tag{7.5}$$

The Nernst-Einstein relationship [217] for relating the diffusivity to ionic mobility is

$$\vartheta^k = \frac{D^k F_c}{RT} \tag{7.6}$$

with T the absolute temperature, and R is the universal gas constant. Using ϑ^k, Equation (7.5) becomes

$$\nabla\cdot \left(D^k \nabla c^k + \frac{z^k F_c}{RT} D^k c^k \nabla\psi \right) = 0. \tag{7.7}$$

By multiplication with a test function v_k and integrating over the domain Ω, the Galerkin formulation of Equation (7.7) is obtained,

$$D^k \int_\Omega \nabla c^k \cdot \nabla v_k dA + D^k \frac{z^k F_c}{RT} \int_\Omega c^k \nabla\psi \cdot \nabla v_k dA = 0. \tag{7.8}$$

In the first step, the Poisson–Nernst–Planck equations are solved numerically using a mixed-function space [219]. This function space consists of second-order Lagrange elements to describe the three scalar functions for anion as well as cation distribution, and the electric potential [116, 198]. The given nonlinear problem was solved using the 'NonLinearVariationalSolver' of FEniCS [118] based on Newton's method with the associated solver 'MUMPS' (MUltifrontal Massively Parallel sparse direct Solver) [220]. MUMPS is a direct solver used for the solution of the linear system occurring within Newton's iterations [118]. In the next step, this solution of the Poisson–Nernst–Planck equations is used to find the osmotic pressure and displacement.

7.3.3 Osmotic Pressure and Momentum Equations

The equation of motion to find the displacement for small deformations is [240, 241],

$$\Psi \frac{\partial^2 \mathbf{u}}{\partial t^2} + \Upsilon \frac{\partial \mathbf{u}}{\partial t} = \nabla\cdot \sigma + \Psi \mathbf{d} \tag{7.9}$$

where $\mathbf{u}$ is the displacement vector, Ψ is the effective density of the gel, Υ represents the viscous damping between the electrolyte and the polymer fibers, σ is the stress tensor, and $\mathbf{d}$ is the body force. The friction can be neglected due to the absence of body forces and Equation (7.9) reduces to,

$$\Psi \frac{\partial^2 \mathbf{u}}{\partial t^2} = \nabla \cdot \sigma. \tag{7.10}$$

Since the redistribution processes of the ionic charges happen at a much lower rate compared to the hydrogel deformation, a quasi-static state can be considered and Equation (7.10) becomes,

$$\nabla \cdot \sigma = 0. \tag{7.11}$$

Further, due to the application of a low potential difference, the electrostatic stress is neglected and Equation (7.11) becomes,

$$\nabla \cdot \left(-p_{osm}\mathbf{I} + \lambda_s \mathrm{tr}(\mathbf{S})\mathbf{I} + 2\mu_s \mathbf{S} \right) = 0 \tag{7.12}$$

where λ_s and μ_s are the Lamé constants, $\mathbf{I}$ is the identity tensor, $\mathbf{S}$ is the strain tensor, $\mathrm{tr}(\mathbf{S})$ is the trace of the strain tensor, and p_{osm} is the osmotic pressure.

The osmotic pressure which depends on the ion concentrations can be calculated by the expression [242],

$$p_{osm} = RT \sum_{k=+,-} \left(c^k_{gel} - c^k_{sol} \right) \tag{7.13}$$

where c^k_{gel} and c^k_{sol} are the concentrations of the kth ion species in the hydrogel and in the solution next to the hydrogel, respectively. For the steady state one-dimensional simulations, Equation (7.12) becomes,

$$(3\lambda_s + 2\mu_s)\frac{\partial^2 u}{\partial x^2} - \frac{\partial p_{osm}}{\partial x} = 0. \tag{7.14}$$

The linear elastic equation at equilibrium that governs the one-dimensional steady state mechanical deformation of hydrogels [243] is,

$$(3\lambda_s + 2\mu_s)\frac{\partial^2 u}{\partial x^2} - RT\frac{\partial}{\partial x}\left(\sum_{k=+,-} \left(c^k_{gel} - c^k_{sol} \right) \right) = 0. \tag{7.15}$$

The Galerkin form of Equation (7.15) is,

$$\begin{aligned} &(3\lambda_s + 2\mu_s)\left(\int_{\partial\Omega} \frac{\partial u}{\partial n} v_u ds - \int_{\Omega} \frac{\partial u}{\partial x} \cdot \frac{\partial v_u}{\partial x} dx \right) \\ &- RT\left(\int_{\Omega} \frac{\partial}{\partial x}\left(\sum_{k=+,-} \left(c^k_{gel} - c^k_{sol} \right) \right) v_u dx \right) = 0 \end{aligned} \tag{7.16}$$

where v_u is the test function for the displacement and dx denotes the one-dimensional differential element for integration. Applying homogeneous Neumann boundary conditions, Equation (7.16) reduces to,

$$-\left(3\lambda_s + 2\mu_s\right) \int_\Omega \frac{\partial u}{\partial x} \cdot \frac{\partial v_u}{\partial x} dx = RT \left(\int_\Omega \frac{\partial}{\partial x} \left(\sum_{k=+,-} \left(c^k_{gel} - c^k_{sol} \right) \right) v_u dx \right). \tag{7.17}$$

The complete simulation scheme is shown in Figure 7.4.

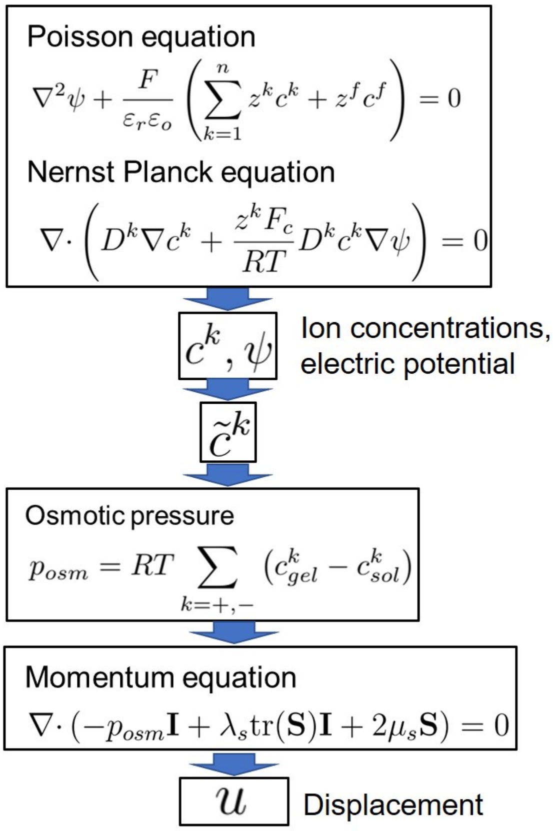
Poisson equation
$\nabla^2\psi + \frac{F}{\varepsilon_r\varepsilon_o}\left(\sum_{k=1}^{n} z^k c^k + z^f c^f\right) = 0$
Nernst Planck equation
$\nabla\cdot\left(D^k\nabla c^k + \frac{z^k F_c}{RT} D^k c^k \nabla\psi\right) = 0$
c^k, ψ
Ion concentrations, electric potential
$\tilde{c}^k$
Osmotic pressure
$p_{osm} = RT \sum_{k=+,-} \left(c^k_{gel} - c^k_{sol}\right)$
Momentum equation
$\nabla\cdot\left(-p_{osm}\mathbf{I} + \lambda_s \mathrm{tr}(\mathbf{S})\mathbf{I} + 2\mu_s\mathbf{S}\right) = 0$
u
Displacement

Figure 7.4: Simulation flow chart of the problem.

7.4 Results

For validation of the proposed simulation scheme, Equations (7.2), (7.8), and (7.17) were solved numerically by means of the simulation scheme described in Figure 7.5. The initial concentration of fixed negative ions was $c^f = 8\,\mathrm{mM}$, while all other quantities for the simulation are described in Table 7.1. The displacement of the hydrogel obtained as last step of the model was compared to the displacement result of multiphasic theory from the study reported by Li *et al.* [244]. It is evident from Figure 7.5 that both results are in good agreement which verifies the current modeling approach using the open-source software. In the following, the model is explained in detail making comparisons to the examples from literature.

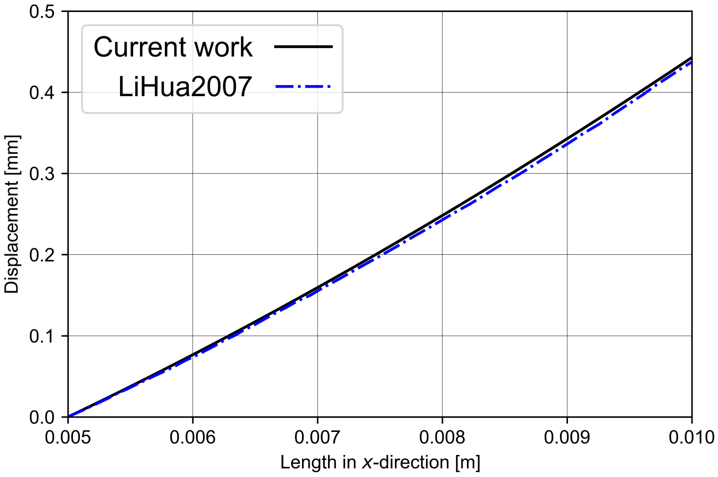

Figure 7.5: Comparison for the distribution of horizontal displacement of the hydrogel.

7.4.1 Chemical Stimulation

The hydrogel sample with initial concentration of fixed negative charges $c^f = 2\,\text{mM}$ was placed in between the electrodes in a cell culture medium with concentration of $1\,\text{mM}$ as shown in Figure 7.2. For the numerical simulation, a concentration of $1\,\text{mM}$ for both anions and cations was taken as boundary condition at the ends of electrolyte solution. The difference of ionic concentrations between the solution and the hydrogel compels the mobile ions to redistribute in the whole region for maintaining the electroneutrality condition. The ionic concentration difference results in a negative step in the electric potential as displayed in Figure 7.8(b).

The concentration of ions in the hydrogel at Donnan equilibrium can be evaluated using [159, 221]

$$c^{\pm}_{\text{gel}} = \frac{1}{2}\left(\mp c^f + \sqrt{[c^f]^2 + 4[c^{\pm}_{\text{sol}}]^2}\right). \tag{7.18}$$

The corresponding Donnan potential can be found by using the relation [222–224],

$$\Delta\phi = \frac{RT}{z^k F_c}\ln\left(\frac{c^k_{\text{gel}}}{c^k_{\text{sol}}}\right). \tag{7.19}$$

Using Equations (7.18) and (7.19), the concentration of anions, cations and the Donnan potential were found to be 0.4142 mM, 2.4142 mM, and −22.2522 mV, respectively. Similar results were obtained by numerically solving the Equations (7.2) and (7.8) which also agree to the results reported by Wallmersperger *et al.* [8].

The mesh was refined locally such that the maximal edge length was 0.0002 m on either side of the interface as shown in Figure 7.3. This refinement was used for all the simulations to obtain good convergence of the solution. The parameters used are listed in Table 7.1 and the simulation results are shown in Figures 7.6–7.8.

7.4.2 Electrical Stimulation

The chemo-electrical behavior of the hydrogel sample under electrical stimulation is considered in this section. For the two-dimensional numerical simulation, the concentration of negative fixed charges for the hydrogel was set to $c^f = 2\,\mathrm{mM}$. For the concentration of free Na^+ and Cl^- ions in the solution, the concentrations at the electrodes were set to $c^+ = c^- = 1\,\mathrm{mM}$ using the Dirichlet boundary conditions. A constant electric potential of −100 mV was prescribed directly at the cathode and +100 mV at the anode. As initial condition for numerical simulation, the results of the chemical stimulation, i.e., without applied external electric field were used. Other quantities used for the numerical solution were identical to those for the chemical stimulation, as given in Table 7.1.

The presented numerical results for the chemical and electrical stimulation are in accordance to the numerical simulation results reported by Wallmersperger *et al.* [8] except that here the value of applied electric potential is ±100 mV instead of ±50 mV. The presented results also agree qualitatively to the experimental results reported by Gülch *et al.* [225].

The computation time for the two-dimensional Poisson–Nernst–Planck equations under electrical stimulation was ∼10 min with 10,387,755 degrees of freedom. The number of degrees of freedom was estimated by the convergence analysis as discussed in Section 7.5.1. This large number of the degrees of freedom is necessary as the coupled Poisson–Nernst–Planck equations are nonlinear, and the solution tends to become unstable at the hydrogel-solution interface by the occurrence of nonphysical negative ionic concentrations. The simulations were performed on a computer with Intel(R) Xeon(R) E5-2687W v4 CPU @ 3.00 GHz with 256 GB RAM without using parallelization. The Python scripts related to the current study can be accessed through an online repository (`https://github.com/arfarooqi/Electromechanics_hydrogels`).

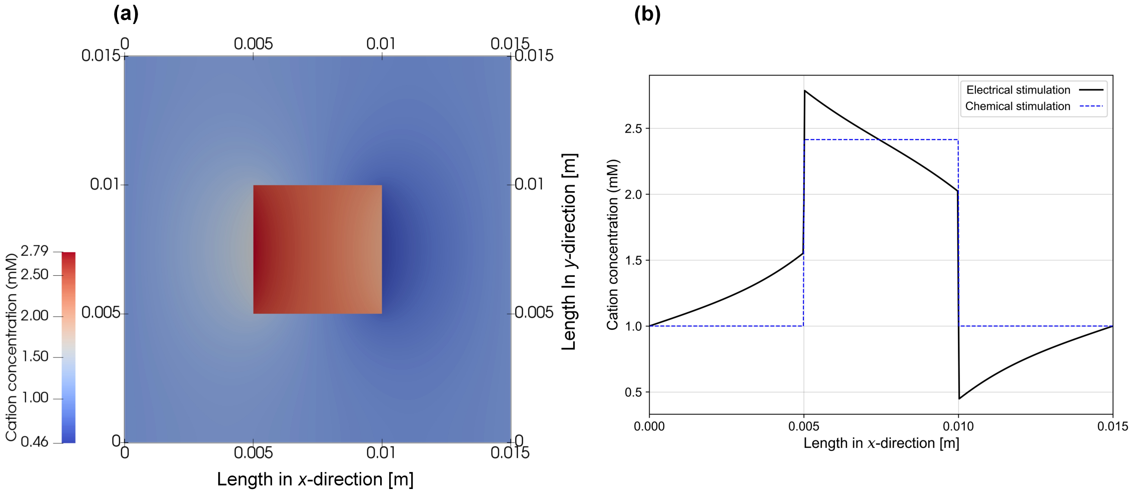

Figure 7.6: Cation concentration distribution: **(a)** under electrical stimulation, **(b)** under chemical or electrical stimulation, respectively, at $y = 0.0075\,\mathrm{m}$ versus the x-direction.

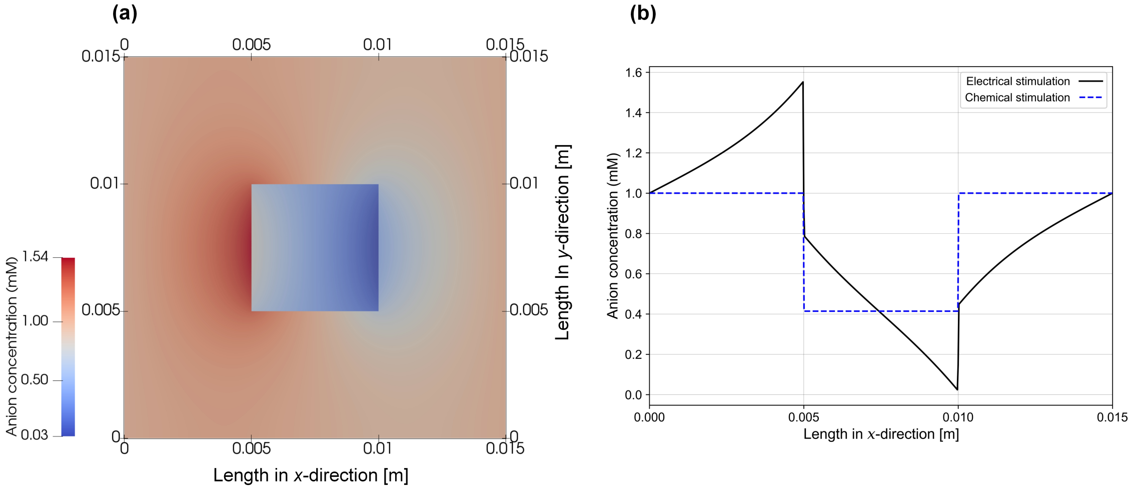

Figure 7.7: Anion concentration distribution: **(a)** under electrical stimulation, **(b)** under chemical or electrical stimulation, respectively, at $y = 0.0075\,\mathrm{m}$ versus the x-direction.

7.4.3 Osmotic Stimulation and Displacement

This osmotic pressure created due to the difference of ionic concentrations compels the hydrogel to take up solvent, resulting in hydrogel swelling. The osmotic pressure can be associated to a strain imposed on the mechanical field Equation (7.12). The method reported by Wallmersperger *et al.* [245] was used to find the osmotic pressure

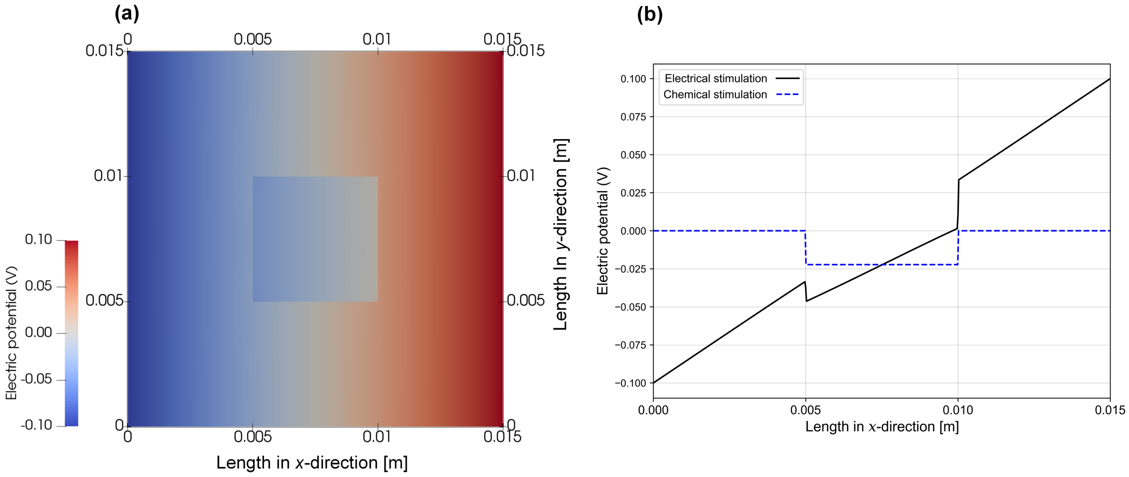

Figure 7.8: Electric potential distribution: **(a)** under electrical stimulation, **(b)** under chemical or electrical stimulation, respectively, at $y = 0.0075\,\mathrm{m}$ versus the x-direction.

Table 7.1: Quantities used for simulations in accordance with [9].

Parameter	**Value**
Ionic mobility ϑ^k	$3.9607 \times 10^{-6}\,\mathrm{m^2\,s^{-1}\,V^{-1}}$
Ionic diffusion coefficient D^k	$1.0 \times 10^{-7}\,\mathrm{m^2\,s^{-1}}$
Gas constant R	$8.3143\,\mathrm{J\,mol^{-1}\,K^{-1}}$
Temperature T	$298.0\,\mathrm{K}$
Relative permittivity ε_r	80.0
Vacuum permittivity ε_o	$8.854 \times 10^{-12}\,\mathrm{A\,s\,V^{-1}\,m^{-1}}$
Faraday constant F_c	$9.6487\,\mathrm{C\,mol^{-1}}$
Ionic valence z^k	± 1.0
Fixed charge valence z^f	-1.0
Lamé coefficient $3\lambda_s + 2\mu_s$	$1.2 \times 10^5\,\mathrm{Pa}$
External electric potential ψ	$\pm 100\,\mathrm{mV}$
Hydrogel dimensions	$0.005 \times 0.005\,\mathrm{m^2}$
Solution bath dimensions	$0.015 \times 0.015\,\mathrm{m^2}$

difference. As evident from Figure 7.9, the osmotic pressure varies in the entire hydrogel sample and should be determined locally. To attain this, information about the non-local values of the corresponding ionic concentrations in the nearby solution are required. Thus, two artificial degrees of freedom are introduced which interpolate the ionic concentrations of mobile ions at the hydrogel-solution interface into the hydrogel. These degrees of freedom are represented by $\tilde{c}^{+}(x)$ and $\tilde{c}^{-}(x)$ for cations and anions, respectively. More specifically, the local value of the one-dimensional osmotic pressure difference as function of x can be calculated using Equation (7.13) as

$$p_{osm} = RT\left[c^{+}_{gel}(x) - \tilde{c}^{+}(x) + c^{-}_{gel}(x) - \tilde{c}^{-}(x)\right]. \tag{7.20}$$

The osmotic pressure evaluated for the hydrogel is illustrated in Figure 7.10 which serves as input for the mechanical field Equation (7.15).

It is not reasonable to start the solution of the system from the complete dry condition. Thus, an initial osmotic pressure p_{ini} is introduced into the mechanical equation. This initial value can be found using the osmotic pressure created due to the chemical stimulation as

$$p_{ini} = RT\left(c^{+}_{gel} - c^{+} + c^{-}_{gel} - c^{-}\right). \tag{7.21}$$

For the current case, the initial osmotic pressure using Equation (7.13) is found to be 2.052 kPa and Equation (7.15) can be written as

$$(3\lambda_s + 2\mu_s)\frac{\partial^2 u}{\partial x^2} - RT\frac{\partial}{\partial x}\left(\sum_{k=+,-}\left(c^{k}_{gel} - c^{k}_{sol}\right) - p_{ini}\right) = 0. \tag{7.22}$$

Solving Equation (7.22) numerically gives the hydrogel displacement as illustrated in Figure 7.11 which is in agreement to the numerical result reported by Li *et al.* [9].

7.5 Discussion

Applying electrical stimulation to the hydrogel sample immersed in the solution bath causes the ions to redistribute in the hydrogel and solution. It is because of a higher potential difference created on one side of the hydrogel and a lower on the other side. Due to the fixed charges attached to the polymers of the hydrogel, the diffusion process causes ionic concentration differences between the exterior solution and the interior hydrogel. So, there is an increased swelling on one side whereas a reduced swelling takes place on the other side. Accordingly, the ionic concentration difference results in an osmotic pressure which causes the shrinking or swelling of the hydrogel. The deformation of the hydrogel induces reorganization of the diffused ions and bound anionic charges resulting in modified ionic concentration differences and the hydrogel bends. This mechanism continues till the increase in mechanical energy equalizes the decrease in free energy of the system.

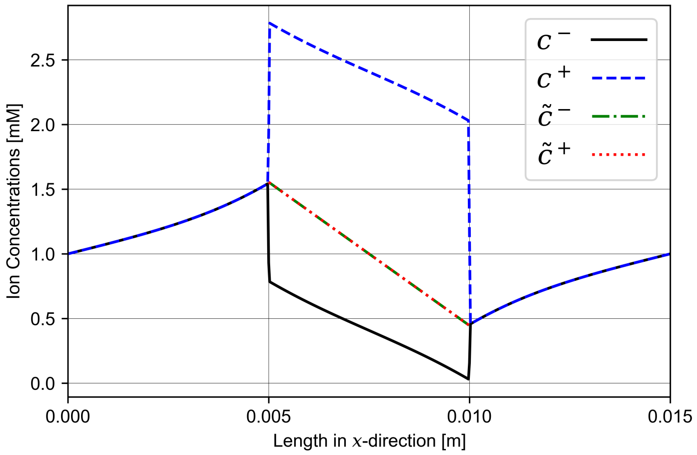

Figure 7.9: Ionic concentration distributions to evaluate the osmotic pressure difference for the electro-chemo-mechanical coupling scheme under electrical stimulation.

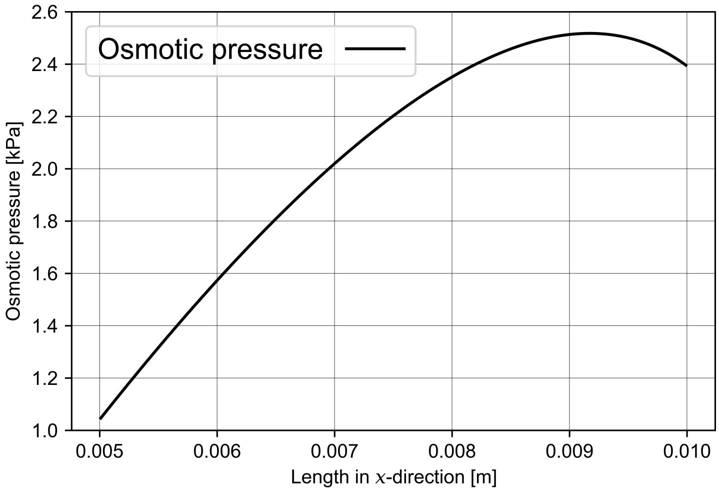

Figure 7.10: Osmotic pressure in the hydrogel due to variation of ionic concentrations.

The bending direction depends on the type of hydrogel (anionic or cationic fixed charge groups) and the polarity of the applied electrical stimulation. With anionic hydrogels, there is an increase in the potential difference or an additional swelling on the side facing the anode and a decrease in the potential difference or a shrinkage on the opposite side. This leads to a bend in the direction of the cathode as shown in Figure 7.2. For cationic hydrogels, however, the reverse effect occurs, i.e., they bend towards the anode.

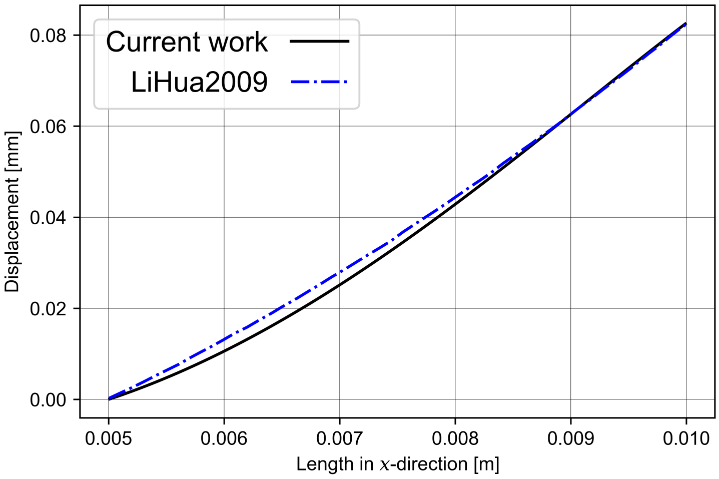

Figure 7.11: Comparison for the distribution of horizontal displacement of the hydrogel.

Various approaches for cartilage–tissue repair were experimentally performed using electrical [74, 199, 200, 246, 247] and osmotic [11, 248, 249] stimulation but appropriate computational models have still not been presented. Keeping this in mind, a mathematical model has been proposed to comprehend the experimental procedures for engineering of cartilage tissue using electrical and osmotic stimulation. The proposed model was then solved numerically using the open-source platform FEniCS. A similar setup was also experimentally studied by Lim *et al.* [250] using human mesenchymal stem cells under electric stimulation for cell viability, proliferation, and chondrogenic differentiation. These experimental investigations can be enhanced by numerical simulations to study the chondrocyte-hydrogel interactions and transduction pathways at the microscale.

7.5.1 Convergence Analysis

In order to demonstrate convergence of the finite-element simulations, the relative error is evaluated for the ionic concentrations and the electric potential at a representative point ($x = 0.0051\,\mathrm{m}$, $y = 0.0075\,\mathrm{m}$) just inside the hydrogel, while refining the mesh. A local mesh refinement of 0.0002 m was used on both sides of the interface as shown in Figure 7.3 because it is the region where the solution tends to become unstable. The convergence study was initiated from one refinement cycle in a distance of 0.0002 m on either side of the interface, and ended at the sixth cycle while keeping the mesh in the remaining solution domain constant in each refinement cycle. The relative error is found using the relation

$$\text{relative error} := \frac{|u_i - u_{i-1}|}{|u_i|} \tag{7.23}$$

where u_i and u_{i-1} are the current and previous values of the degrees of freedom, respectively, corresponding to the each refinement cycle. The relative error in the ionic concentrations of anions, cations, and electric potential distribution at a representative point ($x = 0.0051\,\mathrm{m}$, $y = 0.0075\,\mathrm{m}$) is plotted against the degrees of freedom as given in Figure 7.12. Expectedly the relative error reduces as the degrees of freedom increase. This happens in two stages: after a first, steeper descend with the order of approx. 4, the descend reduces to the order of approx. 1 while approaching zero. Clearly, the relative error for anions, cations and electric potential tends to a stable value if the mesh consists of more than 1 million degrees of freedom. The global convergence was checked as well by computing the L^2 error using the relation

$$L^2 \text{ error} = \|u_i - u_{i-1}\|_2 = \sqrt{\int_\Omega (u_i - u_{i-1})^2 dA} \tag{7.24}$$

A steadily converging solution is observed as it is evident from Figure 7.13. The global convergence error for the ionic concentrations of anions, cations, and electric potential distribution has the descend of order 0.3.

7.5.2 Limitations

The numerical model presented here has some limitations. First, the cells have not been included explicitly. Nonetheless the model has the capability to include the cellular inclusions as well. Second, there is an abrupt change in values at the hydrogel-solution interface which is not realistic. This could be addressed by using the model proposed by Li *et al.* [208] but it is characterized by a higher number of unknowns. Third, the current numerical method is rather computationally expensive due to a high number of degrees of freedom. The numerical method can be further optimized e.g. using the physics based refinement [251] instead of the currently used local mesh refinement.

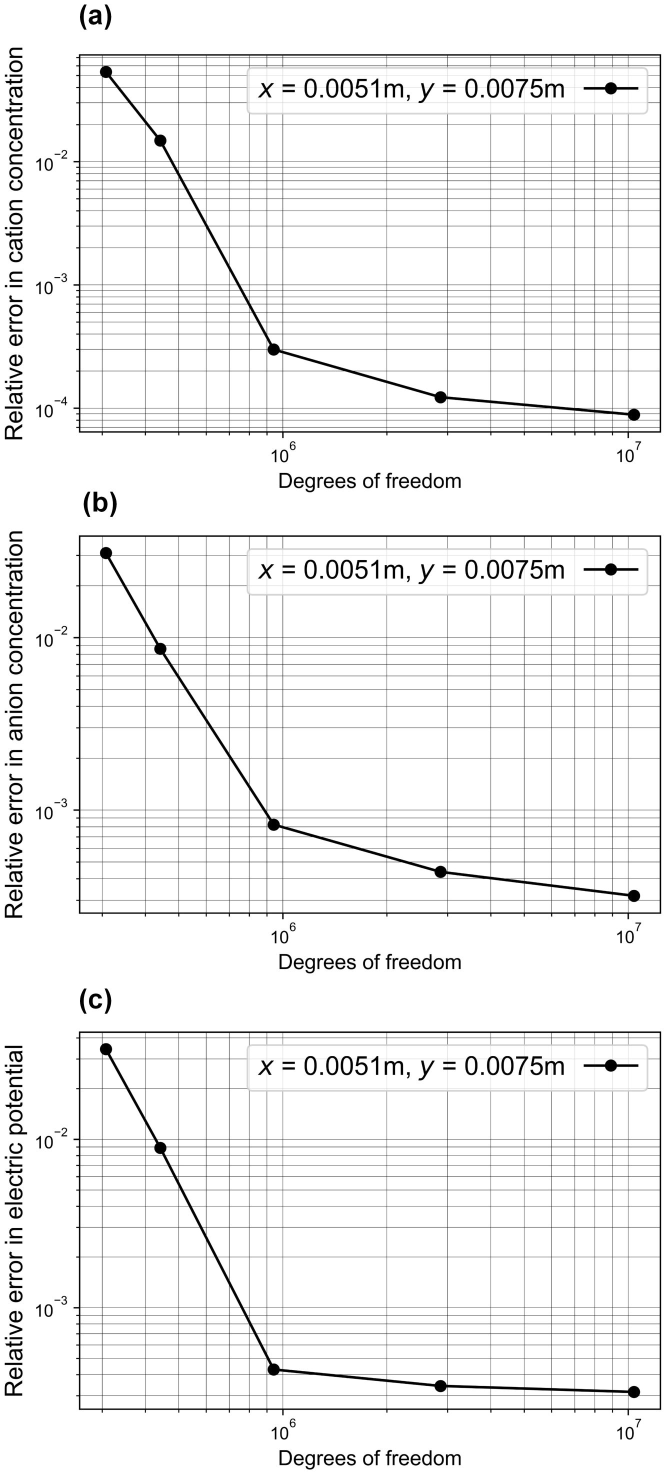

Figure 7.12: Relative error according to Equation (7.23): **(a)** cation concentration, **(b)** anion concentration, **(c)** electric potential.

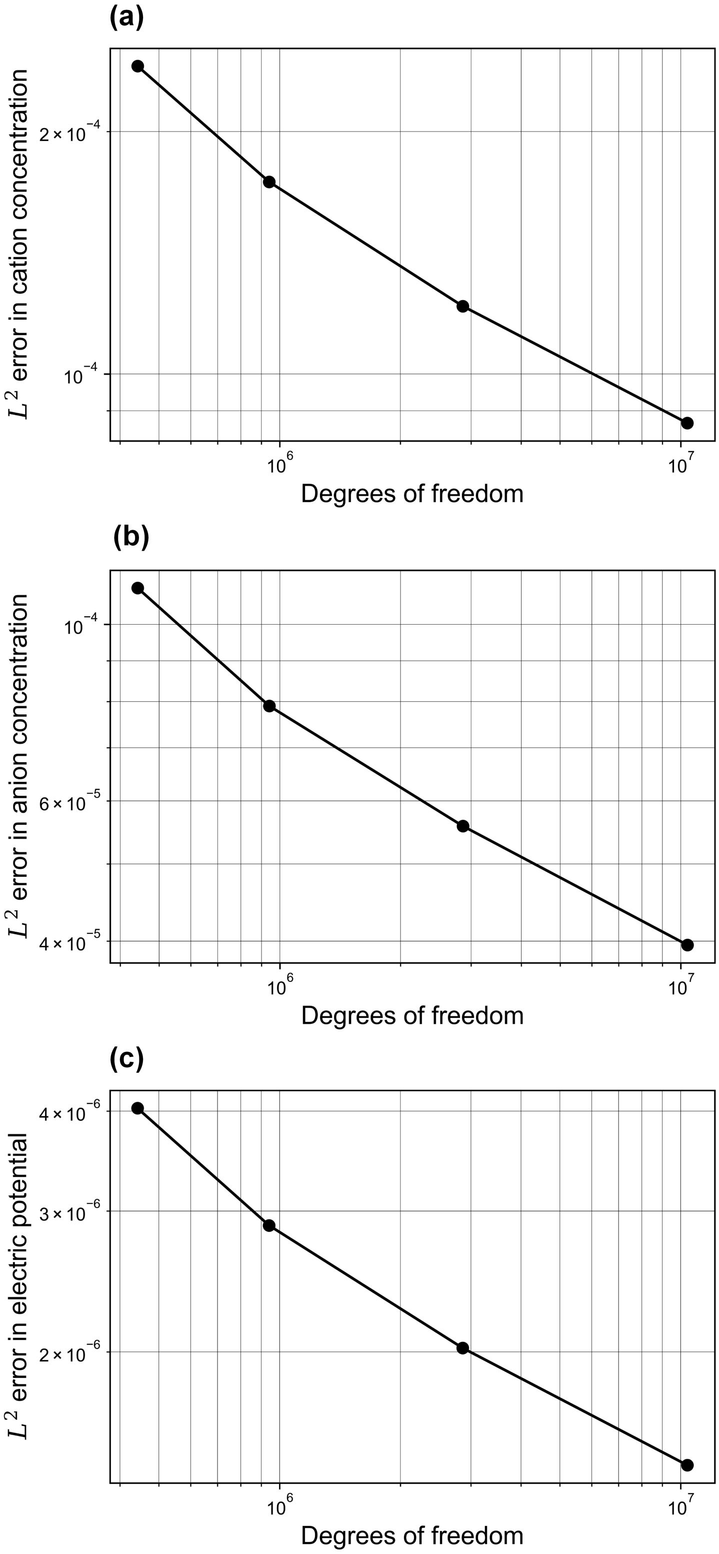

Figure 7.13: Global convergence by evaluating L^2 error according to Equation (7.24): **(a)** cation concentration, **(b)** anion concentration, **(c)** electric potential.

8 Conclusions and Perspectives

The establishment of robust and reproducible computer simulations takes on a pivotal role in complementing novel experimental techniques to understand the state of health and progress of diseases and therefore aid in their diagnosis and treatment. Computational models can be used to simulate the therapeutic outcomes and enable less *in vitro* and *in vivo* studies required [252, 253]. For the cartilage–tissue repair, most of the electrical stimulation studies have been performed with animal and human samples and with living animals, while only a few *in silico* studies are available. Thus, there is a need for *in silico* investigations using electrical stimulation for a complete understanding of the transduction pathways and interaction mechanisms for designing an optimized electrical stimulation protocol for cartilage–tissue repair [154].

The conclusion of this thesis can be described in two parts. The first part starts with summarizing *in silico* investigations discussing the effects of different biophysical stimuli, that is, electrical, mechanical, and chemical stimuli, on the induced electrical properties and physiology of cartilage tissue. Clearly, biophysical stimuli leading to a potential gradient resembling the intrinsic signals are applicable as an additional tool toward the development of optimal therapies for cartilage regeneration. Nevertheless, few models have been proposed to study the *in silico* induced electrical properties of cartilage at the tissue level due to direct electrical stimulation, but a comprehensive and consistent model to observe the electrical interactions at the cellular level is still lacking. Subsequently, the general mathematical formulation for the *in silico* description of the induced electrical properties of cartilage was presented. This formulation is applicable to all the mixture theories starting from the biphasic up to the generalized multiphasic theory. Based upon the summary of *in silico* induced electrical properties of cartilage tissue and their general mathematical description, a preliminary numerical study focusing on the linear electromechanical transduction in a cartilage-tissue sample using the open-source platform FEniCS was presented. The results were compared to the results of the experimental study by Frank and Grodzinsky [19]. Finally, *in vitro* and *in vivo* research studies reported to date using either the direct or indirect electrical stimulation of chondrocytes, cartilage tissue, and cell-seeded hydrogel scaffolds were summarized. It is evident that both types of electrical stimulation could be beneficial for cartilage–tissue repair approaches. However, a complete understanding of the transduction pathways and interaction mechanisms due to electrical stimulation is still lacking for designing an optimized electrical stimulation protocol.

To shortly conclude the first part, cartilage-related *in silico*, *in vitro*, and *in vivo* research studies reported to date were summarized. Based upon this, a general mathematical framework for the investigation of electrical properties was presented, and eventually a preliminary numerical study using an open-source finite-element platform was reported.

Investigating the electrical properties of cartilage *in silico* due to indirect electric stimulation, that is, capacitive and inductive coupling, is still an open research area. In this context, the presented open-source implementation of the electrokinetic phenomena in a cartilage-tissue sample using FEniCS can be useful to study the *in silico* electrical interactions at microscale as well as for modeling of the indirect electric stimulation for the cartilage tissue. For this purpose, the solution of the Poisson–Nernst–Planck equations for the applied alternating-current signal can be the starting point [254, 255].

In the second part of the thesis, the focus of the numerical study was on the first and coarsest level of the experimental design, that is the scale of the hydrogel scaffold and its surrounding medium. By analyzing ionic distributions, electric potential, and the osmotic pressure causing mechanical deformation, the way is paved for future investigations on a finer scale. Moreover, the possibility of coupling the electrochemical model to the mechanical model is explored. By this, eventually the mechanical displacement of the scaffold due to the applied electric stimulation is estimated.

Modeling the behavior of a hydrogel immersed in a solution bath is challenging due to highly coupled nonlinear partial differential equations. To date, the behavior of electroactive hydrogels immersed in a solution has been simulated using custom programs implemented in individual laboratories that are not publicly available. A few of the models have also been implemented using commercial softwares, but mostly for one-dimensional cases. None of the models have been implemented so far using any open-source software and for the electrical stimulation response of the hydrogels in the context of cartilage–tissue repair. Thus, a two-dimensional open-source computational model has been proposed to study the effect of electrical stimulation on a hydrogel scaffold for cartilage–tissue engineering at the mesoscale. The proposed model was verified against results available in the literature and then extended for a circular geometry by solving the Poisson–Nernst–Planck equations using FEniCS. Subsequently, finite-element simulations were performed for the electromechanics of electroactive hydrogels immersed in a solution bath under the effect of electrical and osmotic stimulation. Modeling the behavior of such hydrogel samples under biophysical stimulation is challenging due to nonlinear coupled equations involving the chemical, electrical, and mechanical multiphysics. Thus, the simulations of electroactive hydrogels [256, 257] have been performed using FEniCS in context of the cartilage–tissue repair. The proposed model was validated with data from literature. Furthermore, its application as a model for the tissue engineering using biophysical stimulation is explained in detail. Eventually, successful and validated *in silico* studies will make it possible to perform fewer biological testings for trying different protocols. Also, specialized cues can be designed, i.e., progressing from a trial-and-error approach to a well-controlled experiment planning. The use of open-source software like FEniCS for the finite element simulations is involved as compared to commercial software. It is because one has to define every step, unlike commercial finite-element software, where one can generally put some values by using the graphical user interface.

The proposed model has the capability to include other stimuli like pH, mechanical stress, oxygen, and glucose, or a combination of two or more stimuli [258]. In addition, it can also be used to study drug delivery mechanisms [259]. Moreover, the cellular interactions of chondrocytes with porous hydrogel scaffolds can be modeled at the microscale by the addition of appropriate equations [260]. Thus, the computational models discussed in this thesis are a step forward in establishing comprehensive simulation models for the engineering of optimized cartilage scaffolds.

Bibliography

[1] M. R. Servin-Vences, J. Richardson, G. R. Lewin, K. Poole, Mechanoelectrical transduction in chondrocytes, Clin. Exp. Pharmacol. Physiol. 45 (2018) 481–488. URL: `https://doi.org/10.1111/1440-1681.12917`.

[2] The International Cartilage Regeneration & Joint Preservation Society (ICRS), Cartilage lesion classification system, 2020. URL: `https://cartilage.org/society/publications/icrs-score/`.

[3] H. Kwon, W. E. Brown, C. A. Lee, D. Wang, N. Paschos, J. C. Hu, K. A. Athanasiou, Surgical and tissue engineering strategies for articular cartilage and meniscus repair, Nat. Rev. Rheumatol. 15 (2019) 550–570. URL: `https://doi.org/10.1038/s41584-019-0255-1`.

[4] R. Balint, N. J. Cassidy, S. H. Cartmell, Electrical stimulation: A novel tool for tissue engineering, Tissue Eng. Part B Rev. 19 (2013) 48–57. URL: `https://doi.org/10.1089/ten.TEB.2012.0183`.

[5] G. Thrivikraman, S. K. Boda, B. Basu, Unraveling the mechanistic effects of electric field stimulation towards directing stem cell fate and function: A tissue engineering perspective, Biomaterials 150 (2018) 60–86. URL: `https://doi.org/10.1016/j.biomaterials.2017.10.003`.

[6] C. Chen, X. Bai, Y. Ding, I.-s. Lee, Electrical stimulation as a novel tool for regulating cell behavior in tissue engineering, Biomater. Res. 23 (2019) 25. URL: `https://doi.org/10.1186/s40824-019-0176-8`.

[7] N. More, G. Kapusetti, Piezoelectric material – A promising approach for bone and cartilage regeneration, Med. Hypotheses 108 (2017) 10–16. URL: `https://doi.org/10.1016/j.mehy.2017.07.021`.

[8] T. Wallmersperger, B. Kröplin, J. Holdenried, R. W. Gülch, A Coupled multi-field-formulation for ionic polymer gels in electric fields, in: SPIE's 8th Annu. Int. Symp. Smart Struct. Mater., 2001, pp. 264–275. URL: `https://doi.org/10.1117/12.432655`.

[9] H. Li, Kinetics of smart hydrogels responding to electric field: A transient deformation analysis, Int. J. Solids Struct. 46 (2009) 1326–1333. URL: `https://doi.org/10.1016/j.ijsolstr.2008.11.001`.

[10] V. C. Mow, A. Ratcliffe, A. Robin Poole, Cartilage and diarthrodial joints as paradigms for hierarchical materials and structures, Biomaterials 13 (1992) 67–97. URL: `https://doi.org/10.1016/0142-9612(92)90001-5`.

[11] H. Jahr, C. Matta, A. Mobasheri, Physicochemical and biomechanical stimuli in cell-based articular cartilage repair, Curr. Rheumatol. Rep. 17 (2015) 22. URL: `https://doi.org/10.1007/s11926-014-0493-9`.

[12] M. De Mattei, A. Pellati, M. Pasello, A. Ongaro, S. Setti, L. Massari, D. Gemmati, A. Caruso, Effects of physical stimulation with electromagnetic field and insulin growth factor-I treatment on proteoglycan synthesis of bovine articular cartilage, Osteoarthr. Cartil. 12 (2004) 793–800. URL: `https://doi.org/10.1016/j.joca.2004.06.012`.

[13] V. C. Mow, C. C. Wang, C. T. Hung, The extracellular matrix, interstitial fluid and ions as a mechanical signal transducer in articular cartilage, Osteoarthr. Cartil. 7 (1999) 41–58. URL: `https://doi.org/10.1053/joca.1998.0161`.

[14] N. P. Cohen, R. J. Foster, V. C. Mow, Composition and dynamics of articular cartilage: Structure, function, and maintaining healthy state, J. Orthop. Sport. Phys. Ther. 28 (1998) 203–215. URL: `https://doi.org/10.2519/jospt.1998.28.4.203`.

[15] A. J. S. Fox, A. Bedi, S. A. Rodeo, The basic science of articular cartilage: structure, composition, and function, Sports Health 1 (2009) 461–468. URL: `https://doi.org/10.1177/1941738109350438`.

[16] R. K. Korhonen, P. Julkunen, J. S. Jurvelin, S. Saarakkala, Structural and compositional changes in peri- and extracellular matrix of osteoarthritic cartilage modulate chondrocyte morphology, Cell. Mol. Bioeng. 4 (2011) 484–494. URL: `https://doi.org/10.1007/s12195-011-0178-7`.

[17] M. A. Brady, S. D. Waldman, C. R. Ethier, The application of multiple biophysical cues to engineer functional neo-cartilage for treatment of osteoarthritis. Part I: Cellular response, Tissue Eng. Part B Rev. 21 (2015) 1–19. URL: `https://doi.org/10.1089/ten.teb.2013.0757`.

[18] V. C. Mow, X. E. Guo, Mechano-electrochemical properties of articular cartilage: their inhomogeneities and anisotropies, Annu. Rev. Biomed. Eng. 4 (2002) 175–209. URL: `https://doi.org/10.1146/annurev.bioeng.4.110701.120309`.

[19] E. H. Frank, A. J. Grodzinsky, Cartilage electromechanics-II. A continuum model of cartilage electrokinetics and correlation with experiments, J. Biomech. 20 (1987) 629–639. URL: `https://doi.org/10.1016/0021-9290(87)90283-1`.

[20] X. Huang, R. Das, A. Patel, T. Duc Nguyen, Physical stimulations for bone and cartilage regeneration, Regen. Eng. Transl. Med. 4 (2018) 216–237. URL: `https://doi.org/10.1007/s40883-018-0064-0`.

[21] V. C. Mow, S. C. Kuei, W. M. Lai, C. G. Armstrong, Biphasic creep and stress relaxation of articular cartilage in compression: Theory and experiments, J. Biomech. Eng. 102 (1980) 73–84. URL: `https://doi.org/10.1115/1.3138202`.

[22] W. M. Lai, V. C. Mow, Drag induced compression of articular cartilage during a permeation experiment, Biorheology 17 (1980) 111–123. URL: `https://doi.org/10.3233/BIR-1980-171-213`.

[23] V. C. Mow, M. C. Gibbs, W. M. Lai, W. B. Zhu, K. A. Athanasiou, Biphasic indentatin of articular cartilage - II. A numerical algorithm and an experimental study, J. Biomech. 22 (1989) 853–861. URL: `https://doi.org/10.1016/0021-9290(89)90069-9`.

[24] W. Wilson, C. C. Van Donkelaar, R. Van Rietbergen, R. Huiskes, The role of computational models in the search for the mechanical behavior and damage mechanisms of articular cartilage, Med. Eng. Phys. 27 (2005) 810–826. URL: `https://doi.org/10.1016/j.medengphy.2005.03.004`.

[25] V. Klika, E. A. Gaffney, Y. C. Chen, C. P. Brown, An overview of multiphase cartilage mechanical modelling and its role in understanding function and pathology, J. Mech. Behav. Biomed. Mater. 62 (2016) 139–157. URL: `https://doi.org/10.1016/j.jmbbm.2016.04.032`.

[26] J. J. Vaca-González, J. M. Guevara, M. A. Moncayo, H. Castro-Abril, Y. A. Hata, D. A. Garzón-Alvarado, Biophysical stimuli: A review of electrical and mechanical stimulation in hyaline cartilage, Cartilage 10 (2019) 157–172. URL: `https://doi.org/10.1177/1947603517730637`.

[27] C. Lee, S. Grad, M. Wimmer, M. Alini, The Influence of mechanical stimuli on articular cartilage tissue engineering, in: N. Ashammakhi, R. Reis (Eds.), Top. Tissue Eng., volume 2, 2006, pp. 1–32. URL: `https://www.oulu.fi/spareparts/ebook_topics_in_t_e_vol2/abstracts/alini_0102.pdf`.

[28] J. A. Panadero, S. Lanceros-Mendez, J. L. G. Ribelles, Differentiation of mesenchymal stem cells for cartilage tissue engineering: Individual and synergetic effects of three-dimensional environment and mechanical loading, Acta Biomater. 33 (2016) 1–12. URL: `https://doi.org/10.1016/j.actbio.2016.01.037`.

[29] G. Ofek, K. A. Athanasiou, Micromechanical properties of chondrocytes and chondrons: relevance to articular cartilage tissue engineering, J. Mech. Mater. Struct. 2 (2007) 1059–1086. URL: `https://doi.org/10.2140/jomms.2007.2.1059`.

[30] L. Bilke, B. Flemisch, T. Kalbacher, O. Kolditz, R. Helmig, T. Nagel, Development of open-source porous media simulators: Principles and experiences, Transp. Porous Media 130 (2019) 337–361. URL: `https://doi.org/10.1007/s11242-019-01310-1`.

[31] J. W. Holmes, Model first and ask Questions Later: Confessions of a reformed experimentalist, J. Biomech. Eng. 141 (2019) 074701. URL: `https://doi.org/10.1115/1.4043432`.

[32] A. S. Hoffman, Hydrogels for biomedical applications âŸĘ, Adv. Drug Deliv. Rev. 64 (2012) 18–23. URL: `https://doi.org/10.1016/j.addr.2012.09.010`.

[33] S. Fuchs, K. Shariati, M. Ma, Specialty tough hydrogels and their biomedical applications, Adv. Healthc. Mater. 9 (2020) 1901396. URL: `https://doi.org/10.1002/adhm.201901396`.

[34] L. Hu, Y. Wan, Q. Zhang, M. J. Serpe, Harnessing the power of stimuli-responsive polymers for actuation, Adv. Funct. Mater. 30 (2020) 1903471. URL: `https://doi.org/10.1002/adfm.201903471`.

[35] A. R. D. Bakhshayesh, N. Asadi, A. Alihemmati, H. T. Nasrabadi, A. Montaseri, S. Davaran, S. Saghati, A. Akbarzadeh, A. Abedelahi, An overview of advanced biocompatible and biomimetic materials for creation of replacement structures in the musculoskeletal systems: Focusing on cartilage

tissue, J. Biol. Eng. 13 (2019) 1–21. URL: `https://doi.org/10.1186/s13036-019-0209-9`.

[36] C. Ning, Z. Zhou, G. Tan, Y. Zhu, C. Mao, Electroactive polymers for tissue regeneration: Developments and perspectives, Prog. Polym. Sci. 81 (2018) 144–162. URL: `https://doi.org/10.1016/j.progpolymsci.2018.01.001`.

[37] K. L. Spiller, S. A. Maher, A. M. Lowman, Hydrogels for the repair of articular cartilage defects, Tissue Eng. Part B Rev. 17 (2011) 281–299. URL: `https://doi.org/10.1089/ten.teb.2011.0077`.

[38] Y. Krishnan, A. J. Grodzinsky, Cartilage diseases, Matrix Biol. 71-72 (2018) 51–69. URL: `https://doi.org/10.1016/j.matbio.2018.05.005`.

[39] K. A. Athanasiou, E. M. Darling, G. D. DuRaine, J. C. Hu, A. H. Reddi, Articular cartilage, CRC Press, Boca Raton, 2017. URL: `https://doi.org/10.1017/CBO9781107415324.004`.

[40] A. Getgood, T. Bhullar, N. Rushton, Current concepts in articular cartilage repair, Orthop. Trauma 23 (2009) 189–200. URL: `https://doi.org/10.1016/j.mporth.2009.05.002`.

[41] J. A. Buckwalter, E. B. Hunziker, L. C. Rosenberg, R. Coutts, M. Adams, D. Eyre, Articular cartilage: composition and structure, in: S. L. Woo, J. A. Buckwalter (Eds.), Injury and repair of the musculoskeletal soft tissue, American Academy of Orthopaedic Surgeons, Park Ridge, 1991, pp. 405–425.

[42] V. C. Mow, A. Ratcliffe, Structure and function of articular cartilage and meniscus, in: V. C. Mow, W. C. Hayes (Eds.), Basic Orthop. Biomech., Lippincott-Raven, Philadelphia, 1997, pp. 113–177.

[43] J. P. Halloran, S. C. Sibole, C. C. Van Donkelaar, M. C. Van Turnhout, C. W. J. Oomens, J. A. Weiss, F. Guilak, A. Erdemir, Multiscale mechanics of articular cartilage: Potentials and challenges of coupling musculoskeletal, joint, and microscale computational models, Ann. Biomed. Eng. 40 (2012) 2456–2474. URL: `https://doi.org/10.1007/s10439-012-0598-0`.

[44] A. Erdemir, C. Bennetts, S. Davis, A. Reddy, S. C. Sibole, Multiscale cartilage biomechanics: technical challenges in realizing a high-throughput modelling and simulation workflow, Interface Focus 5 (2015) 1–14. URL: `https://doi.org/10.1098/rsfs.2014.0081`.

[45] H. J. Samvelyan, D. Hughes, C. Stevens, K. A. Staines, Models of osteoarthritis: Relevance and new insights, Calcif. Tissue Int. 2020, Accepted (2020). URL: `https://doi.org/10.1007/s00223-020-00670-x`.

[46] B. Johnstone, M. J. Stoddart, G. I. Im, Multi-disciplinary approaches for cell-based cartilage regeneration, J. Orthop. Res. 38 (2020) 463–472. URL: `https://doi.org/10.1002/jor.24458`.

[47] L. C. Biant, M. J. McNicholas, Current surgical options for the treatment of symptomatic articular cartilage lesions of the knee, Orthop. Trauma 33 (2019) 127–132. URL: `https://doi.org/10.1016/j.mporth.2019.01.008`.

[48] R. E. Outerbridge, The etiology of chondromalacia patellae, J. Bone Jt. Surg. 43B (1961) 752–757. URL: `https://doi.org/10.1302/0301-620X.43B4.752`.

[49] W. Widuchowski, J. Widuchowski, T. Trzaska, Articular cartilage defects: Study of 25,124 knee arthroscopies, Knee 14 (2007) 177–182. URL: `https://doi.org/10.1016/j.knee.2007.02.001`.

[50] W. Wilson, J. M. Huyghe, C. C. van Donkelaar, A composition-based cartilage model for the assessment of compositional changes during cartilage damage and adaptation, Osteoarthr. Cartil. 14 (2006) 554–560. URL: `https://doi.org/10.1016/j.joca.2005.12.006`.

[51] P. Julkunen, W. Wilson, J. S. Jurvelin, R. K. Korhonen, Composition of the pericellular matrix modulates the deformation behaviour of chondrocytes in articular cartilage under static loading, Med. Biol. Eng. Comput. 47 (2009) 1281–1290. URL: `https://doi.org/10.1007/s11517-009-0547-8`.

[52] R. K. Korhonen, W. Herzog, Depth-dependent analysis of the role of collagen fibrils, fixed charges and fluid in the pericellular matrix of articular cartilage on chondrocyte mechanics, J. Biomech. 41 (2008) 480–485. URL: `https://doi.org/10.1016/j.jbiomech.2007.09.002`.

[53] R. K. Korhonen, P. Julkunen, W. Wilson, W. Herzog, Importance of collagen orientation and depth-dependent fixed charge densities of cartilage on mechanical behavior of chondrocytes, J. Biomech. Eng. 130 (2008) 1–11. URL: `https://doi.org/10.1115/1.2898725`.

[54] R. Shirazi, A. Shirazi-Adl, Deep vertical collagen fibrils play a significant role in mechanics of articular cartilage, J. Orthop. Res. 26 (2008) 608–615. URL: `https://doi.org/10.1002/jor.20537`.

[55] F. Vannini, T. Spalding, L. Andriolo, M. Berruto, M. Denti, J. Espregueira-Mendes, J. Menetrey, G. M. Peretti, R. Seil, G. Filardo, Sport and early osteoarthritis: the role of sport in aetiology, progression and treatment of knee osteoarthritis, Knee Surgery, Sport. Traumatol. Arthrosc. 24 (2016) 1786–1796. URL: `https://doi.org/10.1007/s00167-016-4090-5`.

[56] W. Meng, L. Gao, J. K. Venkatesan, G. Wang, H. Madry, Translational applications of photopolymerizable hydrogels for cartilage repair, J. Exp. Orthop. 6 (2019) 47. URL: `https://doi.org/10.1186/s40634-019-0215-3`.

[57] J. R. Steadman, W. G. Rodkey, S. B. Singleton, K. K. Briggs, Microfracture technique for full-thickness chondral defects: Technique and clinical results, Oper. Tech. Orthop. 7 (1997) 300–304. URL: `https://doi.org/10.1016/S1048-6666(97)80033-X`.

[58] A. M. Bhosale, J. B. Richardson, Articular cartilage: Structure, injuries and review of management, Br. Med. Bull. 87 (2008) 77–95. URL: `https://doi.org/10.1093/bmb/ldn025`.

[59] J. S. Temenoff, A. G. Mikos, Review: tissue engineering for regeneration of articular cartilage, Biomaterials 21 (2000) 431–440. URL: `https://doi.org/10.1016/S0142-9612(99)00213-6`.

[60] L. Hangody, G. Kish, Z. Kárpáti, I. Szerb, I. Udvarhelyi, Arthroscopic autogenous osteochondral mosaicplasty for the treatment of femoral condylar articular defects: A preliminary report, Knee Surgery, Sport. Traumatol. Arthrosc. 5 (1997) 262–267. URL: `https://doi.org/10.1007/s001670050061`.

[61] J. Becerra, J. A. Andrades, E. Guerado, P. Zamora-Navas, J. M. López-Puertas, A. H. Reddi, Articular cartilage: Structure and regeneration, Tissue Eng. - Part B Rev. 16 (2010) 617–627. URL: `https://doi.org/10.1089/ten.teb.2010.0191`.

[62] C. Mina, W. E. Garrett, R. Pietrobon, R. Glisson, L. Higgins, High tibial osteotomy for unloading osteochondral defects in the medial compartment of the knee, Am. J. Sports Med. 36 (2008) 949–955. URL: `https://doi.org/10.1177/0363546508315471`.

[63] T. A. E. Ahmed, M. T. Hincke, Strategies for articular cartilage lesion repair and functional restoration, Tissue Eng. Part B Rev. 16 (2010) 305–29. URL: `https://doi.org/10.1089/ten.TEB.2009.0590`.

[64] C. M. Revell, K. A. Athanasiou, Success rates and immunologic responses of autogenic, allogenic, and xenogenic treatments to repair articular cartilage defects, Tissue Eng. Part B Rev. 15 (2009) 1–15. URL: `https://doi.org/10.1089/ten.teb.2008.0189`.

[65] S. L. Sherman, J. Garrity, K. Bauer, J. Cook, J. Stannard, W. D. Bugbee, Fresh Osteochondral Allograft Transplantation for Fractures of the Knee, J Am Acad Orthop Surg 22 (2014) 121–133. URL: `https://doi.org/10.1177/1947603516657640`.

[66] J. P. Benthien, P. Behrens, The treatment of chondral and osteochondral defects of the knee with autologous matrix-induced chondrogenesis (AMIC): Method description and recent developments, Knee Surgery, Sport. Traumatol. Arthrosc. 19 (2011) 1316–1319. URL: `https://doi.org/10.1007/s00167-010-1356-1`.

[67] P. Behrens, Matrixgekoppelte Mikrofrakturierung. Ein neues Konzept zur Knorpeldefektbehandlung, Arthroskopie 18 (2005) 193–197. URL: `https://doi.org/10.1007/s00142-005-0316-0`.

[68] J. M. Oliveira, R. L. Reis (Eds.), Regenerative Strategies for the Treatment of Knee Joint Disabilities, volume 21 of *Studies in Mechanobiology, Tissue Engineering and Biomaterials*, Springer, 2017. URL: `https://doi.org/10.1007/978-3-319-44785-8`.

[69] J. Gille, E. Schuseil, J. Wimmer, J. Gellissen, A. P. Schulz, P. Behrens, Mid-term results of Autologous Matrix-Induced Chondrogenesis for treatment of focal cartilage defects in the knee, Knee Surgery, Sport. Traumatol. Arthrosc. 18 (2010) 1456–1464. URL: `https://doi.org/10.1007/s00167-010-1042-3`.

[70] J. Gille, P. Behrens, P. Volpi, L. De Girolamo, E. Reiss, W. Zoch, S. Anders, Outcome of autologous matrix induced chondrogenesis (AMIC) in cartilage knee surgery: Data of the AMIC registry, Arch. Orthop. Trauma Surg. 133 (2013) 87–93. URL: `https://doi.org/10.1007/s00402-012-1621-5`.

[71] T. Kusano, R. P. Jakob, E. Gautier, R. A. Magnussen, H. Hoogewoud, M. Jacobi, Treatment of isolated chondral and osteochondral defects in the knee by autologous matrix-induced chondrogenesis (AMIC), Knee Surgery, Sport. Traumatol. Arthrosc. 20 (2012) 2109–2115. URL: `https://doi.org/10.1007/s00167-011-1840-2`.

[72] T. Dvir, B. P. Timko, D. S. Kohane, R. Langer, Nanotechnological strategies for engineering complex tissues, Nat. Nanotechnol. 6 (2011) 13–22. URL: `10.1038/nnano.2010.246`.

[73] F. H. Chen, K. T. Rousche, R. S. Tuan, Technology insight: Adult stem cells in cartilage regeneration and tissue engineering, Nat. Clin. Pract. Rheumatol. 2 (2006) 373–382. URL: `https://doi.org/10.1038/ncprheum0216`.

[74] C. Madeira, A. Santhagunam, J. B. Salgueiro, J. Cabral, Advanced cell therapies for articular cartilage regeneration, Trends Biotechnol. 33 (2015) 35–42. URL: `https://doi.org/10.1016/j.tibtech.2014.11.003`.

[75] D. A. Grande, M. I. Pitman, L. Peterson, D. Menche, M. Klein, The repair of experimentally produced defects in rabbit articular cartilage by autologous chondrocyte transplantation, J. Orthop. Res. 7 (1989) 208–218. URL: `https://doi.org/10.1002/jor.1100070208`.

[76] M. Brittberg, A. Lindahl, A. Nilsson, C. Ohlsson, O. Isaksson, L. Peterson, Treatment of deep cartilage defects in the knee with autologous chondrocyte transplantation, N. Engl. J. Med. 331 (1994) 889–895. URL: `https://doi.org/10.1056/NEJM199410273311701`.

[77] H. S. Vasiliadis, J. Wasiak, G. Salanti, Autologous chondrocyte implantation for the treatment of cartilage lesions of the knee: A systematic review of randomized studies, Knee Surgery, Sport. Traumatol. Arthrosc. 18 (2010) 1645–1655. URL: `https://doi.org/10.1007/s00167-010-1050-3`.

[78] L. Peterson, H. S. Vasiliadis, M. Brittberg, A. Lindahl, Autologous chondrocyte implantation: A long-term follow-up, Am. J. Sports Med. 38 (2010) 1117–1124. URL: `https://doi.org/10.1177/0363546509357915`.

[79] E. A. Makris, A. H. Gomoll, K. N. Malizos, J. C. Hu, K. A. Athanasiou, Repair and tissue engineering techniques for articular cartilage, Nat. Rev. Rheumatol. 11 (2015) 21–34. URL: `https://doi.org/10.1038/nrrheum.2014.157`.

[80] W. Bartlett, J. A. Skinner, C. R. Gooding, R. W. Carrington, A. M. Flanagan, T. W. Briggs, G. Bentley, Autologous chondrocyte implantation versus matrix-induced autologous chondrocyte implantation for osteochondral defects of the knee. A prospective, randomised study, J. Bone Jt. Surg. - Ser. B 87 (2005) 640–645. URL: `10.1302/0301-620X.87B5.15905`.

[81] M. H. Zheng, C. Willers, L. Kirilak, P. Yates, J. Xu, D. Wood, A. Shimmin, Matrix-Induced Autologous Chondrocyte Implantation (MACI®): Biological and histological assessment, Tissue Eng. 13 (2007) 737–746. URL: `https://doi.org/10.1089/ten.2006.0246`.

[82] B. S. Dunkin, C. Lattermann, New and emerging techniques in cartilage repair: Matrix-induced autologous chondrocyte implantation, Oper. Tech. Sports Med. 21 (2013) 100–107. URL: `https://doi.org/10.1053/j.otsm.2013.03.003`.

[83] D. Saris, A. Price, W. Widuchowski, M. Bertrand-Marchand, J. Caron, J. O. Drogset, P. Emans, A. Podskubka, A. Tsuchida, S. Kili, D. Levine, M. Brittberg, Matrix-applied characterized autologous cultured chondrocytes versus microfracture: Two-year follow-up of a prospective randomized trial, Am. J. Sports Med. 42 (2014) 1384–1394. URL: `https://doi.org/10.1177/0363546514528093`.

[84] M. Brittberg, D. Recker, J. Ilgenfritz, D. B. Saris, Matrix-applied characterized autologous cultured chondrocytes versus microfracture: Five-year follow-up of a prospective randomized trial, Am. J. Sports Med. 46 (2018) 1343–1351. URL: `https://doi.org/10.1177/0363546518756976`.

[85] B. B. Hinckel, A. H. Gomoll, J. Farr, Cartilage restoration in the patellofemoral joint, Am. J. Orthop. 46 (2017) 217–222. URL: `https://doi.org/10.1016/j.otsm.2019.150692`.

[86] J. Farr, B. J. Cole, S. Sherman, V. Karas, Particulated articular cartilage: CAIS and DeNovo NT, J. Knee Surg. 25 (2012) 23–29. URL: `https://doi.org/10.1055/s-0031-1299652`.

[87] J. Ackermann, B. J. Cole, A. H. Gomoll, Cartilage restoration in the patellofemoral Joint: Techniques and outcomes, Oper. Tech. Sports Med. 27 (2019) 150692. URL: `10.1016/j.otsm.2019.150692`.

[88] J. J. Felder, C. Lattermann, Advances and current concepts of cartilage repair in the patellofemoral joint, Oper. Tech. Sports Med. 23 (2015) 143–149. URL: `https://doi.org/10.1053/j.otsm.2015.02.004`.

[89] D. L. Richter, R. C. Schenck, D. C. Wascher, G. Treme, Knee articular cartilage repair and restoration techniques: A review of the literature, Sports Health 8 (2016) 153–160. URL: `https://doi.org/10.1177/1941738115611350`.

[90] M. Tompkins, J. C. Hamann, D. R. Diduch, K. F. Bonner, J. M. Hart, F. W. Gwathmey, M. D. Milewski, C. M. Gaskin, Preliminary results of a novel single-stage cartilage restoration technique: Particulated juvenile articular cartilage allograft for chondral defects of the patella, Arthrosc. - J. Arthrosc. Relat. Surg. 29 (2013) 1661–1670. URL: `https://doi.org/10.1016/j.arthro.2013.05.021`.

[91] G. Filardo, E. Kon, A. Roffi, A. Di Martino, M. Marcacci, Scaffold-based repair for cartilage healing: A systematic review and technical note, Arthrosc. - J. Arthrosc. Relat. Surg. 29 (2013) 174–186. URL: `https://doi.org/10.1016/j.arthro.2012.05.891`.

[92] J.-H. Lee, H.-W. Kim, Emerging properties of hydrogels in tissue engineering, J. Tissue Eng. 9 (2018) 1–4. URL: `https://doi.org/10.1177/2041731418768285`.

[93] H. J. Kwon, Tissue engineering of muscles and cartilages using polyelectrolyte hydrogels, Adv. Mater. Sci. Eng. 2014 (2014) 154071. URL: `https://doi.org/10.1155/2014/154071`.

[94] E.-Y. Chuang, C.-W. Chiang, P.-C. Wong, C.-H. Chen, Hydrogels for the application of articular cartilage tissue engineering: A review of hydrogels, Adv. Mater. Sci. Eng. 2018 (2018) 4368910. URL: `https://doi.org/10.1155/2018/4368910`.

[95] S. L. Vega, M. Y. Kwon, J. A. Burdick, Recent advances in hydrogels for cartilage tissue engineering, Eur. Cells Mater. 33 (2017) 59–75. URL: `https://doi.org/10.22203/eCM.v033a05`.

[96] J. Yang, Y. S. Zhang, K. Yue, A. Khademhosseini, Cell-laden hydrogels for osteochondral and cartilage tissue engineering, Acta Biomater. 57 (2017) 1–25. URL: `https://doi.org/10.1016/j.actbio.2017.01.036`.

[97] D. A. Sánchez-Téllez, L. Téllez-Jurado, L. M. Rodríguez-Lorenzo, Hydrogels for cartilage regeneration, from polysaccharides to hybrids, Polymers (Basel). 9 (2017) 671. URL: `https://doi.org/10.3390/polym9120671`.

[98] H. Yuk, B. Lu, X. Zhao, Hydrogel bioelectronics, Chem. Soc. Rev. 48 (2019) 1642–1667. URL: `https://doi.org/10.1039/c8cs00595h`.

[99] E. A. Aisenbrey, S. J. Bryant, The role of chondroitin sulfate in regulating hypertrophy during MSC chondrogenesis in a cartilage mimetic hydrogel under dynamic loading, Biomaterials 190-191 (2019) 51–62. URL: `10.1016/j.biomaterials.2018.10.028`.

[100] S. G. Walter, R. Ossendorff, F. A. Schildberg, Articular cartilage regeneration and tissue engineering models: a systematic review, Arch. Orthop. Trauma Surg. 139 (2019) 305–316. URL: `https://doi.org/10.1007/s00402-018-3057-z`.

[101] J. Fu, P. He, D.-A. Wang, Articular cartilage tissue engineering, in: A. Hasan (Ed.), Tissue engineering for artificial organs: Regenerative medicine, smart diagnostics and personalized medicine, volume 1, Wiley Online Library, 2017, pp. 243–295. URL: `https://doi.org/10.1002/9783527689934.ch8`.

[102] E. Y. Salinas, J. C. Hu, K. A. Athanasiou, A guide for using mechanical stimulation to enhance tissue-engineered articular cartilage properties, Tissue Eng. Part B Rev. 24 (2018) 345–358. URL: `https://doi.org/10.1089/ten.teb.2018.0006`.

[103] A. R. Farooqi, R. Bader, U. van Rienen, Numerical study on electromechanics in cartilage tissue with respect to its electrical properties, Tissue Eng. Part B Rev. 25 (2019) 152–166. URL: `https://doi.org/10.1089/ten.teb.2018.0214`.

[104] M. A. Brady, S. D. Waldman, C. R. Ethier, The application of multiple biophysical cues to engineer functional neocartilage for treatment of osteoarthritis. Part II: Signal transduction, Tissue Eng. Part B Rev. 21 (2015) 20–33. URL: `https://doi.org/10.1089/ten.teb.2013.0760`.

[105] K. Iwasa, A. H. Reddi, Pulsed electromagnetic fields and tissue engineering of the joints, Tissue Eng. Part B Rev. 24 (2018) 144–154. URL: `https://doi.org/10.1089/ten.teb.2017.0294`.

[106] M. Fini, S. Pagani, G. Giavaresi, M. De Mattei, A. Ongaro, K. Varani, F. Vincenzi, L. Massari, M. Cadossi, Functional tissue engineering in articular cartilage repair: Is there a role for electromagnetic biophysical stimulation?, Tissue Eng. Part B Rev. 19 (2013) 353–367. URL: `https://doi.org/10.1089/ten.TEB.2012.0501`.

[107] R. H. W. Funk, T. Monsees, N. Özkucur, Electromagnetic effects - From cell biology to medicine, Prog. Histochem. Cytochem. 43 (2009) 177–264. URL: `https://doi.org/10.1016/j.proghi.2008.07.001`.

[108] L. P. da Silva, S. C. Kundu, R. L. Reis, V. M. Correlo, Electric phenomenon: A disregarded tool in tissue engineering and regenerative medicine, Trends Biotechnol. 38 (2020) 24–49. URL: `https://doi.org/10.1016/j.tibtech.2019.07.002`.

[109] D. R. Merrill, M. Bikson, J. G. Jefferys, Electrical stimulation of excitable tissue: Design of efficacious and safe protocols, J. Neurosci. Methods 141 (2005) 171–198. URL: `https://doi.org/10.1016/j.jneumeth.2004.10.020`.

[110] S. Meng, M. Rouabhia, Z. Zhang, Electrical stimulation in tissue regeneration, in: G. D. Gargiulo, A. McEwan (Eds.), Applied Biomedical Engineering, IntechOpen, Rijeka, 2011, pp. 37–62. URL: `https://doi.org/10.5772/18874`.

[111] C. T. Brighton, W. Wang, R. Seldes, G. Zhang, S. R. Pollack, Signal transduction in electrically stimulated bone cells, J. Bone Jt. Surg. 83 (2001) 1514–1523. URL: `https://doi.org/10.2106/00004623-200110000-00009`.

[112] N. Szasz, Electric field regulation of chondrocyte proliferation, biosynthesis, and cellular signaling, Ph.D. thesis, Massachusetts Institute of Technology, 2003.

[113] T. Rylander, P. Ingelstrom, A. Bondeson, Computational electromagnetics, 2nd ed., Springer, 2013. URL: `https://doi.org/10.1007/978-1-4419-7646-8`.

[114] J. C. Maxwell, A Treatise On Electricity and Magnetism, 3 ed., Dover Publications, New York, 1954.

[115] U. van Rienen, Numerical methods in computational electrodynamics_Linear systems in practical applications, 1 ed., Springer-Verlag, Berlin, Heidelberg, 2001. URL: `https://doi.org/10.1007/978-3-642-56802-2`.

[116] M. G. Larson, F. Bengzon, The finite element method: theory, implementation, and applications, volume 10, Springer Science & Business Media, 2013. URL: `https://doi.org/10.1007/978-3-642-33287-6`.

[117] J. Fish, T. Belytschko, A First Course in Finite Elements, John Wiley & Sons, 2007. URL: `https://doi.org/10.1002/9780470510858`.

[118] A. Logg, K.-A. Mardal, G. N. Wells, Automated solution of differential equations by the finite element method_The FEniCS book, Springer-Verlag, Berlin, Heidelberg, 2012. URL: `https://doi.org/10.1007/978-3-642-23099-8`.

[119] M. S. Alnæs, J. Blechta, J. Hake, A. Johansson, B. Kehlet, A. Logg, C. Richardson, J. Ring, E. Rognes, G. N. Wells, The FEniCS project version 1.5, Arch. Numer. Softw. 3 (2015) 9–23. URL: `https://doi.org/10.11588/ans.2015.100.20553`.

[120] L. Scott, Introduction to automated modeling with FEniCS, Computational Modeling Initiative LLC, 2018. URL: `https://dl.acm.org/doi/book/10.5555/3265509`.

[121] B. D. Arnold, A. Logg, Periodic Table of the Elements, SIAM News 47 (2014) 9.

[122] H. P. Langtangen, K.-A. Mardal, Introduction to numerical methods for variational problems, Texts in Computational Science and Engineering, 1 ed., Springer International Publishing, Switzerland, 2019. URL: `https://doi.org/10.1007/978-3-030-23788-2`.

[123] B. Baker, J. Spadaro, A. Marino, R. O. Backer, Electrical stimulation of articular cartilage regeneration, Ann. New York Acad. Sci. 238 (1974) 491–499. URL: `https://doi.org/10.1111/j.1749-6632.1974.tb26815.x`.

[124] B. Baker, R. O. Becker, J. Spadaro, A study of electrochemical enhancement of articular cartilage repair, Clin. Orthop. Relat. Res. 102 (1974) 251–267. URL: `https://doi.org/10.1097/00003086-197407000-00029`.

[125] L. Lippiello, D. Chakkalakal, J. F. Connolly, Pulsing direct current-induced repair of articular cartilage in rabbit osteochondral defects, J. Orthop. Res. 8 (1990) 266–275. URL: `https://doi.org/10.1002/jor.1100080216`.

[126] E. H. Frank, A. Grodzinsky, Cartilage electromechanics-I. Electrokinetic transduction and the effects of electrolyte pH and ionic strength, J. Biomech. 20 (1987) 615–627. URL: `https://doi.org/10.1016/0021-9290(87)90282-X`.

[127] S. I. Berkenblit, E. H. Frank, E. P. Salant, A. J. Grodzinsky, Nondestructive detection of cartilage degeneration using electromechanical surface spectroscopy, J. Biomech. Eng. 116 (1994) 384–392. URL: `https://doi.org/10.1115/1.2895788`.

[128] T. Akkin, D. P. Davé, J.-I. Youn, S. A. Telenkov, H. G. Rylander, T. E. Milner, Imaging tissue response to electrical and photothermal stimulation with nanometer sensitivity, Lasers Surg. Med. 33 (2003) 219–225. URL: `https://doi.org/10.1002/lsm.10221`.

[129] J.-I. Youn, T. Akkin, T. E. Milner, Electrokinetic measurement of cartilage using differential phase optical coherence tomography, Physiol. Meas. 25 (2004) 85–95. URL: `https://doi.org/10.1088/0967-3334/25/1/008`.

[130] M. L. Gray, Physical regulation of epiphysical cartilage biosynthesis: Responses to electrical, mechanical and chemical signals, Ph.D. thesis, Massachusetts Institute of Technology, 1986.

[131] L. A. MacGinitie, Electrical and thermal modulation of protein synthesis in cartilage: A model for field effects on biological tissues, Ph.D. thesis, Massachusetts Institute of Technology, 1987.

[132] L. A. MacGinitie, A. J. Grodzinsky, E. H. Frank, Y. A. Gluzband, Frequency and amplitude dependence of electric field interactions: Electrokinetics and biosynthesis, in: M. Blank, E. Findl (Eds.), Mechanistic Approaches to Interactions of Electric and Electromagnetic Fields with Living Systems, Springer, Boston, MA, USA, 1987, pp. 133–149. URL: `https://doi.org/10.1007/978-1-4899-1968-7_8`.

[133] L. A. MacGinitie, Y. A. Gluzband, A. J. Grodzinsky, Electric field stimulation can increase protein synthesis in articular cartilage explants, J. Orthop. Res. 12 (1994) 151–160. URL: `https://doi.org/10.1002/jor.1100120202`.

[134] H. Nogami, H. Aoki, T. Okagawa, K. Mimatsu, Effects of electric current on chondrogenesis in vitro, Clin. Orthop. Relat. Res. 163 (1982) 243–247.

[135] P. H. Chao, R. Roy, R. L. Mauck, W. Liu, W. B. Valhmu, C. T. Hung, Chondrocyte translocation response to direct current electric fields., J. Biomech. Eng. 122 (2000) 261–267. URL: `https://doi.org/10.1115/1.429661`.

[136] O. O. Akanji, D. A. Lee, D. A. Bader, The effects of direct current stimulation on isolated chondrocytes seeded in 3D agarose constructs, Biorheology 45 (2008) 229–243. URL: `https://doi.org/10.3233/BIR-2008-0473`.

[137] H. J. Kwon, G. S. Lee, H. Chun, Electrical stimulation drives chondrogenesis of mesenchymal stem cells in the absence of exogenous growth factors, Sci. Rep. 6 (2016) 39302. URL: `https://doi.org/10.1038/srep39302`.

[138] B. Hiemer, M. Krogull, T. Bender, J. Ziebart, S. Krueger, R. Bader, A. Jonitz-Heincke, Effect of electric stimulation on human chondrocytes and mesenchymal stem cells under normoxia and hypoxia, Mol. Med. Rep. 18 (2018) 2133–2141. URL: `https://doi.org/10.3892/mmr.2018.9174`.

[139] J. Farr, M. A. Mont, J. R. Caldwell, D. Garland, T. M. Zizic, Pulsed electrical stimulation in patients with osteoarthritis of the knee: Follow up in 288 patients who had failed non-operative therapy, Surg. Technol. Int. 15 (2006) 227–233.

[140] D. Garland, P. A. Holt, J. T. Harrington, J. R. Caldwell, T. M. Zizic, J. Cholewczynski, A 3-month, randomized, double-blind, placebo-controlled study to evaluate the safety and efficacy of a highly optimized, capacitively coupled, pulsed electrical stimulator in patients with osteoarthritis of the knee, Osteoarthr. Cartil. 15 (2007) 630–637. URL: `https://doi.org/10.1016/j.joca.2007.01.004`.

[141] G. A. Rodan, L. A. Bourret, L. A. Norton, DNA synthesis in cartilage cells is stimulated by oscillating electric fields., Science (80-.). 199 (1978) 690–692. URL: `https://doi.org/10.1126/science.625660`.

[142] R. J. Fitzsimmons, S. L. Gordon, J. Kronberg, T. Ganey, A. A. Pilla, A pulsing electric field (PEF) increases human chondrocyte proliferation through a transduction pathway involving nitric oxide signaling, J. Orthop. Res. 26 (2008) 854–859. URL: `https://doi.org/10.1002/jor.20590`.

[143] E. Esfandiari, S. Roshankhah, M. Mardani, B. Hashemibeni, E. Naghsh, M. Kazemi, M. Salahshoor, The effect of high frequency electric field on enhancement of chondrogenesis in human adipose-derived stem cells, Iran. J.

Basic Med. Sci. 17 (2014) 571–576. URL: `https://doi.org/10.22038/IJBMS.2014.3188`.

[144] M. Mardani, S. Roshankhah, B. Hashemibeni, M. Salahshoor, E. Naghsh, E. Esfandiari, Induction of chondrogenic differentiation of human adipose-derived stem cells by low frequency electric field, Adv. Biomed. Res. 5 (2016) 97. URL: `https://doi.org/10.4103/2277-9175.183146`.

[145] C. T. Brighton, A. S. Unger, J. L. Stambough, In vitro growth of bovine articular cartilage chondrocytes in various capacitively coupled electrical fields, J. Orthop. Res. 2 (1984) 15–22. URL: `https://doi.org/10.1002/jor.1100020104`.

[146] W. Wang, Z. Wang, G. Zhang, C. C. Clark, C. T. Brighton, Up-regulation of chondrocyte matrix genes and products by electric fields, Clin. Orthop. Relat. Res. 427 (2004) S163–S173. URL: `https://doi.org/10.1097/01.blo.0000143837.53434.5c`.

[147] C. T. Brighton, W. Wang, C. C. Clark, Up-regulation of matrix in bovine articular cartilage explants by electric fields, Biochem. Biophys. Res. Commun. 342 (2006) 556–561. URL: `https://doi.org/10.1016/j.bbrc.2006.01.171`.

[148] C. T. Brighton, W. Wang, C. C. Clark, The effect of electrical fields on gene and protein expression in human osteoarthritic cartilage explants., J. Bone Jt. Surg. 90 (2008) 833–848. URL: `https://doi.org/10.2106/JBJS.F.01437`.

[149] J. Xu, W. Wang, C. C. Clark, C. T. Brighton, Signal transduction in electrically stimulated articular chondrocytes involves translocation of extracellular calcium through voltage-gated channels, Osteoarthr. Cartil. 17 (2009) 397–405. URL: `https://doi.org/10.1016/j.joca.2008.07.001`.

[150] C. T. Brighton, W. Wang, C. C. Clark, A. Praestgaard, A spectrophotometric analysis of human osteoarthritic cartilage explants subjected to specific capacitively coupled electric fields, Open J. Biophys. 3 (2013) 158–164. URL: `https://doi.org/10.4236/ojbiphy.2013.32019`.

[151] M. L. Hernández-Bule, C. L. Paíno, M. Á. Trillo, A. Úbeda, Electric stimulation at 448 kHz promotes proliferation of human mesenchymal stem cells, Cell. Physiol. Biochem. 34 (2014) 1741–1755. URL: `https://doi.org/10.1159/000366375`.

[152] J. J. Vaca-González, J. M. Guevara, J. F. Vega, D. A. Garzón-Alvarado, An in Vitro chondrocyte electrical stimulation framework: A methodology to calculate electric fields and modulate proliferation, cell death and glycosaminoglycan synthesis, Cell. Mol. Bioeng. 9 (2016) 116–126. URL: `https://doi.org/10.1007/s12195-015-0419-2`.

[153] J. J. Vaca-González, J. F. Escobar, J. M. Guevara, Y. A. Hata, G. Gallego Ferrer, D. A. Garzón-Alvarado, Capacitively coupled electrical stimulation of rat chondroepiphysis explants: A histomorphometric analysis, Bioelectrochemistry 126 (2019) 1–11. URL: `https://doi.org/10.1016/j.bioelechem.2018.11.004`.

[154] J. J. Vaca-González, The effect of electric fields on hyaline cartilage: An in vitro and in silico study, Ph.D. thesis, Universidad Nacional de Colombia and Universitat Politècnica de València, 2019. URL: `https://doi.org/10.4995/Thesis/10251/120023`.

[155] B. R. Simon, Multiphase poroelastic finite element models for soft tissue structures, Appl. Mech. Rev. 45 (1992) 191–218. URL: `https://doi.org/10.1115/1.3121397`.

[156] A. F. T. Mak, The apparent viscoelastic behavior of articular cartilage - The contributions from the intrinsic matrix viscoelasticity and interstitial fluid flows, J. Biomech. Eng. 108 (1986) 123–130. URL: `https://doi.org/10.1115/1.3138591`.

[157] T. D. Nguyen, Y. Gu, A. Oloyede, W. Senadeera, Analysis of strain-rate dependent mechanical behavior of single chondrocyte: a finite element study, Int. J. Comput. Methods 11 (2014) 1344005. URL: `https://doi.org/10.1142/S0219876213440052`.

[158] W. M. Lai, J. S. Hou, V. C. Mow, A triphasic theory for the swelling and deformation behaviors of articular cartilage, J. Biomech. Eng. 113 (1991) 245–258. URL: `https://doi.org/10.1115/1.2894880`.

[159] J. M. Huyghe, J. D. Janssen, Quadriphasic mechanics of swelling incompressible porous media, Int. J. Eng. Sci. 35 (1997) 793–802. URL: `https://doi.org/10.1016/S0020-7225(96)00119-X`.

[160] W. Y. Gu, W. M. Lai, V. C. Mow, A mixture theory for charged-hydrated soft tissues containing multi-electrolytes: Passive transport and swelling Behaviors,

J. Biomech. Eng. 120 (1998) 169–180. URL: `https://doi.org/10.1115/1.2798299`.

[161] V. C. Mow, W. M. Lai, Recent Developments in synovial joint biomechanics, SIAM Rev. 22 (1980) 275–317. URL: `https://doi.org/10.1137/1022056`.

[162] W. M. Lai, V. C. Mow, D. D. Sun, G. A. Ateshian, On the electric potentials inside a charged soft hydrated biological tissue: Streaming potential versus diffusion potential, J. Biomech. Eng. 122 (2000) 336–346. URL: `https://doi.org/10.1115/1.1286316`.

[163] W. Y. Gu, W. M. Lai, V. C. Mow, Transport of multi-electrolytes in charged hydrated biological soft tissues, Transp. Porous Media 34 (1999) 143–157. URL: `https://doi.org/10.1023/A:1006561408186`.

[164] A. Maroudas, C. Bannon, Measurement of swelling pressure in cartilage and comparison with the osmotic pressure of constituent proteoglycans, Biorheology 18 (1981) 619–632. URL: `https://doi.org/10.3233/BIR-1981-183-624`.

[165] L. Onsager, Reciprocal relations in irreversible processes. I., Phys. Rev. 37 (1931) 405–426. URL: `https://doi.org/10.1103/PhysRev.37.405`.

[166] L. Onsager, Reciprocal relations in irreversible processes. II., Phys. Rev. 38 (1931) 2265–2279. URL: `https://doi.org/10.1103/PhysRev.38.2265`.

[167] S. R. De Groot, P. Mazur, Non-equilibrium thermodynamics, Dover Publications, New York, 1984.

[168] A. Katchalsky, P. F. Curran, Nonequilibrium thermodynamics in biophysics, Harvard University Press, Cambridge, Massachusetts, 1965. URL: `https://doi.org/10.4159/harvard.9780674494121`.

[169] S. R. Eisenberg, A. J. Grodzinsky, Swelling of articular cartilage and other connective tissues: Electromechanochemical forces, J. Orthop. Res. 3 (1985) 148–159. URL: `https://doi.org/10.1002/jor.1100030204`.

[170] W. Y. Gu, W. M. Lai, V. C. Mow, Hydraulic permeability and electro-kinetic properties of charged-hydrated tissues during permeation, in: Winter Annu. Meet. Am. Soc. Mech. Eng. - Anaheim, CA, USA, 1992, pp. 593–596.

[171] A. J. H. Frijns, J. M. Huyghe, E. F. Kaasschieter, M. W. Wijlaars, Numerical simulation of deformations and electrical potentials in a cartilage substitute,

Biorheology 40 (2003) 123–31. URL: `https://content.iospress.com/articles/biorheology/bir175`.

[172] D. N. Sun, W. Y. Gu, X. E. Guo, W. M. Lai, V. C. Mow, A mixed finite element formulation of triphasic mechano-electrochemical theory for charged, hydrated biological soft tissues, Int. J. Numer. Methods Eng. 45 (1999) 1375–1402. URL: `https://doi.org/10.1002/(SICI)1097-0207(19990810)45:10<1375::AID-NME635>3.0.CO;2-7`.

[173] W. Y. Gu, W. M. Lai, V. C. Mow, Transport of fluid and ions through a porous-permeable charged-hydrated tissue, and streaming potential data on normal bovine articular cartilage, J. Biomech. 26 (1993) 709–723. URL: `https://doi.org/10.1016/0021-9290(93)90034-C`.

[174] W. Y. Gu, W. M. Lai, V. C. Mow, Theoretical basis for measurements of cartilage fixed-charge density using streaming current and electro-osmosis effects, in: Proc. 1993 ASME Winter Annu. Meet. New Orleans, LA, USA, 1993, pp. 55–58.

[175] M. E. Levenston, E. H. Frank, A. J. Grodzinsky, Electrokinetic and poroelastic coupling during finite deformations of charged porous media, J. Appl. Mech. 66 (1999) 323–333. URL: `https://doi.org/10.1115/1.2791052`.

[176] M. Kojic, N. Filipovic, S. Mijailovic, A large strain finite element analysis of cartilage deformation with electrokinetic coupling, Comput. Methods Appl. Mech. Eng. 190 (2001) 2447–2464. URL: `https://doi.org/10.1016/S0045-7825(00)00246-2`.

[177] M. Kojic, N. Filipovic, S. Vulovic, S. Mijailovic, A finite element solution procedure for porous medium with fluid flow and electromechanical coupling, Commun. Numer. Methods Eng. 14 (1998) 381–392. URL: `https://doi.org/10.1002/(SICI)1099-0887(199804)14:4<381::AID-CNM157>3.0.CO;2-1`.

[178] J. R. Sachs, A. J. Grodzinsky, An electromechanically coupled poroelastic medium driven by an applied electric current: Surface detection of bulk material properties, Physicochem. Hydrodyn. 11 (1989) 585–614.

[179] G. A. Ateshian, S. A. Maas, J. A. Weiss, Multiphasic finite element framework for modeling hydrated mixtures with multiple neutral and charged solutes, J. Biomech. Eng. 135 (2013) 1–11. URL: `https://doi.org/10.1115/1.4024823`.

[180] S. A. Maas, B. J. Ellis, G. A. Ateshian, J. A. Weiss, FEBio: Finite Elements for Biomechanics, J. Biomech. Eng. 134 (2012) 1–10. URL: `https://doi.org/10.1115/1.4005694`.

[181] R. C. Lee, E. H. Frank, A. J. Grodzinsky, D. K. Roylance, Oscillatory compressional behavior of articular cartilage and its associated electromechanical properties, J. Biomech. Eng. 103 (1981) 280–292. URL: `https://doi.org/10.1115/1.3138294`.

[182] Y.-J. Kim, L. J. Bonassar, A. J. Grodzinsky, The role of cartilage streaming potential, fluid flow and pressure in the stimulation of chondrocyte biosynthesis during dynamic compression, J. Biomech. 28 (1995) 1055–1066. URL: `https://doi.org/10.1016/0021-9290(94)00159-2`.

[183] A. C. Chen, T. T. Nguyen, R. L. Sah, Streaming potentials during the confined compression creep test of normal and proteoglycan-depleted cartilage, Ann. Biomed. Eng. 25 (1997) 269–277. URL: `https://doi.org/10.1007/BF02648041`.

[184] A. C. Chen, W. C. Bae, R. M. Schinagl, R. L. Sah, Depth- and strain-dependent mechanical and electromechanical properties of full-thickness bovine articular cartilage in confined compression, J. Biomech. 34 (2001) 1–12. URL: `https://doi.org/10.1016/S0021-9290(00)00170-6`.

[185] W. M. Lai, D. D. Sun, G. A. Ateshian, X. E. Guo, V. C. Mow, Electrical signals for chondrocytes in cartilage, Biorheology 39 (2002) 39–45.

[186] A. J. H. Frijns, J. M. Huyghe, M. W. Wijlaars, Deformations and electrical potentials in a charged porous medium, Technical Report, Technische Universiteit Eindhoven, Eindhoven, 2001.

[187] V. C. Mow, D. D. Sun, X. E. Guo, M. Likhitpanichkul, W. M. Lai, Fixed Negative charges modulate mechanical behaviours and electrical signals in articular cartilage under unconfined compression - a triphasic paradigm, in: Wolfgang Ehlers (Ed.), Porous Media Theroy, Exp. Numer. Appl., 2002, pp. 227–247. URL: `https://doi.org/10.1007/978-3-662-04999-0_7`.

[188] D. D. Sun, X. E. Guo, M. Likhitpanichkul, W. M. Lai, V. C. Mow, The influence of the fixed negative charges on mechanical and electrical behaviors of articular cartilage under unconfined compression, J. Biomech. Eng. 126 (2004) 6. URL: `https://doi.org/10.1115/1.1644562`.

[189] L. P. Li, W. Herzog, Electromechanical response of articular cartilage in indentation - considerations on the determination of cartilage properties during arthroscopy, Comput. Methods Biomech. Biomed. Engin. 8 (2005) 83–91. URL: `https://doi.org/10.1080/10255840500167895`.

[190] L. Q. Wan, C. Miller, X. E. Guo, V. C. Mow, Fixed electrical charges and mobile ions affect the measurable mechano-electrochemical properties of charged-hydrated biological tissues: The articular cartilage paradigm, Mech Chem Biosyst. 1 (2004) 81–99. URL: `https://doi.org/10.1038/jid.2014.371`.

[191] J. R. Sachs, A. J. Grodzinsky, Electromechanical spectroscopy of cartilage using a surface probe with applied mechanical displacement, J. Biomech. 28 (1995) 963–976. URL: `10.1016/0021-9290(94)00108-G`.

[192] W. Y. Gu, W. M. Lai, V. C. Mow, A triphasic analysis of negative osmotic flows through charged hydrated soft tissues, J. Biomech. 30 (1997) 71–78. URL: `https://doi.org/10.1016/S0021-9290(96)00099-1`.

[193] W. Y. Gu, D. N. Sun, W. M. Lai, V. C. Mow, Analysis of the dynamic permeation experiment with implication to cartilaginous tissue engineering, J. Biomech. Eng. 126 (2004) 485–491. URL: `https://doi.org/10.1115/1.1785806`.

[194] É. Quenneville, M. D. Buschmann, A transport model of electrolyte convection through a charged membrane predicts generation of net charge at membrane/electrolyte interfaces, J. Memb. Sci. 265 (2005) 60–73. URL: `https://doi.org/10.1016/j.memsci.2005.04.032`.

[195] Ankit Rohatgi, WebPlotDigitizer, 2020. URL: `https://automeris.io/WebPlotDigitizer`.

[196] C. G. Armstrong, W. M. Lai, V. C. Mow, An analysis of the unconfined compression of articular cartilage., J. Biomech. Eng. 106 (1984) 165–173. URL: `https://doi.org/10.1115/1.3138475`.

[197] V. C. Mow, M. H. Holmes, W. M. Lai, Fluid transport and mechanical properties of articular cartilage: A review, J. Biomech. 17 (1984) 377–394. URL: `https://doi.org/10.1016/0021-9290(84)90031-9`.

[198] M. S. Gockenbach, Understanding and lmplementing the Finite Element Method, Society for Industrial and Applied Mathematics, Philadelphia, PA, USA, 2006. URL: `https://doi.org/10.1137/1.9780898717846`.

[199] A. H. Doulabi, K. Mequanint, H. Mohammadi, Blends and nanocomposite biomaterials for articular cartilage tissue engineering, Materials (Basel). 7 (2014) 5327–5355. URL: `https://doi.org/10.3390/ma7075327`.

[200] S. Ansari, S. Khorshidi, A. Karkhaneh, Engineering of gradient osteochondral tissue: From nature to lab, Acta Biomater. 87 (2019) 41–54. URL: `https://doi.org/10.1016/j.actbio.2019.01.071`.

[201] J. Jacob, N. More, K. Kalia, G. Kapusetti, Piezoelectric smart biomaterials for bone and cartilage tissue engineering, Inflamm. Regen. 38 (2018) 2. URL: `https://doi.org/10.1186/s41232-018-0059-8`.

[202] P. J. Flory, Principles of Polymer Chemistry, Cornell University Press, Ithaca, New York, NY, USA, 1953.

[203] F. G. Donnan, The theory of membrane equilibria, Chem. Rev. 1 (1924) 73–90. URL: `https://doi.org/10.1021/cr60001a003`.

[204] T. Shiga, T. Kurauchi, Deformation of polyelectrolyte gels under the influence of electric field, J. Appl. Polym. Sci. 39 (1990) 2305–2320. URL: `https://doi.org/10.1002/app.1990.070391110`.

[205] M. Doi, M. Matsumoto, Y. Hirose, Deformation of Ionic Polymer Gels by Electric Fields, Macromolecules 25 (1992) 5504–5511. URL: `https://doi.org/10.1021/ma00046a058`.

[206] P. E. Grimshaw, J. H. Nussbaum, A. J. Grodzinsky, M. L. Yarmush, Kinetics of electrically and chemically induced swelling in polyelectrolyte gels, J. Chem. Phys. 93 (1990) 4462–4472. URL: `https://doi.org/10.1063/1.458729`.

[207] X. Zhou, Y. C. Hon, S. Sun, A. F. T. Mak, Numerical simulation of the steady-state deformation of a smart hydrogel under an external electric field, Smart Mater. Struct. 11 (2002) 459–467. URL: `https://doi.org/10.1088/0964-1726/11/3/316`.

[208] H. Li, Z. Yuan, K. Y. Lam, H. P. Lee, J. Chen, J. Hanes, J. Fu, Model development and numerical simulation of electric-stimulus-responsive hydrogels subject to an externally applied electric field, Biosens. Bioelectron. 19 (2004) 1097–1107. URL: `https://doi.org/10.1016/j.bios.2003.10.004`.

[209] T. Wallmersperger, B. Kröplin, R. W. Gülch, Coupled chemo-electro-mechanical formulation for ionic polymer gels - Numerical and experimental investigations, Mech. Mater. 36 (2004) 411–420. URL: `https://doi.org/10.1016/S0167-6636(03)00068-1`.

[210] M. K. Ghantasala, K. J. Suthar, D. C. Mancini, Steady-state simulation of the chemo-electro-mechanical behaviour of hydrogels, Int. J. Model. Simul. 30 (2010) 396–404. URL: `https://doi.org/10.1080/02286203.2010.11442596`.

[211] U. Ayachit, The paraView guide: A parallel visualization application, Kitware, Inc., Clifton Park, NY, USA, 2015. URL: `https://doi.org/10.5555/2789330`.

[212] C. Geuzaine, J.-F. Remacle, Gmsh: A 3-D finite element mesh generator with built-in pre- and post-processing facilities, Int. J. Numer. Methods Eng. 79 (2009) 1309–1331. URL: `https://doi.org/10.1002/nme.2579`.

[213] F. Helfferich, Ion exchange, McGraw-Hill Book Company, Inc., New York, NY, USA, 1962.

[214] W. Nernst, Zur Kinetik der in Lösung befindlichen Körper, Zeitschrift für Phys. Chemie 2U (1888) 613–637. URL: `https://doi.org/10.1515/zpch-1888-0274`.

[215] W. Nernst, Die elektromotorische Wirksamkeit der Jonen, Zeitschrift für Phys. Chemie 4U (1889) 129–181. URL: `https://doi.org/10.1515/zpch-1889-0412`.

[216] M. Planck, Ueber die Erregung von Electricität und Wärme in Electrolyten, Ann. Phys. 275 (1890) 161–186. URL: `https://doi.org/10.1002/andp.18902750202`.

[217] P. G. Bruce (Ed.), Solid State Electrochemistry, Cambridge University Press, Cambridge, UK, 1995. URL: `https://doi.org/10.1017/CBO9780511524790`.

[218] B. E. Abali, Computational reality_Solving nonlinear and coupled problems in continuum mechanics, Springer, Singapore, 2017. URL: `https://doi.org/10.1007/978-981-10-2444-3`.

[219] F. Brezzi, M. Fortin, Mixed and Hybrid Finite Element Methods, volume 15 of *Springer Series in Computational Mathematics*, Springer-Verlag, 1991. URL: `https://doi.org/10.1007/978-1-4612-3172-1`.

[220] P. Amestoy, I. S. Duff, J.-Y. L'Excellent, J. Koster, A fully asynchronous multifunctional solver using distributed dynamic scheduling, SIAM J. Matrix Anal. Appl. 23 (2001) 15–41. URL: `https://doi.org/10.1137/S0895479899358194`.

[221] C. Yu, K. Malakpoor, J. M. Huyghe, A three-dimensional transient mixed hybrid finite element model for superabsorbent polymers with strain-dependent permeability, Soft Matter 14 (2018) 3834–3848. URL: `https://doi.org/10.1039/c7sm01587a`.

[222] P. J. Basser, A. J. Grodzinsky, The Donnan model derived from microstructure, Biophys. Chem. 46 (1993) 57–68. URL: `https://doi.org/10.1016/0301-4622(93)87007-J`.

[223] M. D. Buschmann, A. J. Grodzinsky, A molecular model of proteoglycan-associated electrostatic forces in cartilage mechanics, J. Biomech. Eng. 117 (1995) 179–192. URL: `https://doi.org/10.1115/1.2796000`.

[224] J. T. G. Overbeek, The Donnan equilibrium, Prog. Biophys. Biophys. Chem. 6 (1956) 57–84. URL: `https://doi.org/10.1016/S0096-4174(18)30104-5`.

[225] R. W. Gülch, J. Holdenried, A. Weible, T. Wallmersperger, B. Kröplin, Polyelectrolyte gels in electric fields: a theoretical and experimental approach, in: Proc. SPIE 3987, Smart Struct. Mater. 2000 Electroact. Polym. Actuators Devices, volume 3987, 2000, pp. 193–202. URL: `https://doi.org/10.1117/12.387778`.

[226] J. M. Patel, K. S. Saleh, J. A. Burdick, R. L. Mauck, Bioactive factors for cartilage repair and regeneration: Improving delivery, retention, and activity, Acta Biomater. 93 (2019) 222–238. URL: `https://doi.org/10.1016/j.actbio.2019.01.061`.

[227] Z. Ji, K. Yan, W. Li, H. Hu, X. Zhu, Mathematical and computational modeling in complex biological systems, Biomed Res. Int. 2017 (2017) 5958321. URL: `https://doi.org/10.1155/2017/5958321`.

[228] S. L. Peck, Simulation as experiment: A philosophical reassessment for biological modeling, Trends Ecol. Evol. 19 (2004) 530–534. URL: `https://doi.org/10.1016/j.tree.2004.07.019`.

[229] L. Geris, et al., Computational modeling in tissue engineering, Springer, Berlin, Heidelberg, 2013. URL: `https://doi.org/10.1007/978-3-642-32563-2`.

[230] E. G. Baylon, M. E. Levenston, Osmotic swelling responses are conserved across cartilaginous tissues with varied sulfated-glycosaminoglycan contents, J. Orthop. Res. 38 (2020) 785–792. URL: `https://doi.org/10.1002/jor.24521`.

[231] M. Lv, Y. Zhou, X. Chen, L. Han, L. Wang, X. L. Lu, Calcium signaling of in situ chondrocytes in articular cartilage under compressive loading: Roles of calcium sources and cell membrane ion channels, J. Orthop. Res. 36 (2018) 730–738. URL: `https://doi.org/10.1002/jor.23768`.

[232] Y. Zhou, M. A. David, X. Chen, L. Q. Wan, R. L. Duncan, L. Wang, X. L. Lu, Effects of Osmolarity on the spontaneous calcium signaling of in situ juvenile and adult articular chondrocytes, Ann. Biomed. Eng. 44 (2016) 1138–1147. URL: `https://doi.org/10.1007/s10439-015-1406-4`.

[233] A. Mobasheri, C. Matta, I. Uzielienè, E. Budd, P. Martín-Vasallo, E. Bernotiene, The chondrocyte channelome: A narrative review, Jt. Bone Spine 86 (2019) 29–35. URL: `https://doi.org/10.1016/j.jbspin.2018.01.012`.

[234] T. Shiga, Deformation and viscoelastic behavior of polymer gels in electric fields, in: Neutron Spin Echo Spectroscopy Viscoelasticity Rheology, volume 134 of *Advances in Polymer Science*, Springer, Berlin, Heidelberg, 1997, pp. 131–163. URL: `https://doi.org/10.1007/3-540-68449-2_2`.

[235] P. J. Flory, J. Rehner, Statistical mechanics of cross-linked polymer networks I. Rubberlike Elasticity, J. Chem. Phys. 11 (1943) 512–520. URL: `https://doi.org/10.1063/1.1723792`.

[236] P. J. Flory, J. Rehner, Statistical mechanics of cross-linked polymer networks II. Swelling, J. Chem. Phys. 11 (1943) 521–526. URL: `https://doi.org/10.1063/1.1723792`.

[237] P. E. Grimshaw, A. J. Grodzinsky, M. L. Yarmush, D. M. Yarmush, Dynamic membranes for protein transport: chemical and electrical control, Chem. Eng.

Sci. 44 (1989) 827–840. URL: `https://doi.org/10.1016/0009-2509(89)85256-X`.

[238] Y. C. Hon, M. W. Lu, A. F. T. Mak, X. Zhou, Mechano-electrochemical response analysis of a hydrogel strip under electric field, in: Adv. Comput. Eng. Sci., Tch Science Press, 2000, pp. 1681–1686. URL: `http://hdl.handle.net/10397/73198`.

[239] H. Li, J. Chen, K. Y. Lam, Multiphysical Modeling and Meshless Simulation of Electric-Sensitive Hydrogels, J. Polym. Sci. Part B Polym. Phys. 42 (2004) 1514–1531. URL: `https://doi.org/10.1002/polb.20025`.

[240] D. S. Chandrasekharaiah, L. Debnath, Continuum Mechanics, Academic Press, San Diego, 1994. URL: `https://doi.org/10.1016/C2009-0-21209-8`.

[241] T. Tanaka, L. O. Hocker, G. B. Benedek, Spectrum of light scattered from a viscoelastic gel, J. Chem. Phys. 59 (1973) 5151–5159. URL: `https://doi.org/10.1063/1.1680734`.

[242] F. Horkay, I. Tasaki, P. J. Basser, Osmotic swelling of polyacrylate hydrogels in physiological salt solutions, Biomacromolecules 1 (2000) 84–90. URL: `https://doi.org/10.1021/bm9905031`.

[243] M. A. Biot, Theory of deformation of a porous viscoelastic anisotropic solid, J. Appl. Phys. 27 (1956) 459–467. URL: `https://doi.org/10.1063/1.1722402`.

[244] H. Li, J. Chen, K. Y. Lam, Transient simulation of kinetics of electric-sensitive hydrogels, Biosens. Bioelectron. 22 (2007) 1633–1641. URL: `https://doi.org/10.1016/j.bios.2006.07.016`.

[245] T. Wallmersperger, D. Ballhause, Coupled chemo-electro-mechanical finite element simulation of hydrogels: II. Electrical stimulation, Smart Mater. Struct. 17 (2008) 1–10. URL: `https://doi.org/10.1088/0964-1726/17/4/045012`.

[246] T. Ning, J. Guo, K. Zhang, K. Li, J. Zhang, Z. Yang, Z. Ge, Nanosecond pulsed electric fields enhanced chondrogenic potential of mesenchymal stem cells via JNK/CREB-STAT3 signaling pathway, Stem Cell Res. Ther. 10 (2019) 45. URL: `https://doi.org/10.1186/s13287-019-1133-0`.

[247] J. J. Vaca-González, S. Clara-Trujillo, M. Guillot-Ferriols, J. Ródenas-Rochina, M. J. Sanchis, J. L. G. Ribelles, D. A. Garzón-Alvarado, G. G. Ferrer, Effect of electrical stimulation on chondrogenic differentiation of mesenchymal stem cells cultured in hyaluronic acid – Gelatin injectable hydrogels, Bioelectrochemistry 134 (2020) 107536. URL: `https://doi.org/10.1016/j.bioelechem.2020.107536`.

[248] M. Ganser, F. E. Hildebrand, M. Kamlah, R. M. McMeeking, A finite strain electro-chemo-mechanical theory for ion transport with application to binary solid electrolytes, J. Mech. Phys. Solids 125 (2019) 681–713. URL: `https://doi.org/10.1016/j.jmps.2019.01.004`.

[249] G. Pattappa, J. Zellner, B. Johnstone, D. Docheva, P. Angele, Cells under pressure - the relationship between hydrostatic pressure and mesenchymal stem cell chondrogenesis, Eur. Cells Mater. 37 (2019) 360–381. URL: `https://doi.org/10.22203/eCM.v037a22`.

[250] H. L. Lim, J. C. Chuang, T. Tran, A. Aung, G. Arya, S. Varghese, Dynamic electromechanical hydrogel matrices for stem cell culture, Adv. Funct. Mater. 21 (2011) 55–63. URL: `https://doi.org/10.1002/adfm.201001519`.

[251] P. W. Hsieh, S. Y. Yang, A new stabilized linear finite element method for solving reaction-convection-diffusion equations, Comput. Methods Appl. Mech. Eng. 307 (2016) 362–382. URL: `https://doi.org/10.1016/j.cma.2016.04.024`.

[252] D. Pearce, S. Fischer, F. Huda, A. Vahdati, Applications of computer modeling and simulation in cartilage tissue engineering, Tissue Eng. Regen. Med. 17 (2019) 1–13. URL: `https://doi.org/10.1007/s13770-019-00216-9`.

[253] S. Krüeger, S. Achilles, J. Zimmermann, T. Tischer, R. Bader, A. Jonitz-Heincke, Re-differentiation capacity of human chondrocytes in vitro following electrical stimulation with capacitively coupled fields, J. Clin. Med. 8 (2019) 1771. URL: `https://doi.org/10.3390/jcm8111771`.

[254] L. H. Olesen, M. Z. Bazant, H. Bruus, Strongly nonlinear dynamics of electrolytes in large ac voltages, Phys. Rev. E - Stat. Nonlinear, Soft Matter Phys. 82 (2010) 1–29. URL: `https://doi.org/10.1103/PhysRevE.82.011501`.

[255] A. Golovnev, S. Trimper, Analytical solution of the PNP equations at AC applied voltage, Phys. Lett. A 376 (2012) 1391–1395. URL: `https://doi.org/10.1016/j.physleta.2012.03.014`.

[256] T. Distler, F. Ruther, A. R. Boccaccini, R. Detsch, Development of 3D biofabricated cell laden hydrogel vessels and a low-cost desktop printed perfusion chamber for in vitro vessel maturation, Macromol. Biosci. 19 (2019) 1900245. URL: `https://doi.org/10.1002/mabi.201900245`.

[257] T. Distler, A. R. Boccaccini, 3D printing of electrically conductive hydrogels for tissue engineering and biosensors - A review, Acta Biomater. 101 (2020) 1–13. URL: `https://doi.org/10.1016/j.actbio.2019.08.044`.

[258] K. B. Goh, H. Li, K. Y. Lam, Modeling the impact of pH- and oxygen-coupled stimuli on osmotic pressure and electrical potential responses of hemoglobin-loaded polyampholyte hydrogel, ACS Appl. Bio Mater. 1 (2018) 318–327. URL: `https://doi.org/10.1021/acsabm.8b00074`.

[259] H. Ye, Y. Liu, L. Gao, T. Du, Y. Jia, Effects of solution pH on ion distribution and drug release behaviors of a weak polyelectrolyte hydrogel, Polym. Int. 66 (2017) 1662–1668. URL: `https://doi.org/10.1002/pi.5429`.

[260] M. J. Bassetti, A. N. Chatterjee, N. R. Aluru, D. J. Beebe, Development and Modeling of Electrically Triggered Hydrogels for Microfluidic Applications, J. Microelectromechanical Syst. 14 (2005) 1198–1207. URL: `https://doi.org/10.1109/JMEMS.2005.845407`.

Curriculum vitae

PERSONAL INFORMATION

Abdul Razzaq Farooqi

📍 Institute of General Electrical Engineering (IEF), Albert Einstein Str. 2, 18059 Rostock (Germany)
✉ abdul.farooqi@uni-rostock.de

Date of birth 02/04/1988 | Nationality Pakistani

EDUCATION AND TRAINING

10/2016–Present

PhD (Electrical Engineering)

Universität Rostock
Albert Einstein Str. 2, 18059 Rostock (Germany)
www.uni-rostock.de

Thesis title:

Computational Modeling of Electroactive Hydrogels for Cartilage–Tissue Repair Using Electrical Stimulation

01/2010–01/2012

MS (Electronic Engineering)

GIK Institute of Engineering Sciences & Technology
23640 Topi (Pakistan)
www.giki.edu.pk

Cumulative GPA: 3.38/4.0

Thesis Title:

Electromagnetic Field Focusing Applications of Chiro Cylindrical Reflectors

09/2005–10/2009

BS (Electronic Engineering)

The Islamia University of Bahawalpur
63100 Bahawalpur (Pakistan)
www.iub.edu.pk

Aggregate: 75.08%

WORK EXPERIENCE

02/2013–09/2016

Lecturer

Department of Electronic Engineering, The Islamia University of Bahawalpur
63100 Bahawalpur (Pakistan)
www.iub.edu.pk

01/2012–02/2013

Research Associate

Faculty of Electronic Engineering, GIK Institute of Engineering Sciences & Technology
23460 Topi (Pakistan)
www.giki.edu.pk

ADDITIONAL INFORMATION

Memberships

Institute of Electrical & Electronics Engineers (IEEE).
Pakistan Engineering Council (PEC).

Declaration of Authorship

I, Abdul Razzaq Farooqi hereby declare that the thesis titled “Computational Modeling of Electroactive Hydrogels for Cartilage–Tissue Repair Using Electrical Stimulation” has been written by me under the guidance of my supervisors. All the sources of information and aid have been acknowledged to the best of my knowledge. This thesis has not been submitted previously for any other qualification at any other universities or institutions.

Rostock, 17.06.2020

Abdul Razzaq Farooqi